STUDIA UNIVERSITATIS
BABEŞ-BOLYAI

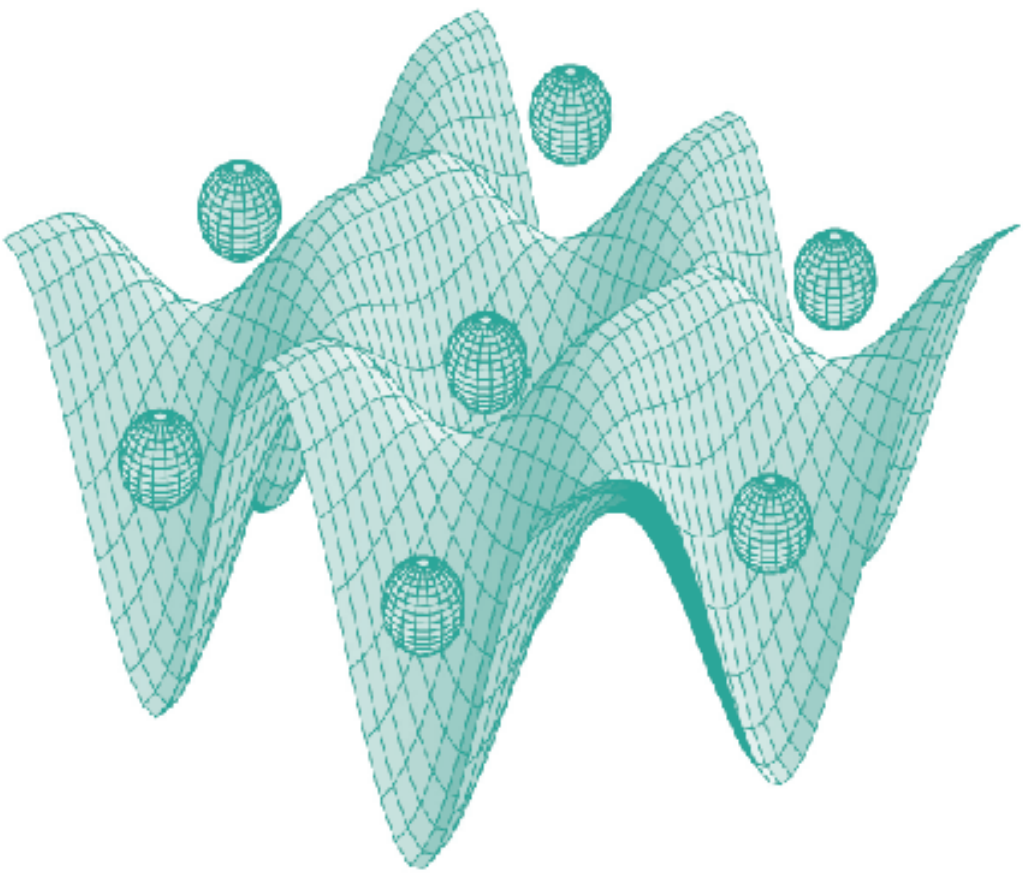

PHYSICA

1-2/2022

STUDIA
UNIVERSITATIS BABEŞ-BOLYAI
PHYSICA

1-2/2022

ISSN (print): 0258-8730;
ISSN (online): 2065-9415; ISSN-L: 0258-8730;

Published by Babeş-Bolyai University

EDITORIAL OFFICE OF STUDIA UBB PYSICA:
1, M. Kogălniceanu St., Cluj-Napoca, ROMANIA, Phone: +40 264 405300
http://www.studia.ubbcluj.ro/serii/physica/index_en.html

YEAR **Volume 67 (LXVII) 2022**
MONTH **DECEMBER**
ISSUE **1-2**

PUBLISHED ONLINE: 2022-12-30
PUBLISHED PRINT: 2022-12-30
ISSUE DOI:10.24193/subbphys.2022

S T U D I A
UNIVERSITATIS BABEȘ–BOLYAI
PHYSICA

1-2

DEDICATED TO PROFESSOR ROMULUS TETEAN ON HIS 65 ANNIVERSARY

CUPRINS – CONTENT – SOMMAIRE – INHALT

V. POP, *Foreword: Anniversary of Professor Romulus Tetean Vinteler* 5

R. DUDRIC, G. SOUCA, F. GOGA, *Magnetocaloric effect in $La_{1.2}R_{0.2}Ca_{1.6}Mn_2O_7$ (R=Tb, Dy, Ho, Er) perovskites synthesized by sol-gel method* 9

R. HIRIAN, A. MERCEA, V. POP, *Investigation of the physical properties of $MnNi_{(1-X)}M_X$ alloys where M=Ti, Al* 17

R. HIRIAN, V. POP, O. ISNARD, D. BENEA, *Magnetic properties of $(Fe,Co)_5SiB_2$ alloys by W doping* 25

I. GROSU, *Conductance of an one and double-level Quantum dot* 35

M. TOMA, D. MARCONI, C. LUNG, M. POP, A. POP, *Structure and morphology of ZnO films co-doped with Al and rare earth deposited by spray coating technique* 43

L.C. COTET, C. SALAGEAN, A. MIHIS, I. SZÉKELY, Zs. TOTH, L. BAIA, M. BAIA, G. OLTEANU, I. OLTEANU, V. DANCIU, *Suspension based on a mixture of titania-silica-functionalized graphene oxide for surface consolidation of historical andesite stone and mortar* 55

I. PETROVAI, O. TODOR-BOER, L. DAVID, I. BOTIZ, *Enhancing the photo-luminescence of polyfluorene-based thin films via illumination* 79

R.-A. ONE, C. V. TIUSAN, *Rashba Field Contribution and Electric Field Control of the Magnetic Anisotropy* 91

R. LUCHIAN, Z. BORSAY, D. MANIU, N. LEOPOLD, V. CHIȘ, Vibrational Features of Diphenylhydantoin 107

STUDIA UBB PHYSICA, Vol. 67 (LXVII), 1-2, 2022, pp. 5-8
(RECOMMENDED CITATION)

FOREWORD:

ANNIVERSARY OF PROFESSOR ROMULUS TETEAN VINTELER

I appreciate the opportunity offered by this anniversary issue of the scientific journal *Studia Physica* to note some important aspects related to the didactic and research activity of professor doctor Romulus Tetean.

Profesor Romulus Tetean was born in Sântejude, Cluj County, Romania, on November 11, 1957. He graduated Faculty of Physics at the Babeș-Bolyai University in 1981. Thanks to the exceptional results obtained during his undergraduate studies, Romulus Tetean was among the most meritorious students who followed the Solid State Physics master's degree, graduating in 1982 at Babeș-Bolyai University. He performed his PhD studies between 1993 and 1997 at Babeș-Bolyai University under the supervision of professor Emil Burzo. This period allowed him to advance his scientific competences in the field of materials science, more precisely in that of the magnetism of intermetallic compounds of 3d transition metals with rare earths.

The scientific research of prof. Tetean were mainly directed in the study of the structural, electronic, magnetic and transport properties of different classes of materials, such as rare earth - 3*d* transition metal intermetallic compounds, permanent magnets, nanostructured materials, perovskites and superconducting materials with possible technical applications such as permanent magnets, sensors, biomedicine and magnetic refrigeration. He was involved in preparation of new classes of materials and characterization by X-ray diffraction, X-ray photoelectron spectroscopy (XPS), magnetic susceptibility, magnetization, specific heat, electronic properties, Mossbauer effect, and muon spin rotation and relaxation (μSR).

The firs job of professor Tetean was as middle school and high school teacher at Deusu school and later at Baciu school and Natural Science High School Cluj-Napoca, his teaching activity being appreciated by his students and colleagues.

In 1991, he achieved, by competition, the position of assistant at Faculty of Physics at the Babeș-Bolyai University. As a result of the exceptional didactic and scientific activity, professor Romulus Tetean evolved in his career to the positions of lecturer (1997-2001), assistant professor (2001-2008) and full professor at Babeș-Bolyai University from 2008 to present. In this period, he was teaching different courses, seminars and laboratory classes, for doctoral school, graduated and undergraduate students, like: Advanced methods in condensed matter physics – Doctoral school, Nanostructured materials, Magnetic and Superconducting Materials – for master students in Solid State Physics, Superconducting materials and applications, Semiconductors physics, Thermoelectric phenomena, Electricity and magnetism, Electrotechnic etc, for undergraduate students in technological physics, in physics and mathematics physics.

His organizational skills were brought to fruition as Head of Condensed Matter Physics and Advanced Technologies Department, Faculty of Physics, Babeș-Bolyai University and Head of Condensed Matter Physics and Advanced Technologies Research Center, Ioan Ursu Institute, Babeș-Bolyai University.

The research activity of professor Tetean was focused in the synthesis and study of the structural, electric and magnetic properties of materials like rare earths-3d transition metals intermetallic compounds, superconducting oxides, materials for magnetic hyperthermia, from both, fundamental researches and applications. Recent research activity was focuses on:

- Synthesis and characterization of new 3d transition metals - rare earths intermetallic compounds with applications in magnetocaloric refrigeration. In addition to the fundamental physics characteristics involved in the study of these systems, the aspects related to the stability of the phases, the efficiency of the magnetocaloric effect and the obtaining of predefined working temperatures were mainly followed.
- A very actual research activity is dedicated in preparation and characterization of magnetic materials for biomedicine. The aspects concerning magnetic hyperthermia followed different problems linked to the Specific Absorption Rate dependence on the external alternating magnetic field amplitude, toxicity, biodegradation etc.

The research results were expressed in more than 140 papers with 104 papers published in high impact ISI journals like journal of Journal of Molecular Structure, Nanoscale research letters, Nanomaterials, Molecules, Journal of Physics: Condensed Matter, Pharmaceutics, Chemical Engineering Journal, Magnetochemistry, Applied Surface Science, Molecular Crystals and Liquid Crystals, Journal of Alloys and

Compounds, Journal of Magnetism and Magnetic Materials, Journal of Materials Science, Solid State Communications, Journal of Applied Physics, Physica Status Solidi etc. He also has published 8 books. The high scientific and impact on the scientific community of his publications is confirmed by the large number of citations (more than 1040). For his scientific performance he was honored with Stefan Procopiu Romanian Academy prize 2019 and Babeș-Bolyai University award for excellence in research activity (2008 and 2011).

Besides the rigorous scientific activity carried out at the Faculty of Physics, Babeș-Bolyai University, Professor Romulus Tetean was involved in the academic development at local and national levels. He was invited in prestigious institutions for research stages at Univ. Joseph Fourier, Grenoble, Franta, Univ. Louis Pasteur, Strasbourg, Franta, Technical University of Chemnitz, Germania, University of Osnabrueck, Germania, Paul Scherrer Institute, Vilingen, Elvetia. These collaborations led to the development and valorization of scientific research, as well as to the improvement or management of new international collaboration programs, among which should be noted the perennial collaboration, both for scientific research and for didactic activity, with the University of Chemnitz. Professor Romulus Tetean was local coordinator for Tempus/Erasmus program and European Scheme for Physics Student Mobility.

Professor Tetean was involved in the organization or led the organizing committees of various conferences or summer schools, such as: Magnetic Materials and Superconductors Conference, Cluj-Napoca, 3rd General Conference of the Balkan Physical Union, Cluj-Napoca, German-Romanian summer schools, ICPAM 11, ICPAM 12, ICPAM 13, ICPAM 14, member in the organizing committee of two European Schools on Magnetism and many international conferences.

As consequence of his scientific results in research activity, professor Tetean has 12 invited lectures and 33 oral presentations at international conferences. Professor Tetean won by competition 6 national research grants as project coordinator and he lead 3 international grants.

Professor Romulus Tetean is member of the following national or international scientific societies: European Physical Society, Romanian Physical Society, Balkan Physical Society, Romanian Materials Society, Rare earths Society, μSR Society.

Under his supervision, many students have obtained their B.Sc. and M.Sc. Diploma or obtained PhD in physics. Some of his coworkers have pursued a successful research or academic career.

On behalf of all those who have benefited from the scientific achievements of Professor Romulus Tetean, as well as from his fruitful discussions and advices, we wish to express our sincere appreciation and best wishes for the future.

Viorel POP

Professor, Babeș-Bolyai University, Cluj-Napoca, Romania

STUDIA UBB PHYSICA, Vol. 67 (LXVII), 1-2, 2022, pp. 9-16
(RECOMMENDED CITATION)
doi:10.24193/subbphys.2022.01

MAGNETOCALORIC EFFECT IN $La_{1.2}R_{0.2}Ca_{1.6}Mn_2O_7$ (R=Tb, Dy, Ho, Er) PEROVSKITES SYNTHESIZED BY SOL-GEL METHOD

R. DUDRIC[1*], G. SOUCA[1], F. GOGA[2]

ABSTRACT. Nanocrystalline double layered $La_{1.2}R_{0.2}Ca_{1.6}Mn_2O_7$ manganites with R = Tb, Dy, Ho, and Er were synthesized by sol-gel method. The XRD measurements indicate that all samples are single phase with a $Sr_3Ti_2O_7$-type tetragonal (I4*/mmm*) structure and mean crystallite sizes between 22 nm and 27 nm. The magnetic measurements evidence a spin-glass like behavior at low temperatures for all samples, which may be due to frustration of random competing ferromagnetic and antiferromagnetic interactions together with the anisotropy originating from the layered structure. A moderate magnetocaloric effect was found for all samples, with the maximum entropy change located at temperatures near the magnetic transition ones, but high *RCP*(*S*) values were obtained due to the broadened magnetic entropy curves.

Keywords: *nanoparticles, double layered perovskite, magnetocaloric effect.*

INTRODUCTION

The double-layered manganites show many intriguing properties such as colossal magnetoresistance, charge ordering, anisotropic transport in charge carriers, and the possibility of a short-range magnetic ordering above the 3D ferromagnetic transition temperature [1-7]. The doped $R_{2-2x}A_{1+2x}Mn_2O_7$ perovskites (R is a trivalent rare earth ion and A is a divalent alkaline earth cation) consist of MnO_2 bilayers separated by insulating $(R,A)_2O_2$ rock-salt layers, stacked along the *c*-axis, leading to a quasi-two-dimensional structure. The inherent anisotropy

[1] *Faculty of Physics, Babes-Bolyai University, Kogalniceanu 1, 400084 Cluj-Napoca, Romania*
[2] *Faculty of Chemistry and Chemical Engineering, Babes-Bolyai University, Arany Janos 11, 400028 Cluj-Napoca, Romania*
** Corresponding author: roxana.dudric@ubbcluj.ro*

resulted from their layered structure and its consequences for studying low-dimensional physics, as well as the remarkable range of physical properties have generated much interest. Two anisotropic exchange interactions are expected in these manganites, namely: an intralayer exchange interaction within the MnO_2 bilayers and an interlayer exchange interaction acting between the perovskite MnO_2 bilayers, which could be the reason for the two transition temperatures for magnetic ordering [2,8,9]. Among other intriguing properties, $La_{2-2x}Ca_{1+2x}Mn_2O_7$ perovskites exhibit colossal magnetoresistance (CMR) effect at low temperatures [1,3,10] and large magnetic entropy change under a moderate magnetic field [11-13].

The physical properties of double-layered manganites are sensitive to small changes in composition and structure [4]. In particular, the magnetic transition Curie temperature and the magnetic entropy change are influenced by the preparation conditions of these materials. The substitution of La with other rare earth atoms may induce lattice effects and/or change the magnetic interactions.

In this work we present the magnetic properties and magnetocaloric effect of $La_{1.2}R_{0.2}Ca_{1.6}Mn_2O_7$ with R = Tb, Dy, Ho, and Er manganites.

EXPERIMENTAL

Polycrystalline powders of $La_{1.2}R_{0.2}Ca_{1.6}Mn_2O_7$ with R = Tb, Dy, Ho, and Er perovskites were synthesized by sol-gel method, as previously described [14].

The crystal structure of the samples was analyzed at room temperature by using a Bruker D8 Advance AXS X-ray diffractometer with Cu *Kα* radiation in the 2θ region 20°-90°. The crystallite-sizes of the powders were estimated according to the Debye-Scherrer equation:

$$D = \frac{k\lambda}{\beta \cos\theta} \tag{1}$$

where *β* is the peak full width at half maximum (in radians) at the observed peak angle *ϑ*, k is the crystallite shape factor (was considered 0.94) and λ is the X-ray wavelength (0.154 nm).

Magnetic measurements were carried out on pellets, obtained from pressing the powders, using a 12 T VSM from Cryogenics in the temperature range 4.2 – 300 K. The magnetic entropy changes were determined from magnetization isotherms, between zero field and a maximum field (H_0) using the thermodynamic relation:

$$\Delta S_m(T, H_0) = S_m(T, H_0) - S_m(T, 0) = \frac{1}{\Delta T}\int_0^H [M(T + \Delta T, H) - M(T, H)]dT \tag{2}$$

where ΔT = 5 K is the temperature increment between measured magnetization isotherms. The magnetic cooling efficiency was evaluated by calculating the relative cooling power (RCP) based on the magnetic entropy change:

$$RCP(S) = -\Delta S_m(T, H_0) \times \delta T_{FWHM} \quad (3)$$

ΔS_m represents the maximum magnetic entropy change and δT_{FWHM} its full-width at half-maximum.

RESULTS AND DISCUSSION

The crystal structure and crystallite sizes of the polycrystalline powders obtained by sol-gel method were determined by Rietveld refinement of XRD patterns using FullProf Suite Software [15]. The X-ray diffraction analysis (Fig. 1) shows that all $La_{1.2}R_{0.2}Ca_{1.6}Mn_2O_7$ are single phase with a $Sr_3Ti_2O_7$-type tetragonal (I4/*mmm*) structure.

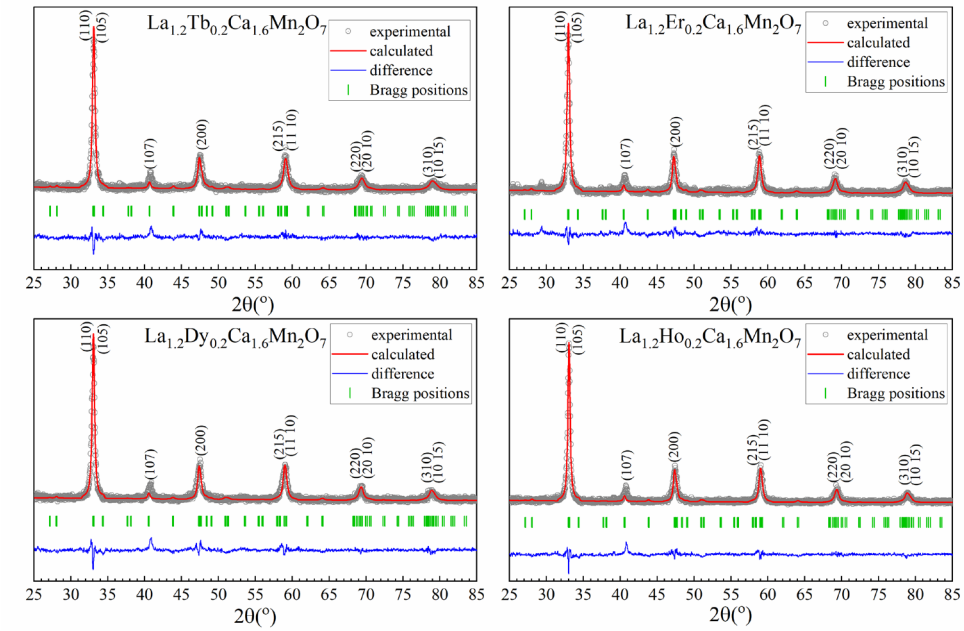

Fig. 1. Rietveld refinement results for the XRD patterns of $La_{1.2}R_{0.2}Ca_{1.6}Mn_2O_7$ manganites recorded at room temperature.

The lattice parameters calculated using the Rietveld method, *c/a* ratios and crystallite-sizes obtained using the Debye-Scherrer equation are collected in Table 1. The lattice parameters determined for $La_{1.2}R_{0.2}Ca_{1.6}Mn_2O_7$ are smaller than for $La_{1.4}Ca_{1.6}Mn_2O_7$ (*c* = 19.176(6) Å, *c/a* = 4.988) [14], which is expected considering the smaller ionic radius of Tb, Dy, Ho, or Er as compared to La. The slight decrease of *c/a* ratio suggests that the lattice contracts preferably in the *c*-direction rather than in the *a*-direction when La is substituted by other rare earth ions, as previously found for Ce, Pr, Nd, Sm, Gd [14,16,17]. For all samples the mean crystallite size was found to be around 25 nm.

Table 1. Lattice parameters, *c/a* ratio and crystallite sizes estimated from XRD patterns

	a (Å)	*c* (Å)	*c/a*	Crystallite size (nm)
$La_{1.2}Tb_{0.2}Ca_{1.6}Mn_2O_7$	3.835(6)	19.050(0)	4.966(6)	22±1
$La_{1.2}Dy_{0.2}Ca_{1.6}Mn_2O_7$	3.838(9)	19.100(9)	4.975(6)	23±1
$La_{1.2}Ho_{0.2}Ca_{1.6}Mn_2O_7$	3.839(2)	19.094(7)	4.973(6)	27±1
$La_{1.2}Er_{0.2}Ca_{1.6}Mn_2O_7$	3.848(7)	19.141(4)	4.973(4)	24±1

The magnetic properties of $La_{1.2}R_{0.2}Ca_{1.6}Mn_2O_7$ with R = Tb, Dy, Ho, and Er perovskites were studied by analyzing the temperature dependence of the zero field cooling (ZFC) and field cooling (FC) magnetizations under a magnetic field of 0.2 T (Fig. 2).

The curves presented in Fig. 2 show a wide ferromagnetic transition, change in slope in the temperature range of 50 – 200 K. The Curie temperature, defined as the temperature corresponding to the maximum of $|\delta M/\delta T|$, is in the range 70 K to 80 K for all samples, as it can be seen in the insets of Fig. 2. The wide ferromagnetic transition in double layered manganites is due to the appearance of short range 2D-magnetic order at temperatures higher than the 3D-ferromagnetic transition temperature [1,18], which is also responsible for the non zero magnetization value at room temperature. For all investigated perovskites, a clear splitting between the ZFC and FC magnetizations can be observed at low temperatures with a maximum of the ZFC curve at about 35 K. The difference between the FC and ZFC curves can be explained by the surface driven spin frustration and disorder in nanoparticles [19-21] together with the anisotropy originating from layered structure. This is supported by the reduced values of the magnetization at 5 K, that do not reach saturation even in magnetic fields of 12 T, as shown in Fig. 3 for $La_{1.2}R_{0.2}Ca_{1.6}Mn_2O_7$ with R = Tb, Dy, Ho, and Er. Also, the M(H) curves presented in Fig. 4 exhibit clear hysteresis at 5 K, which is diminishing with increasing temperature and is almost absent at 75 K.

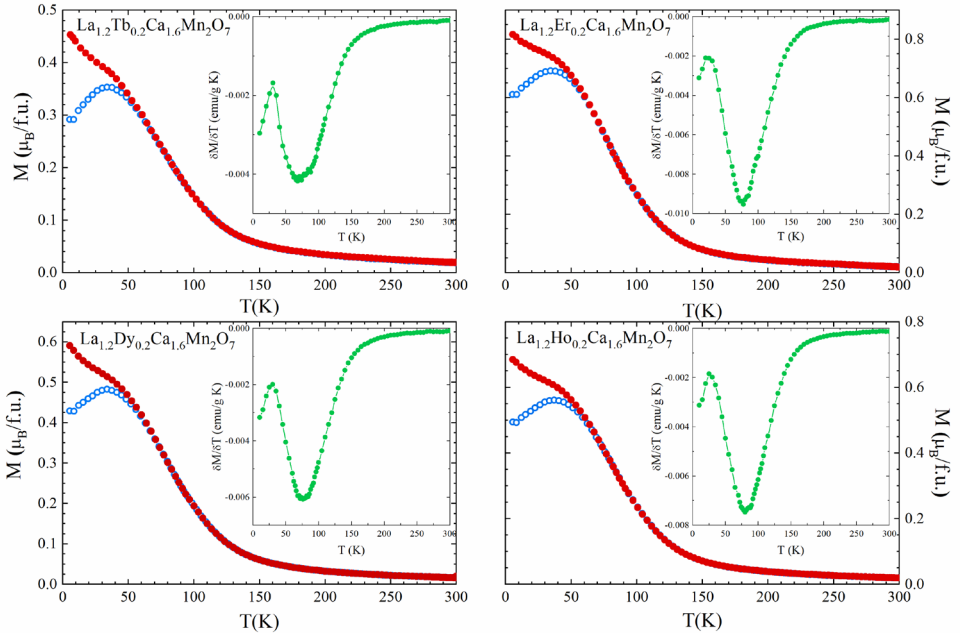

Fig. 2. Temperature dependence of ZFC (open symbols) and FC (filled symbols) magnetizations in 0.2T.

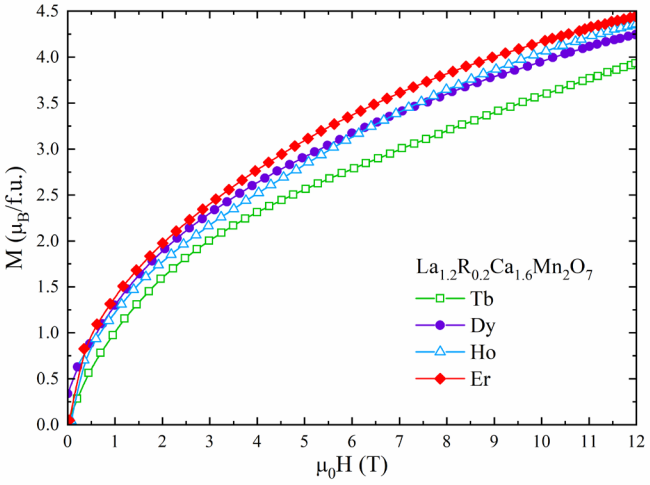

Fig. 3. *M(H)* curves at 5 K in magnetic fields up to 12 T.

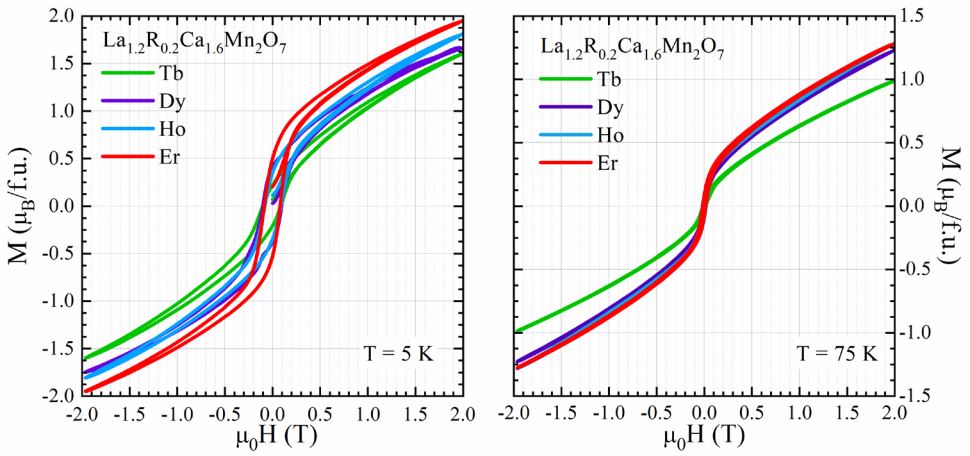

Fig. 4. Magnetic field dependence of the magnetization at 5 K (left) and 75 K (right).

Fig. 5 shows the temperature dependences of the magnetic entropy changes induced by a magnetic field change of 4 T for $La_{1.2}R_{0.2}Ca_{1.6}Mn_2O_7$ with R = Tb, Dy, Ho, and Er, as determined from magnetization isotherms using equation 2. For all samples the magnetic entropy change has a significant value over a broad temperature range, with a maximum at temperatures close to the magnetic transition ones.

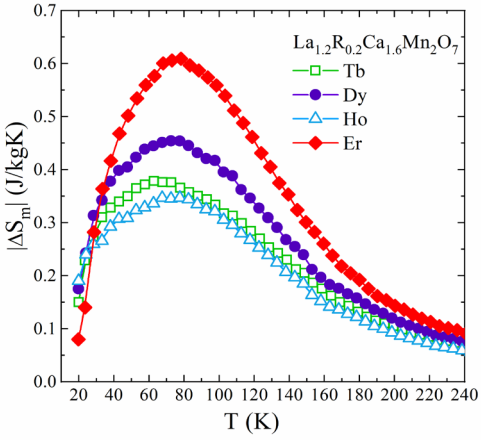

Fig. 5. Temperature dependence of the magnetic entropy changes ΔS_m for ΔH = 4 T.

The magnetocaloric properties of the investigated samples, including the *RCP(S)* values calculated by using equation 3, are presented in Table 2. The maximum values of $|\Delta S_m|$ are rather small since the magnetization of the samples in 4 T is far from the saturation value, but the *RCP(S)* values are high due to the broadened magnetic entropy curves.

Table 2. Magnetocaloric properties of $La_{1.2}R_{0.2}Ca_{1.6}Mn_2O_7$ perovskites

	T_C (K)	T_{max} (K)	$\|\Delta S_{Max}\|$ (J/KgK)	δT_{FWHM} (K)	*RCP(S)* (J/kg)
$La_{1.2}Tb_{0.2}Ca_{1.6}Mn_2O_7$	72±1	67±1	0.38±0.01	131±1	50±1
$La_{1.2}Dy_{0.2}Ca_{1.6}Mn_2O_7$	76±1	71±1	0.45±0.01	127±1	57±1
$La_{1.2}Ho_{0.2}Ca_{1.6}Mn_2O_7$	80±1	73±1	0.35±0.01	131±1	46±1
$La_{1.2}Er_{0.2}Ca_{1.6}Mn_2O_7$	77±1	76±1	0.61±0.01	118±1	72±1

CONCLUSIONS

Nanocrystalline $La_{1.2}R_{0.2}Ca_{1.6}Mn_2O_7$ with R = Tb, Dy, Ho, Er double layered manganites were successfully synthesized by a direct sol-gel method. The XRD analysis reveals that the partial substitution of La with smaller ions does not change the crystal structure and that the lattice contracts preferably in the *c*-direction rather than in the *a*-direction. The increased inter-layer lattice distortion leads to the reduction of the exchange interaction strength. The magnetic measurements show clear differences between FC and ZFC magnetizations at low temperatures for all four samples, which may be due to frustration of random competing ferromagnetic and antiferromagnetic interactions together with the anisotropy originating from layered structure. The magnetization at 4 K of $La_{1.2}R_{0.2}Ca_{1.6}Mn_2O_7$ manganites with R = Tb, Dy, Ho, Er does not saturate even in magnetic fields of 12 T. This may be due to the absence of true long-range FM coupling in the nanocrystalline samples obtained by the sol-gel method for which the grain size is smaller than 30 nm. A moderate magnetocaloric effect was found for all samples, with the maximum entropy change located at temperatures near the magnetic transition ones. The high *RCP(S)* values together with the broadened magnetic entropy curves and the absence of magnetic hysteresis at temperature higher than 50 K suggest the possibility to use these materials for magnetic refrigeration devices.

REFERENCES

[1] Y. Moritomo, A. Asamitsu, H. Kuwahara, Y. Tokura, Nature 380, 141-144 (1996).
[2] H. Asano, J. Hayakawa, M. Matsui, Phys. Rev. B 56, 5395 (1997).
[3] H. Asano, J. Hayakawa, M. Matsui, Appl. Phys. Lett. 70, 2303 (1997).
[4] N.H. Hur, J.T. Kim, K.H. Yoo, Y.H. Park, J.C. Park, E.O. Chi, Y.U. Kwon, Phys. Rev B 57, 10740 (1998).
[5] T. Kimura and Y. Tokura, Annu. Rev. Mater. Sci. 30, 451 (2000).
[6] Sandip Chatterjee, P.H. Chou, C.F. Chang, I.P. Hong, and H.D. Yang, Phys. Rev. B 61, 6106A (2000).
[7] C.D. Ling, J.E. Millburn, J.F. Mitchell, D.N. Argyriou, J. Linton, and H.N. Bordallo, Phys. Rev. B 62, 15096 (2000).
[8] Y. Moritomo, Y. Maruyama, T. Akimoto, and A. Nakamura, Phys. Rev. B 56 (1997) R7057-R7060.
[9] H. Asano, J. Hayakawa, and M. Matsui, Phys. Rev. B 57 (1998) 1052-1056.
[10] H. Asano, J. Hayakawa, and M. Matsui, Appl. Phys.Lett. 68, 3638-3641(1996).
[11] Tie-Jun Zhou, Z. Yu, W. Zhong, X.N. Xu, H.H. Zhang, and Y.W. Du, J. Appl. Phys. 85, 7975-7978 (1999).
[12] H. Zhu, H. Song, Y.H. Zhang, Appl. Phys. Lett. 81, 3416-3419 (2002).
[13] R. Tetean, C. Himcinschi, E. Burzo, J. Optoelectron. Adv. Mater. 10, 849-852 (2008).
[14] R. Dudric, F. Goga, S. Mican, R. Tetean, J. Alloy. Compd., 553, pp. 129–134 (2013).
[15] H.M Rietveld, J. Appl. Crystallogr. 2, 65 (1969).
[16] R. Dudric, F. Goga, M. Neumann, S. Mican, and R. Tetean , J. Mater. Sci. 47, 3125-3130 (2012).
[17] R. Dudric, F. Goga, F. Popa, and R. Tetean, Proceedings of The Romanian Academy – Series A 18, 2, 131-137 (2017).
[18] T. Kimura, Y. Tomioka, H. Kuwahara, A. Asamitsu, M. Tamura, and Y. Tokura, Science 274, 1698-1701 (1996).
[19] M.A. López-Quintela, L. E. Hueso, J. Rivas and F. Rivadulla, Nanotechnology 14, 212-219 (2004).
[20] S. Roy, I. Dubenko, D.D. Edorh, and N. Ali, J. Appl. Phys. 96, 1202-1207 (2004).
[21] P. Dey and T.K. Nath, Phys. Rev. B 73, 214425 (2006).

STUDIA UBB PHYSICA, Vol. 67 (LXVII), 1-2, 2022, pp. 17-24
(RECOMMENDED CITATION)
doi:10.24193/subbphys.2022.02

INVESTIGATION OF THE PHYSICAL PROPERTIES OF $MnNi_{(1-X)}M_X$ ALLOYS WHERE M=Ti, Al

R. HIRIAN[1], A. MERCEA[1], V. POP[1*]

ABSTRACT. $Mn_{50}Ni_{50-x}M_x$, where M= Ti, Al and x=0, 2.5, 5 and 10, alloys with the L10 crystal structure were successfully synthesized. The martensite type transformation was fond to be strongly affected by doping. Both x=10 samples show a spin glass type behavior while the sample doped with Al also shows large exchange bias.

Keywords: *hard magnetic materials, Mn based alloys, exchange bias, spin glass.*

INTRODUCTION

Permanent magnets are crucially important for modern industry. The high energy product $Nd_2Fe_{14}B$ and highly stable $SmCo_5$ or Sm_2Co_{17} based magnets permit the creation of highly compact devices, such as mobile phones and laptops, while also being excellent at delivering high performance for large applications such as wind turbines and electric vehicles [1-6]. However, the supply of rare-earth elements is tenuous and their extraction and processing has significant environmental impact, therefore a concerted scientific effort has been put forward in recent years towards developing magnetic materials from non-rare earth elements [4]. Amongst the proposed solutions are Mn based phases [2, 4], such as MnBi [7] and MnAl [8, 9], as they are low cost and present good magnetic properties. The useable magnetocrystalline anisotropy of these materials is given by the L10 crystal structure with high *c/a* ratio. In this work, we study the effect of doping on the L10 MnNi phase [10]. While this phase is antiferromagnetic, adequate doping may change the Mn-Mn distance leading to ferromagnetic coupling, similar to MnAl or MnBi.

[1] *Faculty of Physics, Babeş-Bolyai University, Cluj-Napoca, RO-400084 Romania*
** Corresponding author: viorel.pop@ubbcluj.ro*

EXPERIMENTAL

The $Mn_{50}Ni_{50-x}M_x$, where M=Ti, Al and x=0, 2.5, 5 and 10, alloys were produced by induction melting of the pure elements under purified argon atmosphere. The as-cast ingost were then placed in tantalum sample holders inside evacuated cuartz tubes and annealed at 1000 K for 48 h. In order to preserve formation of the high temperature structure, the samples were quenched in water.

Crystalline structure of the produced material was investigated using X-ray diffraction (XRD), on a Bruker D8 Advance diffractometer equipped with a Cu Kα source. The lattice parameters were calculated from XRD patterns using the Celref3 program.

Differential scanning calorimetry (DSC) measurements were carried out on a TA-Instruments Q600 simultaneous thermal analysis instrument. Measurements were done in high purity Ar flow, with a heating and cooling rate of 20 ^{o}C/min.

Thermomagnetic measurements were carried out on a Faraday-Weiss type magnetic balance, in the temperature range 300-900 K.

Magnetization measurements, along with zero-field cooled (ZFC) and field cooled (FC) measurements up to room temperature, were carried out using a vibrating sample magnetometer produced by Cryogenics.

RESULTS AND DISCUSSION

In order to determine the annlealing temperature of the $Mn_{50}Ni_{50-x}M_x$ alloys, DSC measurements were carried out in the temperature range between 600 K and 1100 K, *Figure 1*. These measurements show a phase transition around 1000 K for the undoped MnNi phase. This transition corresponds to the martensitic transformation between the low temperature and high temperature MnNi phase [10, 11]. In the case of both Ti and Al doping, *Figure 1a and 1b* respectively, we can see that the martensitic transformation shifts to lower temperature as doping is increased. The transformations for the x=10 samples are shifted below the measurement range of the instrument, i.e. below 600 K.

In order to obtain the L10 phase at room temperature, all samples were annealed for 48 h at 1000 K and quenched.

The X-Ray diffraction patterns for the annealed and quenched alloys are given in *Figure 2.* In the case of Al doping, *Figure 2b*, the structure of the L10 MnNi alloys is maintained for all doping ammounts. Of note are the shifts in peak

possitions due to the variations of lattice parameters. In the case of Ti doping, *Figure 2a*, the majority phase is the L10 MnNi phase, however some impurity peaks can bee seen for x=2.5 and x=10, to the right of the very intense [101] peak.

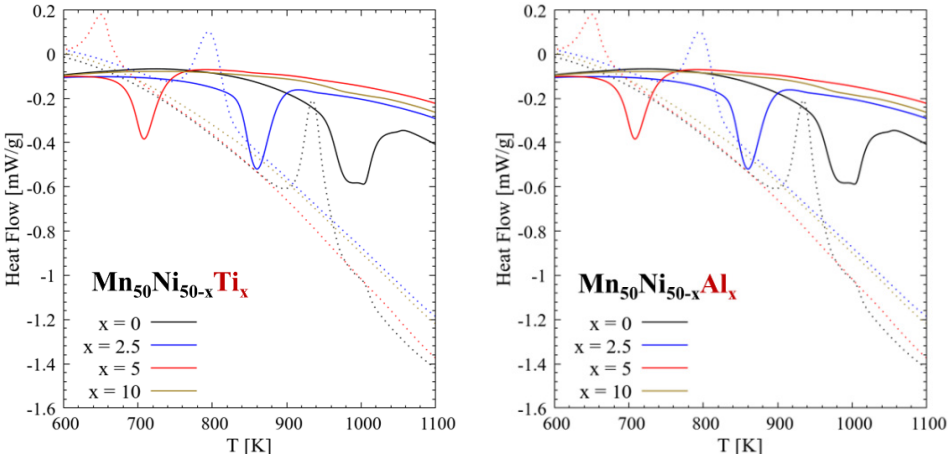

(a) (b)

Figure 1. DSC curves for $Mn_{50}Ni_{50-x}M_x$ alloys, where M is Ti (a) or Al (b). Cooling curves are dashed. Exotherms are displayed as peaks.

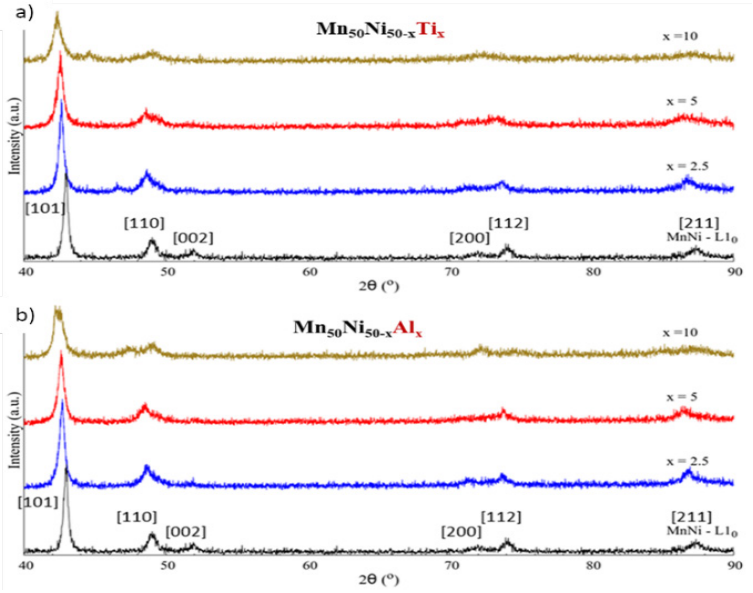

Figure 2. X-Ray diffraction patterns for the annealed and quenched $Mn_{50}Ni_{50-x}M_x$ alloys, where M is Ti (a) or Al (b).

The lattice paramenters for the doped alloys were estimated from XRD, using the space group P4/mmm, Table 1. For Al doping, the *a* parameter remains largely unchanged until x=10, when it contracts slightly. On the other hand, the MnNi cell is expanded on the *c* axis when Al is entered into the structure. This expansion cause an increase in the c/a ratio from 1.34 at x=0 to 1.40 at x=10. In the case of Ti doping, the same trend is observed, a significant contraction of the *a* parameter alongside an expansion of the *c* parameter for x=10.

Table 1. Lattice parameters, estimated from XRD, for the annealed and quenched $Mn_{50}Ni_{50-x}M_x$ alloys, where M is Ti or Al.

Composition	a (Å)	error	c (Å)	error	c/a ratio
x=0	2.641	0.008	3.534	0.003	1.34
M=Al x=2.5	2.641	0.016	3.541	0.014	1.34
M=Al x=5	2.655	0.005	3.557	0.004	1.34
M=Al x=10	2.632	0.003	3.681	0.031	1.40
M=Ti x=2.5	2.647	0.006	3.538	0.006	1.34
M=Ti x=5	2.648	0.040	3.556	0.013	1.34
M=Ti x=10	2.628	0.061	3.608	0.057	1.38

Thermomagnetic measurements (*Figure 3*) are in accordance with the DSC measurements, with magnetic transitions associated with the structural transformations, being measured around 900 K and 800 K for the samples with x=2.5 and x=5 respectively. It should be noted, that the thermomagnetic measurement range is larger than that used in DSC, *Figure 1*, therefore all of the phase transitions can be investigated. The Ti and Al doping at x=10 reduces the phase transition temperature to aproximately 400 K. In all cases, for the magnetic transitions, hysteresis is observed, which can be explained by the thermodynamics of phase transitions, specifically the undercooling and superheating imposed by the germination process.

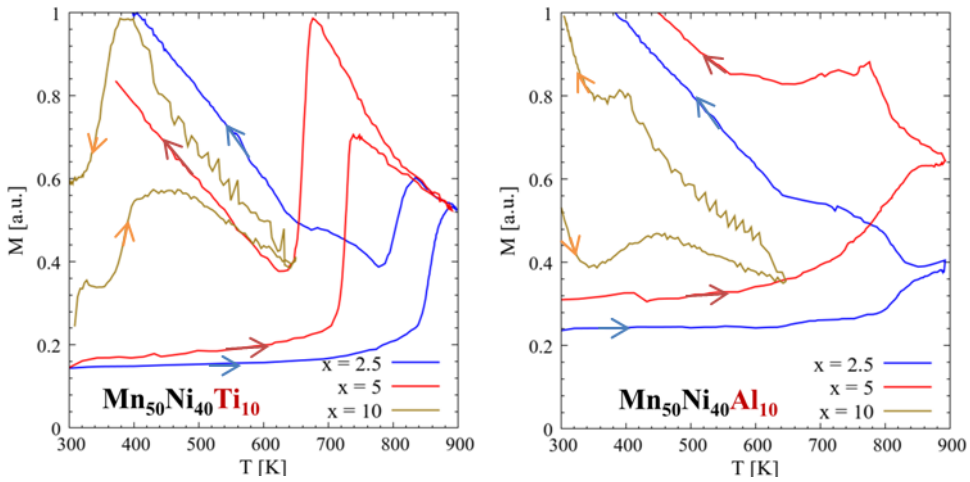

(a) (b)

Figure 3. Thermomagnetic measurements in small applied magnetic field, between 300 K and 900 K, for the annealed and quenched $Mn_{50}Ni_{50-x}M_x$ alloys, where M is Ti (a) or Al (b).

ZFC and FC curves for the x=10 alloys are shown in *Figure 4*. For the Ti doped alloy, *Figure 4a*, we see a large diffrence between the FC and ZFC curves, at low temperatures. The blocking temperature for these alloys is close to 70 K. In the case of Al doping, *Figure 4b*, while we still see a large difference between the ZFC and FC curves, the blocking temperature is much higher, around 140 K. At room temperature, a small peak appears, possibly a Neel temperature. Moreoever, this feature seems to show signs of thermal hysteresis. In the case of Al doping, similar low temperature features were observed to be due to a spin glass type behaviour [12]. Due to the similarity of the behaviour and composition, we may suspect that there is possible spin glass behaviour in the Ti doped sample as well.

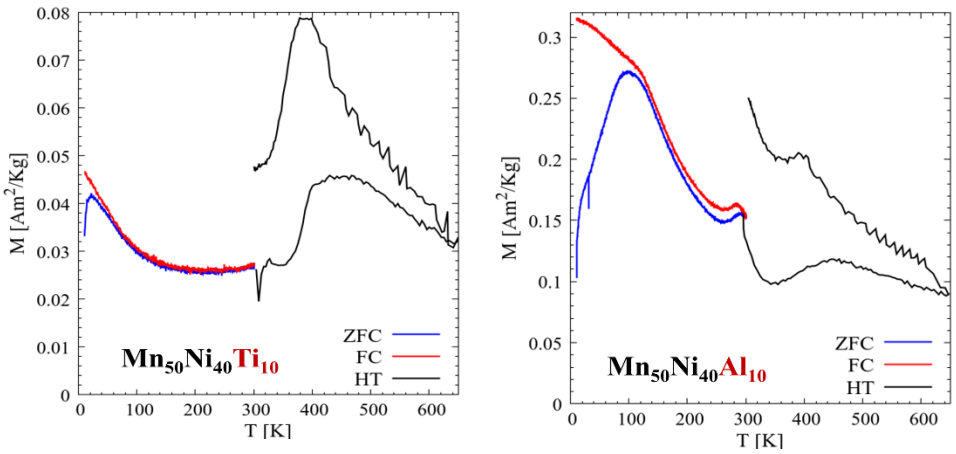

(a) (b)

Figure 4. ZFC and FC curves concatenated with high temperature measurements (HT) for the annealed and quenched $Mn_{50}Ni_{40}M_{10}$ alloys, where M is Ti (a) or Al (b).

Magnetization measurements for the x=10 samples are given in *Figure 5*. The samples measured at 4 K have been field cooled. Measurements at 4 K, for the Al doped sample (*Figure 5b*) show the existence of a large exchange bias, typical of the coexistence of ferromagnetic and antiferromagnetic interactions. The exchange bias disappears at high temperature, 300 K and 500 K. At elevated temperature, although the behaviour seems largely paramagnetic, the slight change in slope around 0 T indicates the presence of some non-compensated negative magnetic interaction.

The analysis of the magnetization curves is also similar to that of Ti doping at high temperature (*Figure 5a*) however the exchange bias seen at 4 K in the case of Al doped samples completely disappears when doping with Ti. At higher temperatures, the Ti doped samples show some magnetic order, likely due to uncompesate negative magnetic interactions.

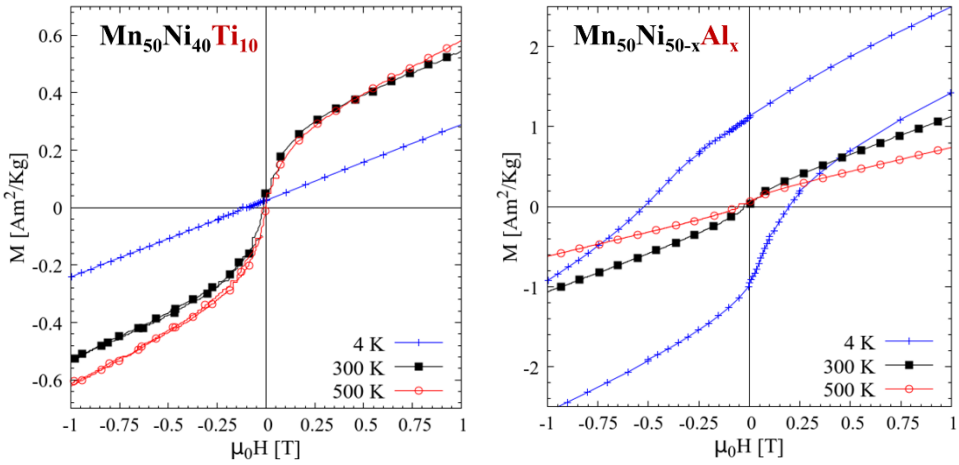

Figure 5. Magnetization measurements at 4 K, 300 K and 500 K, for the annealed and quenched $Mn_{50}Ni_{40}M_{10}$ alloys, where M is Ti (a) or Al (b).

CONCLUSIONS

$Mn_{50}Ni_{50-x}M_x$, where M= Ti, Al and x=0, 2.5, 5 and 10, alloys with the L10 crystal structure were successfully synthesized. Both Ti and Al doping produces distorsions of the L10 MnNi lattice. At doping amounts of x=10, the *c/a* ratio is significantly increased.

Doping also lowers the martensite transformation temperature, from 900 K for x=0 to 400 K for x=10.

In the case of $Mn_{50}Al_{40}M_{10}$ alloys, for both M=Ti and M=Al doping, the samples show a spin glass type behaviour at low temperatures.

The $Mn_{50}Al_{40}Al_{10}$ alloys show a large exchange bias at low temperatures. This feature is absent in the Ti doped sample.

AKNOWLEGEMENT

This work was made possible through the financial support of the Romanian Ministry of Research, Innovation and Digitalization, grant PN-III-P2- 2.1-PED-2019-4696.

REFERENCES

[1] D. Sander, S. O. Valenzuela, D. Makarov, C. H. Marrows, E. E. Fullerton, P. Fischer, J. McCord, P. Vavassori, S. Mangin, P. Pirro, et al. *J. Phys. D. Appl. Phys.* 50 (2017), doi:10.1088/1361-6463/aa81a1.

[2] J.M.D. Coey, *IEEE Trans. Magn.* 47, 4671-4681, (2011) doi:10.1109/TMAG.2011.2166975.

[3] D. Goll, H. Kronmüller,*Naturwissenschaften* 87, 423-438, (2000) doi:10.1007/s001140050755.

[4] J. M. D. Coey, *Engineering* 6, 119–131, (2020) doi:10.1016/j.eng.2018.11.034.

[5] N.T. Nassar, X. Du, T.E. Graedel, *J. Ind. Ecol*. 19, 1044–1054, (2015) doi:10.1111/jiec.12237.

[6] K. Binnemans, P.T. Jones, B. Blanpain, T. Van Gerven, Y. Yang, A. Walton, M. Buchert, *J. Clean. Prod.* 51, 1–22, (2013) doi:10.1016/j.jclepro.2012.12.037.

[7] R. Hirian, R. Dudric, O. Isnard, K. Kuepper, M. Coldea, L. Barbu-Tudoran, V. Pop, D. Benea, *J. Magn. Magn. Mater*. 532, 167997, (2021), doi:10.1016/j.jmmm.2021.167997

[8] S. Mican, D. Benea, R. Hirian, R. Gavrea, O. Isnard, V. Pop, M. Coldea, *J. Magn. Magn. Mater*. 401, 841-847, (2016), doi: 10.1016/j.jmmm.2015.11.011

[9] R. Gavrea, R. Hirian, S. Mican, D. Benea, O. Isnard, M. Coldea, V. Pop, *Intermetallics*, 82, 101-106, (2017), doi: 10.1016/j.intermet.2016.11.012

[10] E. Kren, E. Nagy, I. Nagy, L. Pal, P. Szabo, *J. Phys. Chem. Solids*, 29, 101-108, (1968), doi:10.1016/0022-3697(68)90259-X

[11] V. Rednic, M. Coldea, S.K. Mendiratta, M. Valente, V. Pop, M. Neumann, L. Rednic, *J. Magn. Magn. Mater*. 321, 3415-3421, (2009) doi: 10.1016/j.jmmm.2009.06.020

[12] H. Pan, Li Ma, G. K. Li, L. Y. Jia, C. Zhen, D.-L. Hou, W. Wang, E. Liu, J. L. Chen, G.H. Wu, *Intermetallics*, 86, 116-120, (2017) doi:10.1016/j.intermet.2017.03.003

STUDIA UBB PHYSICA, Vol. 67 (LXVII), 1-2, 2022, pp. 25-33
(RECOMMENDED CITATION)
doi:10.24193/subbphys.2022.03

MAGNETIC PROPERTIES OF $(Fe,Co)_5SiB_2$ ALLOYS BY W DOPING

R. HIRIAN[1*], V. POP[2], O. ISNARD[2,3], D. BENEA[1]

ABSTRACT. The intrinsic magnetic properties (magnetic moments, magneto-crystalline anisotropy, Curie temperatures) of the $Fe_{5-x-y}Co_yW_xSiB_2$ alloys have been calculated using the spin-polarized relativistic Korringa-Kohn-Rostoker (SPRKKR) band structure method. Our calculations show that for several compounds with $x \geq 0.5$, the magnetocrystalline anisotropy energy (MAE) became axial. Also, theoretical calculations for Fe_4WSiB_2 compound found a magnetization decrease (with about 20%), a Curie temperature decrease of about 30% but an increased axial magnetocrystalline anisotropy compared with the corresponding values for Fe_5SiB_2. Several $Fe_{5-x}W_xSiB_2$ alloys (x = 0, 0.1, 0.2, 0.5, 1) have been prepared by arc melting of corresponding high purity elements in Ar controlled atmosphere. Composition analysis of the $Fe_{5-x}W_xSiB_2$ alloys found an impurity phase along with the tetragonal *I4/mcm* phase of pure Fe_5SiB_2. The magnetic measurements found the decrease of the magnetization any significant increase of the coercivity due to W doping.

Keywords: *ab-initio calculations, B. magneto-crystalline anisotropy, C. magnetization, D. rare earth free magnets.*

INTRODUCTION

Magnetic materials are main components of many devices, and their development, impact and innovation are crucial on raising energy efficiency in many economic sectors. Permanent magnets are used widely in advanced technologies

[1] *Faculty of Physics, Babeş-Bolyai University, Cluj-Napoca, Kogălniceanu str. 1, 400084 Cluj-Napoca, Romania.*
[2] *Université Grenoble Alpes, Institut Néel, Grenoble, F-38042, France.*
[3] *CNRS, Institut Néel, 25 rue des Martyrs, F-38042 Grenoble, France.*
* *Corresponding author: razvan.hirian@ubbcluj.ro*

including electric vehicles, memory devices, electric motors, windmills, transportation, magnetic levitation or biomedical devices (including magnetic resonance imaging machines, pacemakers, heart pumps, etc.). A route to build performant magnets with lower prices is to develop rare-earth-free magnets that can fill in the gap between the chip hard ferrite and high performant by expensive rare-earth magnets [1].

A promising class of materials which can be explored is based on Fe_5SiB_2 alloy, due to their intrinsic properties (Tc > 800 K, M_s ~ 9 μ_B/f.u. and K_1~-0.30 MJ/m^3). According to our previous studies [2], the magnetization decreases at 1.46 μ_B/f.u. in Co_5SiB_2 alloys. Also, the Curie temperature is reduced by Co for Fe substitution [2]. The magnetocrystalline anisotropy energy (MAE) is negative for Fe_5SiB_2, but its absolute magnitude decreases by Co for Fe substitution. To build performant permanent magnets, the materials should have (i) ferromagnetic ordering with a high Curie temperature, (ii) large saturation magnetization and (iii) a strong magnetic anisotropy of the easy-axis type [3], first two conditions being fulfilled by Fe_5SiB_2 alloy. The Co for Fe substitution in $Fe_{5-x-y}Co_yW_xSiB_2$ is able to turn the sign of MAE from negative to positive for $1.5 \leq y \leq 2.5$, enabling an axial easy magnetization axis for the corresponding alloys [2]. On the other hand, previous studies [4] showed that doping of Fe_5PSi_2 alloy with a *5d* element would induce a strong uniaxial anisotropy, allowing to build a semi-hard magnet which can be used in nanocomposite magnetic materials. In the present study the W doping of the $Fe_{5-y}Co_ySiB_2$ alloys has been considered, accounting for both axial anisotropy of the alloys with $1.5 \leq y \leq 2.5$ as well as for the strong spin-orbit coupling of the *5d* element which could enhance the axial anisotropy of the W doped alloys. Theoretical and experimental studies on the structural and magnetic properties of $Fe_{5-x-y}Co_yW_xSiB_2$ alloys are presented in the following.

COMPUTATIONAL AND EXPERIMENTAL DETAILS

Spin-polarized fully relativistic Korringa-Kohn-Rostoker (SPRKKR) band structure method has been used for theoretical calculations [5]. The exchange and correlation effects have been accounted for by means of the generalized gradient approximation with the parametrization of Perdew et al. (GGA-PBE) [6]. The k-space integration was performed using the special points method [7]. The substitutional disorder in the system has been treated within the Coherent Potential Approximation (CPA) theory [8]. The study of the magnetic anisotropy has been performed by magnetic torque calculations acting on the magnetic moment $\overrightarrow{m_i}$ of the atomic site *i,* oriented along the magnetization direction $\vec{M}$ [9,10]. The component of the magnetic

torque with respect to axis $\hat{u}$ is $T_{\hat{u}}(\theta,\varphi) = -\partial E(\overrightarrow{M}(\theta,\varphi))/\partial\theta$, where θ and φ are the polar angles. The magnetic torque and the energy difference between the in-plane and out-of-plane magnetization directions are related by a special geometry. By setting the angles to $\theta = \pi/4$ and $\varphi = 0$, the calculated magnetic torque is $T_{\hat{u}}(\pi/4,0) = E_{[100]} - E_{[001]}$ [10]. A complementary approach to investigate the magnetic behaviour of is based on the classical Heisenberg Hamiltonian described by the expression:

$$H_{ex} = -\sum_{ij} J_{ij}\hat{e}_i \cdot \hat{e}_j ,$$

where the summation is performed on all lattice sites *i* and *j* and $\hat{e}_i$ / $\hat{e}_j$ are the unit vectors of magnetic moments on sites *i* and *j,* respectively. The J_{ij} exchange coupling parameters for all magnetic atoms have been calculated as a function of distance using the expression derived by Liechtenstein [11] based on the magnetic force theorem. The Curie temperatures have been derived using the J_{ij} exchange coupling parameters within the mean field approach [11,12],

$$T_c^{rough-MFA} = \frac{2}{3k_B}\sum_i J_{0i} ,$$

where J_{0i} is the exchange-coupling parameters sum over all coordination shells up to 15 Å around lattice site *i*.

The synthesis of the polycrystalline $Fe_{5-x}W_xSiB_2$ alloys (x = 0, 0.1, 0.2, 0.5, 1) alloys has been performed following the arc melting procedure described elsewhere [2] starting from high purity elements (99.999% Fe, 99.99% Si, 99.5% W, 99.7% B), under high purity Ar atmosphere. Each sample was turned and re-melted several times, to ensure homogeneity.

The crystalline structure of the samples was investigated by X-Ray diffraction (XRD), using a Bruker D8 Advance diffractometer equipped with a Cu K_α radiation. The phase content of the annealed alloys was determined using the Rietveld method. In order to compare the data recorded with different wavelengths, the XRDs are plotted versus $1/d_{hkl}$. The lattice parameters of the different samples were determined using the Celref 3 software [13] from least square measurements taking all the Bragg peaks observed into account. Magnetization measurements were carried out using a VSM magnetometer in applied field of up to 4 T (4 K – 300 K).

RESULTS AND DISCUSSIONS

The electronic band structure calculations for the $Fe_{5-x-y}Co_yW_xSiB_2$ (x = 0.0, 0.15, 0.25, 0.5, 1.0; y = 0.0, 1.0, 1.5 and 2.0;) in tetragonal structure (space group *I4/mcm*) using the experimental lattice parameters [2, 14] have been performed. The lattice constants of the W-doped alloys have been evaluated using the experimental lattice constants [2,14,15] and considering their linear dependence with W content x. The random occupation of W atoms of the *4c* and *16l* crystal sites has been considered. Calculated magnetic moments (in Bohr magnetons μ_B) for the $Fe_{5-x-y}Co_yW_xSiB_2$ (x = 0, 0.15, 0.25, 0.5, 1.0 and y = 0, 1.0, 1.5 and 2.0) are shown in Table 1.

According to our calculations, Fe_5SiB_2 alloy is ferromagnetic with a total magnetic moment of 9.24 μ_B/f.u., in plane easy axis with the calculated anisotropy constant K_1 = -0.206 meV/f.u.. The Curie temperature calculated by mean field approach is 1140 K. As the mean field method is known to overestimate by ~20% the Curie temperature values, the estimated T_c would be comparable with the experimental value of 850 K [2].

Table 1. Calculated magnetic moments, MAE constant K_1 and the estimated Curie temperature for the $Fe_{5-x-y}Co_yW_xSiB_2$ alloys (x = 0.0, 0.15, 0.25, 0.5, 1.0; y = 0.0, 1.0, 1.5 and 2.0). Preferential occupation of W for *4c* sites has been considered

	lattice const. *a,c* (Å)	**m_s (μ_B/f.u.)**	**m_l (μ_B/f.u.)**	**K_1 (meV/f.u.)**	**T_c (K)**
Fe_5SiB_2	5.5446; 10.336	9.03	0.215	-0.206	1140
$Fe_{3.5}Co_{1.5}SiB_2$	5.5174; 10.2464	6.92	0.20	-0.05	761
Fe_4WSiB_2	5.6425; 10.4744	7.75	0.22	0.218	747
$Fe_{3.35}Co_{1.5}W_{0.15}SiB_2$	5.5505; 10.2413	6.35	0.187	-0.05	638
$Fe_{3.25}Co_{1.5}W_{0.25}SiB_2$	5.559; 10.255	6.70	0.20	-0.055	509
$Fe_{3.5}CoW_{0.5}SiB_2$	5.59 ;10.33	6.88	0.20	-0.038	545
$Fe_{3.0}Co_{1.5}W_{0.5}SiB_2$	5.5834; 10.29	6.14	0.20	0.024	408
$Fe_{2.0}Co_{2.0}WSiB_2$	5.63; 10.32	4.81	0.18	0.105	210
$Fe_{3.0}CoWSiB_2$	5.6376; 10.3942	6.28	0.20	0.067	414

As can be seen in Table 1, Co doping in Fe_5SiB_2 reduces the total magnetic moment and the Curie temperature of the alloys, as shown in our previous experimental and theoretical investigations [2]. Also, Co doping up to y = 1.5 reduces the absolute

value of the anisotropy constant K_1 to -0.05 meV/f.u.. On the other hand, by W for Fe substitution the anisotropy is turning to axial in Fe_4WSiB_2 with K_1 value of 0.218 meV/f.u, corresponding to 0.22 MJ/m^3. This improved anisotropy is accompanied by a decrease of total magnetic moment (8.97 μ_B/f.u.) and a lower Curie temperature (747 K). If the W doping is performed in the $Fe_{3.5}Co_{1.5}SiB_2$ alloy which has small negative value of K_1, the anisotropy is negative up to y = 0.5. Unfortunately, increasing the W content with x > 0.5 in $Fe_{5-x-y}Co_yW_xSiB_2$ (y = 1.0, 1.5 and 2.0) would induce a strong decrease of T_c.

For $Fe_{2.0}Co_{2.0}WSiB_2$ which has axial anisotropy (K_1 = 0.105 meV/f.u.), the Curie temperature is under room temperature and in this way, the obtained magnet would not be able to operate in a reasonable temperature range. In conclusion, the theoretical study proposes Fe_4WSiB_2 alloy as possible candidate for permanent magnet applications due to its increased anisotropy and relatively high values of Curie temperature and total magnetic moment.

The XRD patterns for the $Fe_{5-x}W_xSiB_2$ alloys (x=0.1, 0.2, 0.5 and 1.0) presented in Fig. 1 show the presence of tetragonal phase (*I4/mcm* space group) in all obtained samples. However, for higher W content (x > 0.5) one can see a mixture of phases within the samples. Also, the thermomagnetic measurements found no trace of free Fe in all samples. The lattice constants obtained by refining the XRD patterns from Fig. 1 are shown in Table 2.

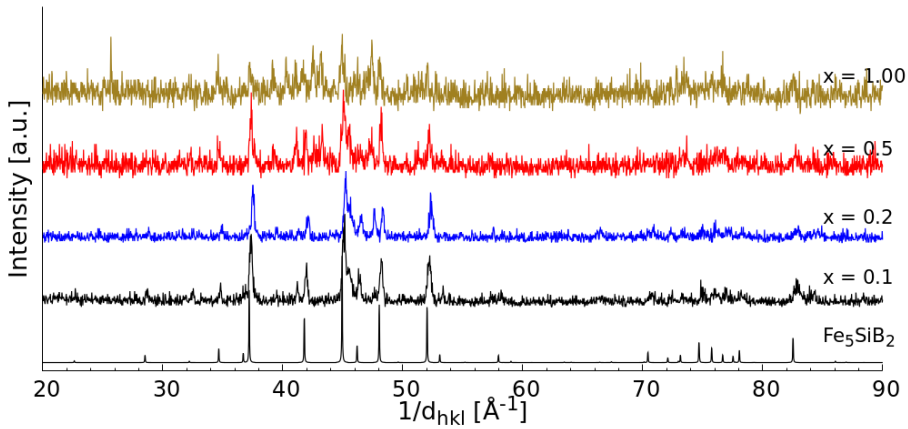

Fig. 1. The XRD patterns for the $Fe_{5-x}W_xSiB_2$ alloys (x=0.1, 0.2, 0.5 and 1.0). The computed XRD pattern for Fe_5SiB_2 is shown for comparison.

Table 2. Lattice constants determined experimentally for the $Fe_{5-x}W_xSiB_2$ alloys

x	Lattice constants (Å)	
	a	c
0.1	5.54(2)	10.31(2)
0.2	5.53(2)	10.28(2)
0.5	5.52(2)	10.26(2)
1.0	5.54(2)	10.37(2)

The thermomagnetic measurements for the $Fe_{5-x}W_xSiB_2$ alloys by heating (a) and by cooling (b) are shown in Fig. 2. By heating, the presence of three different magnetic phases can be evidenced, whilst by cooling only two magnetic phases are present. One of them is the Fe_5SiB_2 phase type with Curie temperatures between 768 (for x = 0.5) and 850 K (for x = 0.1) and the other is a magnetic impurity phase with Curie temperatures between 503 and 553 K, as can be seen in Fig. 2b and Fig. 3.

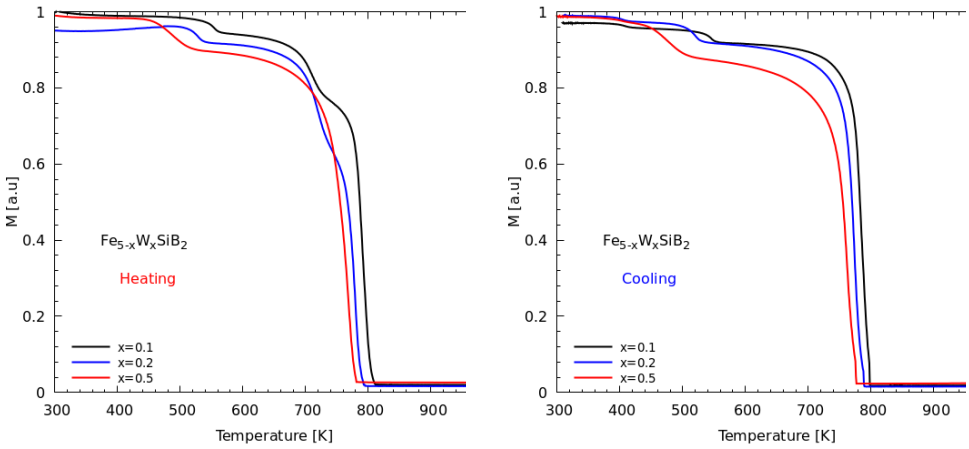

Fig. 2. Temperature dependence of the magnetization for the $Fe_{5-x}W_xSiB_2$ alloys by (a) heating and (b) cooling of the samples.

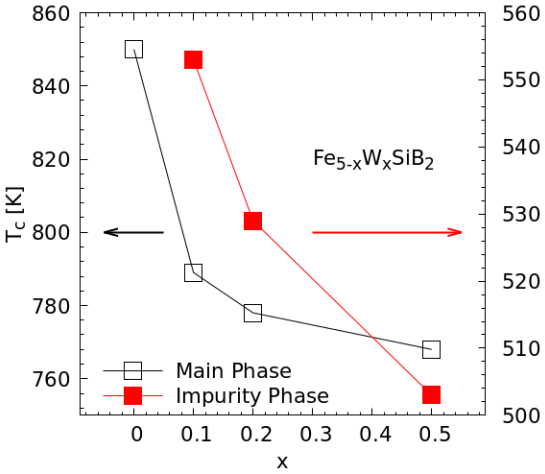

Fig. 3. Composition dependence of the Curie temperatures for the $Fe_{5-x}W_xSiB_2$ alloys. The Curie temperatures of the impurity sample are shown by full squares.

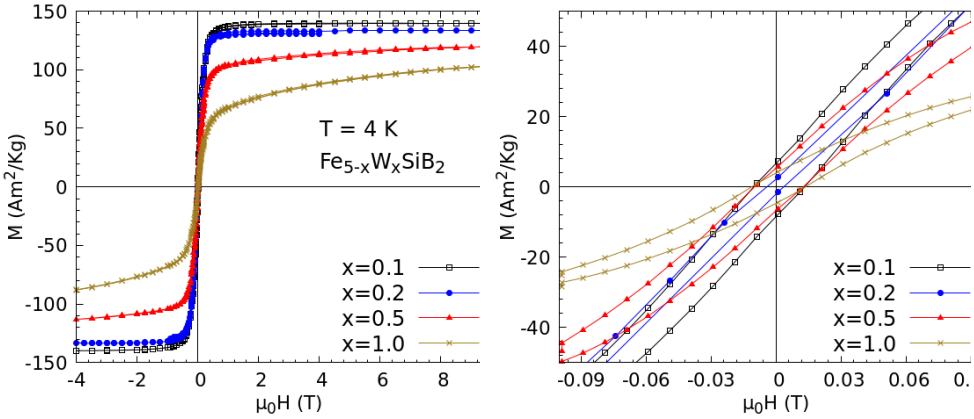

(a) **(b)**

Fig.4. (a) Magnetic hysterezis curves measured at 4 K for the $Fe_{5-x}W_xSiB_2$ alloy and (b) hysterezis curves around the origin for the same system.

The Curie temperatures evolution vs. W content x (Fig. 3) shows that both phases contain Fe and W. The partial substitution of Fe with W reduces the Curie temperature of the corresponding Fe_5SiB_2-doped phases. Accounting for the Curie temperature evolution in the Fe-Si phases [16], the impurity phase is supposed to be the solid solution of Si+W in Fe (α_1 phase).

The hysterezis curves obtained by magnetic measurements (Fig. 4) show a fast saturation of the samples with low W content as well as an anisotropy increase by increasing the W content x. The details of the hysterezis curves around the origin show a low coercivity of the measured samples. Magnetic measurements of the alligned mono-domanines samples would offer a better image on the sample coercivity. Also, the improvement of the present study is intended by using more complex preparation methods, by mechanical alloying or fast cooled ribbons, in order to diminish the impurity phases percentage.

CONCLUSIONS

Theoretical studies on the $Fe_{5-x-y}Co_yW_xSiB_2$ alloys show the decrease of total magnetic moment and Curie temperatures of the alloys by increasing W content x. Also, the theoretical calculated MAE turns from planar for Fe_5SiB_2 alloy to axial for Fe_4WSiB_2 and for $Fe_{5-x-y}Co_yW_xSiB_2$ alloys with W content $x > 0.5$. The experimental investigations show that the samples are mixed phases for magnetic alloys of interest (axial anisotropy, $x > 0.5$). The experimental measured magnetizations and Curie temperatures show agreement with the corresponding theoretical calculations. The improvement of intrinsic magnetic properties for Fe_5SiB_2 alloys by W doping in the investigated doping range is reduced due to the phase mixture appearance. Still, the intrinsic properties of the W doped $Fe_{5-y}Co_ySiB_2$ alloys might be improved by reduction of the impurity phase, which can be obtained using more complex preparation methods.

ACKNOWLEDGEMENTS

The financial support from the Romanian Ministry of Education and Romanian Ministry of Research and Innovation, CCCDI-UEFISCDI grant PN-III-P2-2.1-PED-2019-3484 is acknowledged.

REFERENCES

[1] J. Cui, M. Kramer, L. Zhou et al, *Acta Materialia* 158 118 (2018).
[2] R. Hirian, O. Isnard, V. Pop and D. Benea, *J. Magn. Magn. Mater.* 505 166748 (2020).
[3] R. Skomski and J. M. D. Coey, *Scripta Mater.* 112 3 (2016).
[4] J. Thakur, P. Rani, M. Tomar, V. Gupta and M. K. Kashyap, AIP Conf. Proc. 2093, 020012 (2019)

[5] H. Ebert, D. Ködderitzsch and J. Minar, *Rep. Prog. Phys*, 74 096501 (2011).
[6] J. P. Perdew, K. Burke, M. Ernzerhof, *Phys. Rev. Lett.* 77 3865 (1996).
[7] H. Monkhorst and J. Pack, *Phys. Rev.* B 13, 5188 (1976).
[8] J. S. Faulkner, Prog. Mater. Sci. 27 1 (1982); J. S. Faulkner and G. M. Stocks, *Phys. Rev. B* 21 3222 (1980).
[9] J. B. Staunton, L. Szunyogh, A. Buruzs, B. L. Gyorffy, S. Ostanin, and L. Udvardi, *Phys. Rev. B* 74 144411 (2006).
[10] S. Mankovsky, S. Polesya, J. Minar, F. Hoffmann, D.H. Back and H. Ebert, *Phys. Rev. B* 84 201201 (2011).
[11] A.I. Liechtenstein, M. I. Katsnelson,V. P. Antropov and V. A. Gubanov, *J. Magn. Magn. Mater.* 67 65 (1987).
[12] P. Nieves, S. Arapan, J. Maudes-Raedo, R. Marticorena-Sánchez, N.L. Del Brío, A. Kovacs, C. Echevarria-Bonet, D. Salazar, J. Weischenberg, H. Zhang, O.Yu. Vekilova, R. Serrano-López, J.M. Barandiaran, K. Skokov, O. Gutfleisch, O. Eriksson, H.C. Herper, T. Schrefl, S. Cuesta-López, *Comput. Mat. Sci.* 168 188 (2019).
[13] LMGP-Suite of Programs for the interpretation of X-ray Experiments, by Jean Laugier and Bernard Bochu, ENSP/Laboratoire des Matériaux et du Génie Physique, BP 46. 38042 Grenoble, France. WWW: http://www.inpg.fr/LMGP and http://www.ccp14.ac.uk/tutorial/lmgp/.
[14] M. Werwiński, S. Kontos, K. Gunnarsson, P. Svedlindh, J. Cedervall, V. Höglin, M. Sahlberg, A. Edström, O. Eriksson, and J. Rusz, Phys. Rev B 93 174412 (2016).
[15] K. Fukuma et al., *J. Phys. Soc. Jpn.* 80 024702 (2011).
[16] T.B. Massalski, et al., Binary Alloy Phase Diagrams, ASM International (1990).

STUDIA UBB PHYSICA, Vol. 67 (LXVII), 1-2, 2022, pp. 35-41
(RECOMMENDED CITATION)
doi:10.24193/subbphys.2022.04

CONDUCTANCE OF AN ONE AND DOUBLE-LEVEL QUANTUM DOT

I. GROSU[1]

ABSTRACT. We analytically study the expression of the electric charge current through a two-terminal quantum dot in the linear response approximation. We analyse the one-level and the two-level quantum dot scaled conductance taking into account the relevant parameters. We also present the results for the conductance in the Sommerfeld approximation.

Keywords: *Electrical conductance, Quantum dots, Linear response.*

I. INTRODUCTION

The transport of electric charge through solids has been studied for many decades with the aim of finding new analytical results as well as important experimental applications [1]. The dimensionality effects can strongly affect the properties of the materials, in particular the electrical conduction [2]. These effects also change the thermoelectric properties of the materials [3]. Here the quantum coherence effects are more important than the general properties of a bulk material [4-6]. The main ingredient in the description of transport phenomena in these materials is the transmission function $T(\varepsilon)$[7,8]. It contains microscopic information about the sample and its connections with the leads. In this paper we analyse the charge current response of a quantum dot in contact with two particle reservoirs. First we will analyse the single-level quantum dot case with symmetric coupling (γ_0) to the leads. Then we will study the current conductance of a double-level quantum dot with $t_c$the coupling strength between the two levels of the quantum dot.

[1] *Babes-Bolyai University, Faculty of Physics, 1 Kogalniceanu str., 400084 Cluj-Napoca, Romania. Email: ioan.grosu@ubbcluj.ro.*

II. MODEL

The transport theory, in the case of thermoelectric phenomena, allows the determination of the electrical conductance through the expression [7]

$$G = e^2 L_0 \tag{1}$$

where e is the electron charge, and L_0 is the quantity

$$L_0 = \frac{1}{h}\int_{-\infty}^{\infty} d\varepsilon T(\varepsilon)\left(\frac{-\partial f_{FD}}{\partial \varepsilon}\right) \tag{2}$$

Here h is the Planck's constant, $T(\varepsilon)$ the transmission function, and f_{FD} is the Fermi-Dirac distribution function defined as ($\mu = 0$, μ is the chemical potential).

$$f_{FD} = \frac{1}{e^{(\varepsilon/k_B T)}+1} \equiv \frac{1}{2} - \frac{1}{2}\tanh\left(\frac{\varepsilon}{2k_B T}\right) \tag{3}$$

where k_B is the Boltzmann's constant, and T the temperature. With the new variable $z = \varepsilon/k_B T$, L_0 becomes

$$L_0 = \frac{-1}{h}\int_{-\infty}^{\infty} dz T\,(k_B T z)\frac{\partial f_{FD}(z)}{\partial z} \tag{4}$$

For accurate analytical calculations we express the Fermi-Dirac function through the series [9]

$$f_{FD}(z) = \frac{1}{2} - \sum_{n=-\infty}^{\infty} \frac{1}{z - 2\pi i\left(n+\frac{1}{2}\right)} \tag{5}$$

Now we will use equations (4) and (5) in order to calculate first the scaled (G/e^2) conductance of a single level quantum dot [10]. In this case the transmission function is given by

$$T(\varepsilon) = \frac{\gamma_0^2}{(\varepsilon-\varepsilon_0)^2+\gamma_0^2} \tag{6}$$

which, with the z variable, can be rewritten as

$$T(k_B T z) = 2\Re\left[\frac{i\widetilde{\gamma_0}}{2}\frac{1}{z-\widetilde{\varepsilon_0}+i\widetilde{\gamma_0}}\right] \tag{7}$$

where: $\widetilde{\gamma_0} = \gamma_0/k_B T$, and $\widetilde{\varepsilon_0} = \varepsilon_0/k_B T$ v are scaled quantities. With these results:

$$L_0 = \frac{-\widetilde{\gamma_0}}{h}\Re\left[i\sum_n \int_{-\infty}^{\infty} dz \frac{1}{z-\widetilde{\varepsilon_0}+i\widetilde{\gamma_0}}\frac{1}{[z-2\pi i(n+\frac{1}{2})]^2}\right] \tag{8}$$

The integral in equation (8) is carried by closing the integration path in the upper complex plane to obtain [11]

$$\frac{-1}{2\pi i(n+\tilde{a})^2}; n = 0,1,2,\ldots \tag{9}$$

where:

$$\tilde{a} = \frac{1}{2} + \frac{i}{2\pi}(\widetilde{\varepsilon_0} - i\widetilde{\gamma_0}) \tag{10}$$

Using the fact that

$$\psi^{(1)}(\tilde{a}) = \sum_{n=0}^{\infty} \frac{1}{(n+\tilde{a})^2} \tag{11}$$

is the trigamma function [12], the scaled conductance will be

$$L_0 = \frac{\widetilde{\gamma_0}}{2\pi h} \Re\psi^{(1)}(\frac{1}{2} + \frac{\widetilde{\gamma_0}}{2\pi} + i\frac{\widetilde{\varepsilon_0}}{2\pi}) \tag{12}$$

an exact analytical result [11].

The second case we analyse is the two-levels quantum dot case. Here the transmission is given by [10]

$$T(\varepsilon) = \frac{\gamma_0^2}{(\varepsilon - \varepsilon_0 - \frac{t_c^2}{\varepsilon - \varepsilon_1})^2 + \gamma_0^2} \tag{13}$$

Following steps similar to the first case we will have

$$L_0 = \frac{-\widetilde{\gamma_0}}{h} \Re[i \sum_n \int_{-\infty}^{\infty} dz \frac{1}{z - \widetilde{\varepsilon_0} - \frac{\widetilde{t_c^2}}{z - \widetilde{\varepsilon_1}} + i\widetilde{\gamma_0}} \frac{1}{[z - 2\pi i(n + \frac{1}{2})]^2}] \tag{14}$$

If the tunneling parameter between levels (t_c) is small, $L_0$is reduced to

$$L_0 = \frac{-\widetilde{\gamma_0}}{h} \Re[i \sum_n \int_{-\infty}^{\infty} dz \frac{z - \widetilde{\varepsilon_1}}{(z - z_1)(z - z_2)} \frac{1}{(z - z_n)^2}] \tag{15}$$

where

$$z_1 = [\widetilde{\varepsilon_0} + \frac{\widetilde{t_c^2}\Delta\tilde{\varepsilon}}{(\Delta\tilde{\varepsilon})^2 + \widetilde{\gamma_0^2}}] - i\widetilde{\gamma_0}[1 - \frac{\widetilde{t_c^2}}{(\Delta\tilde{\varepsilon})^2 + \widetilde{\gamma_0^2}}] \equiv c - id \tag{16}$$

$$z_2 = [\widetilde{\varepsilon_1} - \frac{\widetilde{t_c^2}\Delta\tilde{\varepsilon}}{(\Delta\tilde{\varepsilon})^2 + \widetilde{\gamma_0^2}}] - i\frac{\widetilde{\gamma_0}\widetilde{t_c^2}}{(\Delta\tilde{\varepsilon})^2 + \widetilde{\gamma_0^2}} \equiv a - ib \tag{17}$$

$$z_n = 2\pi i(n + \frac{1}{2}) \tag{18}$$

and $\Delta\tilde{\varepsilon} = \widetilde{\varepsilon_0} - \widetilde{\varepsilon_1}$. After performing the contour integration and the summation we obtain

$$L_0 = \frac{2\pi\widetilde{\gamma_0}}{h} \Re(S_1 - S_2 - S_3) \tag{19}$$

Here,

$$S_1 = \frac{i}{2\pi} \frac{\psi(\frac{\pi + d + ic}{2\pi}) - \psi(\frac{\pi + b + ia}{2\pi})}{c - a + i(b - d)} \tag{20}$$

$$S_2 = \frac{1}{4\pi^2}\frac{1}{[c-a+i(b-d)]^2}$$
$$\{[d^2-c^2+(\widetilde{\varepsilon_1}+a+i(2d-b))c-(b+i(\widetilde{\varepsilon_1}+a))d-(a-ib)\widetilde{\varepsilon_1}]\psi^{(1)}(\tfrac{\pi+d+ic}{2\pi}) \quad (21)$$
$$-2\pi(b+i(a-\widetilde{\varepsilon_1}))[\psi(\tfrac{\pi+d+ic}{2\pi})-\psi(\tfrac{\pi+b+ia}{2\pi})]\}$$

and $S_3 = S_2(d \to b; c \to a; a \to c; b \to d)$, and $\psi(z)$ is the digamma function. In Fig.1, we plot the temperature dependence of the scaled conductance for the one-level and for the two-levels quantum dot.

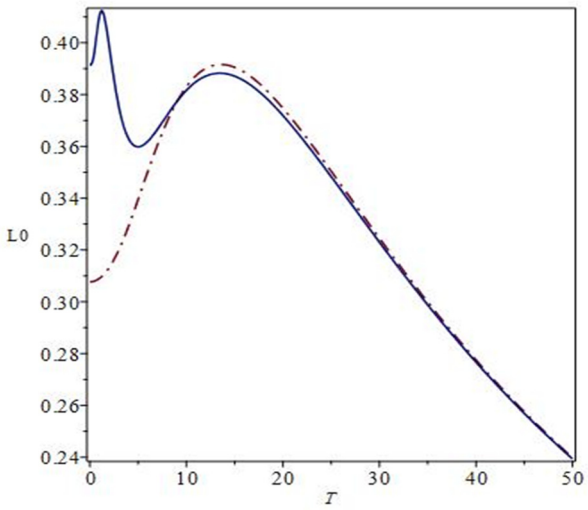

Fig. 1. Scaled conductance as function of temperature. The line correspond to the two-levels quantum dot, and the dashed-dotted line correspond to the one-level quantum dot, for the following parameters: $\widetilde{\gamma_0} = 20\,K/T$, $\widetilde{\varepsilon_0} = 30\,K/T$, $\widetilde{\varepsilon_1} = 5\,K/T$, $\widetilde{t_c} = 5\,K/T$, and for $h = 1$.

In the case when $t_c = 0$ the result (19) reduces to the previous result given by eq. (12).

A. SOMMERFELD EXPANSION

In this section, we will give approximate results of the conductance valid in the low temperatures region. For the one-level quantum dot we will approximate the trigamma function (for large z), according to the relation:

$$\psi^{(1)}\left(\frac{1}{2}+z\right)=\frac{1}{z}-\frac{1}{12z^3}\ldots \tag{22}$$

Using (22) with $z=(\gamma_0+i\varepsilon_0)/2\,\pi k_B T$, L_0given by eq.(12) will be

$$L_0 \simeq \frac{1}{h}\frac{\gamma_0^2}{\gamma_0^2+\varepsilon_0^2}\left[1-\frac{(\pi k_B T)^2}{3}\frac{\gamma_0^2-3\varepsilon_0^2}{(\gamma_0^2+\varepsilon_0^2)^2}\right] \tag{23}$$

In a similar way, for the two-levels quantum dot, the Sommerfeld expansion is:

$$L_0=\frac{1}{h}\frac{\gamma_0^2}{(\varepsilon_0-\frac{t_c^2}{\varepsilon_1})^2+\gamma_0^2}\left[1+\frac{(\pi k_B T)^2}{3}\cdot R\right] \tag{24}$$

with

$$R=\frac{4(\varepsilon_0-\frac{t_c^2}{\varepsilon_1})^2(1+\frac{t_c^2}{\varepsilon_1^2})^2}{[(\varepsilon_0-\frac{t_c^2}{\varepsilon_1})^2+\gamma_0^2]^2}-\frac{1+\frac{2t_c^2}{\varepsilon_1^2}+\frac{3t_c^4}{\varepsilon_1^4}-\frac{2t_c^2\varepsilon_0}{\varepsilon_1^3}}{(\varepsilon_0-\frac{t_c^2}{\varepsilon_1})^2+\gamma_0^2} \tag{25}.$$

Higher values of t_c(up to a limit of it) lead to increased values of the conductance (in the low temperatures limit), as one can see in Fig.2.

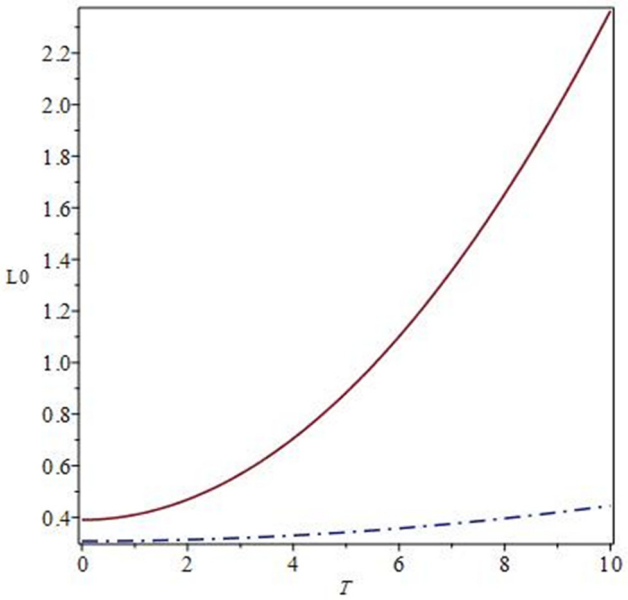

Fig. 2. Scaled conductance as function of temperature in the Sommerfeld approximation for the two-levels quantum dot. The line correspond to $t_c=5$, and the dashed-dotted line correspond to $t_c=0$**.** The parameters are: $\varepsilon_0=30, \gamma_0=20, \varepsilon_1=5$, and $h=k_B=1$.

B. HIGH-TEMPERATURES EXPANSION

Here we will analyse only the one-level quantum dot case. In the high temperatures limit the trigamma function (for small z) is approximated as

$$\psi^{(1)}\left(\frac{1}{2}+z\right)=\frac{\pi^2}{2}-14\zeta(3)z+\frac{\pi^4 z^2}{2}\ldots \tag{26}$$

Using eq.(12) the main contribution to the conductance, in this case, will be

$$L_0 \simeq \frac{\pi\gamma_0}{4hk_BT} \tag{27}$$

in agreement with the plot from Fig. 1.

III. CONCLUSIONS

We analytically calculate the electrical conductance of an one-level and double-level quantum dot. These obtained results are useful for the study of thermoelectric effects in mesoscopic structures. The differences in the temperature dependence of the conductance for one-level and for two-levels quantum dot are highlighted. The difference are substantial at low temperatures, while at high temperatures they are insignificant. At low temperatures, the tunneling effects between the levels in the dot (for the two-levels quantum dot) and the quantum interference effects leave a significant mark on the conductance. At high temperatures, the quantum effects are erased by the thermal effects, and the conductance is similar in both cases. We also obtained Sommerfeld expansion results for the quantum dot conductance. These results are valid in the low temperatures limit. As one see from Fig. 1 and Fig. 2, the results of the Sommerfeld approximation deviate significantly from the exact results, as the temperature increases and, for the parameters used, the results of the approximation are valid only at extremely low temperatures.

REFERENCES

[1]. F.J. Blatt, in "*Solid State Physics*", vol.4, p.199, F. Seitz, D. Turnbull eds., Academic Press, New York, (1957)

[2]. S. Datta, "*Electronic Transport in Mesoscopic Systems*", Cambridge Univ. Press, New York, (1958)

[3]. L.D. Hicks, M.S. Dresselhaus, *Phys. Rev. B* 47, 12727, (1993)

[4]. Y. Dubi, M. Di Ventra, *Rev. Mod. Phys.* 83, 131, (2011)
[5]. C.J. Lambert, *Chem. Soc. Rev.* 44, 875, (2015)
[6]. I. Grosu, L. Tugulan, *J. Supercond. Nov. Magn.* 21, 65, (2008)
[7]. D.K. Ferry, S.M. Goodnick, J. Bird, "*Transport in Nanostructures*", Cambridge Univ. Press, New York, (2009)
[8]. J.C. Cuevas, E. Scheer, "*Molecular Electronics",* World Scientific, New Jersey, (2010)
[9]. I.S. Gradshteyn, I.M. Ryzhik, *"Table of Integrals, Series and Products",* Academic Press, (2007)
[10]. L. Zhou, *arXiv:1704.04733v3*
[11]. G. Bevilaqua, G. Grosso, G. Menichetti, G. Pastori Parravicini, *Phys. Rev. B* 94, 245419, (2016)
[12]. M. Abramowitz, I.A. Stegun, "*Handbook of Mathematical Functions"*, Dover, New York, (1972).

STUDIA UBB PHYSICA, Vol. 67 (LXVII), 1-2, 2022, pp. 43-53
(RECOMMENDED CITATION)
doi:10.24193/subbphys.2022.05

STRUCTURE AND MORPHOLOGY OF ZnO FILMS CO-DOPED WITH AL AND RARE EARTH DEPOSITED BY SPRAY COATING TECHNIQUE

M. TOMA[1], D. MARCONI[1,2], C. LUNG[1*], M. POP[3], A. POP[1]

ABSTRACT. In this work, the influence of co-doping with Al and rare earth ions (RE= Er, Gd, Nd) on the structure and morphology of zinc oxide (ZnO) films is presented. Spray coated thin films were obtained using a mixture of nitrate substances diluted in equal quantities of distilled water and ethanol. The coated films were deposited on quartz glass and Si(100) substrates using a constant concentration of 0.15M, a temperature of 210ºC, pressure of 2 bar and 10 minutes time of deposition. After this step, the coated films were annealed at 3 different temperatures (600ºC, 800ºC and 1000ºC) for 5 minutes each. The influence of dopant and annealing treatment upon crystallographic structure of the films was analyzed by X-ray diffraction (XRD). Microstructural and surface analysis from scanning electron microscopy (SEM) and AFM measurements evidenced that the type of doping and the annealing treatment modify the surface morphology of the films.

Keywords*: spray coating technique, AZO-RE thin films, XRD, SEM, AFM.*

INTRODUCTION

Metal-oxide thin-film transistors (TFTs) have shown increasing utilization in a wide range of applications. Zinc oxide (ZnO) is one of the most interesting transparent and conducting oxide (TCO) due to its electro-optical properties, large band gap, abundance in nature and high electrochemical stability. It has an n-type

[1] *Babes-Bolyai University, Physics Faculty, M. Kogalniceanu No. 1, 400084, Cluj-Napoca, Romania*
[2] *Department of Molecular and Biomolecular Physics, National Institute for Research and Development of Isotopic and Molecular Technologies, Cluj-Napoca, Romania*
[3] *Faculty of Material Engineering and Environment, Technical University of Cluj, 103- 105 Muncii Avenue, 400641 Cluj-Napoca, Romania*
[*] *Corresponding author: claudiu.lung@ubbcluj.ro*

electrical conductivity and it is transparent to visible light. These advantages are of considerable interest for practical applications such as, gas sensors [1,2], piezoelectric devices and many others. With a proper choice of dopant atoms, the luminescence properties of ZnO films can be changed. By introducing Al atoms as dopants, the defect environment is changed whether these atom substitutes the zinc atom or it occupies the interstitial site. Al doping is expected to change the optical and electrical properties of ZnO films. To improve morphological, structural, electrical and optical properties, we decided to use rare earth dopants. In accordance to literature these type of dopants can increase electrical conductivity and form more uniform structures in thin films. Furthermore, different techniques have been applied to obtain ZnO nanostructured thin films such as RF magnetron sputtering [3], chemical vapor deposition [4], pulse laser deposition [5], spray pyrolysis [6], sol-gel process [7], etc. Among these techniques, spray coating techniques is frequently used because of its inexpensive equipment, reproducibility and simplicity to deposit large area, excellent control of chemical uniformity and stoichiometry and possibility of microprocessor based spraying. In a spray pyrolysis process, reaction temperature is a basic operating variable. In addition, solution properties such as precursor composition, concentration, or the addition of a co-solvent may be crucial to achieve the desired product composition and morphology [8,9]. Spray coating has been developed as a powerful tool to synthesize various Al-doped ZnO thin films [10-13] and RE doped ZnO [14-18]. Considering the numerous studies done on aluminum and rare earth doped ZnO by spray coating technique, to our knowledge has not used this method for synthesis of ZnO films co-doped with (Al + RE).

In this research, we describe a spray coating method to obtain ZnO films co-doped with Al+RE (RE= Er, Gd, Nd) and to study the effect of processing parameters such as annealing temperature on the structure and morphology of samples.

RESULTS AND DISCUSSION

Figure 1 shows the XRD pattern of ZnO films co-doped with Al and RE = Er,Gd,Nd (further AZO doped with RE), deposited on quartz glass, and annealed at three different temperatures (600ºC, 800ºC, 1000ºC). The vertical lines in the image show the position of peaks for crystallographic planes with (hkl) for: ZnO –green lines, Al_2O_3-blue vertical lines, RE oxide Re_2O_3 – red vertical lines. All the marked diffraction peaks of ZnO in Fig. 1 can coincidently be indexed by the known hexagonal standard ZnO. The crystallographic phase of doped ZnO belongs to the wurtzite-type ZnO. Diffraction peaks correspond to (100), (002), (101), (102), (110), (103) and (112) planes of wurtzite ZnO, confirming that all the polycrystalline films are randomly oriented. For ZnO film codoped with Al and Er (AZO –Er doped film in fig. 1),

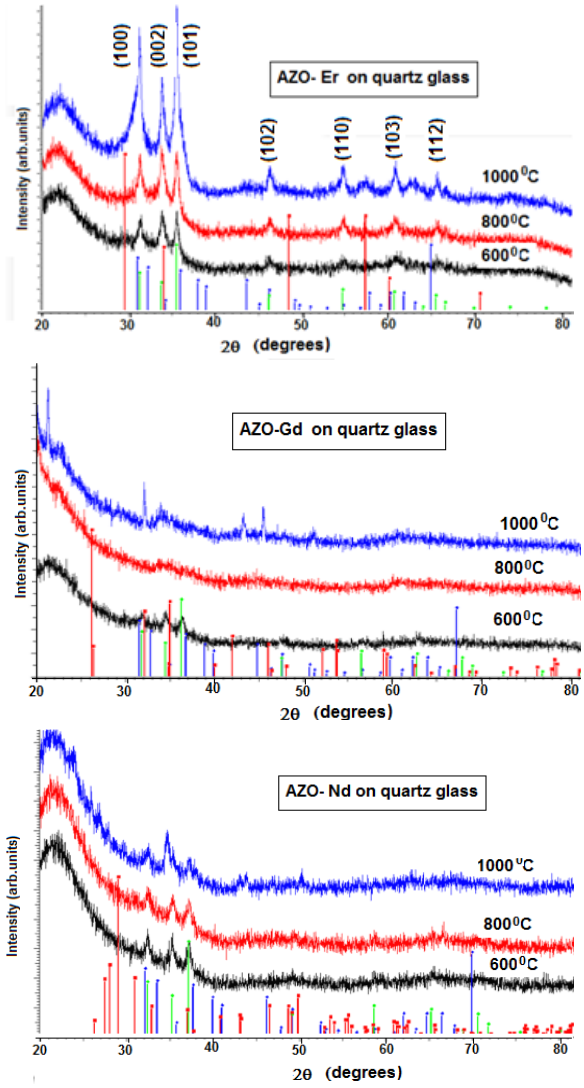

Fig. 1. XRD patterns for AZO film doped with Er,Gd,Nd, deposited on quartz glass substrates and annealed at 3 temperatures (600ºC, 800ºC ,1000ºC).

the relatively high intensity of the (101) peak is indicative of anisotropic growth and implies a preferred orientation. The peak intensities (100), (002) and (101) and the linewidth increased with increasing annealing temperature. The increase of linewidth suggests that the crystallinity of films is affected by the stresses because of the difference in ion radius size between zinc and the dopant (Al and Er) and the

segregation of dopants in grain boundaries. Furthermore, Gd-doped AZO thin films reveal a pronounced amorphous structure for the films deposited on quartz glass, XRD of the AZO-Nd doped film show an amorphous structure, but the presence of (100), (002) and (101) peak evidenced the presence of crystalline phase. For film obtained by using annealing temperature t=1000ºC, the intensity of (002) peak increases comparatively with the films obtained for t=600, 800ºC.

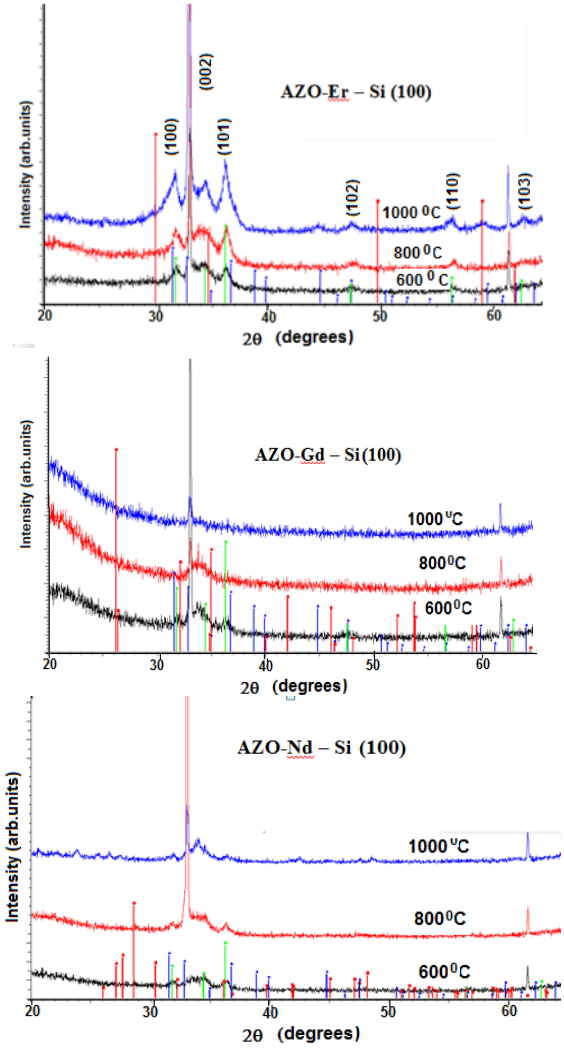

Fig. 2. XRD patterns for AZO-RE (RE=Er,Gd,Nd) thin films deposited on Si(100) substrates and annealed at three temperatures (600ºC, 800ºC, 1000ºC).

XRD results show significant differences between the films deposited on two types of substrates. Si(100) substrate and quartz glass substrate differently influenced the growth of films, and crystallographic plane orientation, respectively. Therefore, for films deposited on Si(100) substrate the intensity of (002) peak is higher and more evident than for thin films deposited on quartz glass substrates. The c-axis epitaxy is influenced by the type of RE ion and annealing temperature. For Er doped AZO film, the relatively high intensity of the (200) peak comparatively with (101) and (102), suggests the anisotropic growth with a preferred c-axis orientation. For Gd and Nd doped AZO films deposited on the Si(100) substrates the c-axis epitaxy is higher that for Er doped AZO film, and is influenced by substrate temperature. For Gd doped film, the higher intensity for (002) peak was obtained for the annealing temperature of 600ºC and for Nd-doped films for the annealing temperature of 800ºC, respectively. Nevertheless, the films show a good *c*-axis orientation, corresponding to vertical growth with respect to Si(100) substrate. This preferred orientation is due to the minimal surface energy of the (002) plane that corresponds to the dense packed plane of the ZnO hexagonal structure. The value of lattice constant, c is calculated from the XRD data and is given in *Table 1*. It is observed that the *c*-axis length is influenced by the type of RE dopant, but it does not change much with the increase of annealing temperature. It was observed that doping of AZO with RE ions lead to the *c*-axis length decreases. Responsible for the decrease in the *c*-axis length was the induced cationic vacancies created by Nd^{3+} doping in the ZnO host matrix [15]. Similar *c*-axis variations were also reported in Er doped ZnO [19] and Ce doped ZnO [20]. The influence of annealing temperature on the stress along the c-axis direction for codoped ZnO films deposited on Si(100) substrate was investigated. By using the biaxial strain model, for the hexagonal lattice of ZnO, the stress (σ) in the film can be calculated with the following formula:

$$\sigma = \frac{2c_{13}^2 - c_{33}(c_{11}+c_{12})}{2c_{13}} \times \varepsilon \quad (1)$$

where ε (c_{film}-c_{bulk})/c_{bulk}, c_{bulk} =5.200 Å is the unstrained lattice parameter (American Society for Testing and Materials) and c_{film} is measured by XRD.

By using the elastic constants c_{ij} of single-crystalline ZnO from reference [21], we obtain $\sigma_{film} = -233 \times \varepsilon$ (GPa). This compressive stress takes place during deposition process itself.

Table 1 shows that, the calculated stress in the direction of the c-axis for Er and Gd doped films, decreases with increasing annealing temperature. The positive sign of the stress is the indication of tension stress. For Nd doped films, by increasing annealing temperature, the sign of stress changes from negative to positive values,

suggesting a change from tension stress to compressive stress. The RE-ions tend to create additional stress in the lattice structure of films and along c-axis because Er^{3+}(0.89 Å), Gd^{3+}(0.935 Å) and Nd^{3+}(0.98 Å) have larger ion radius than that of Zn^{2+} ion (0.74 Å), which makes the replacement more difficult, thus distorting the ZnO lattice [22,23].

Table 1. Calculated stress and strain in the film lattice

Sample name	Annealing temperature (°C)	Lattice parameter, c (nm)	ε (%)	σ (GPa)
AZO-Er	600	5.184	-0.31	0.72
	800	5.191	-0.17	0.40
	1000	5.196	-0.08	0.18
AZO-Gd	600	5.161	-0.75	1.74
	800	5.165	-0.67	1.56
	1000	5.169	-0.59	1.39
AZO-Nd	600	5.196	-0.08	0.18
	800	5.204	0.08	-0.18
	100	5.208	0.15	-0.36

SEM images emphasize the strong influence of the type of dopant and the annealing temperature upon the structure of spray coated films. Therefore, with increasing the annealing temperature, larger cracks begin to form as shown in figures below. Even if the cracks/valleys are not very deep into the surface structure, the film is not uniform anymore, making it impossible for electrical measurements.

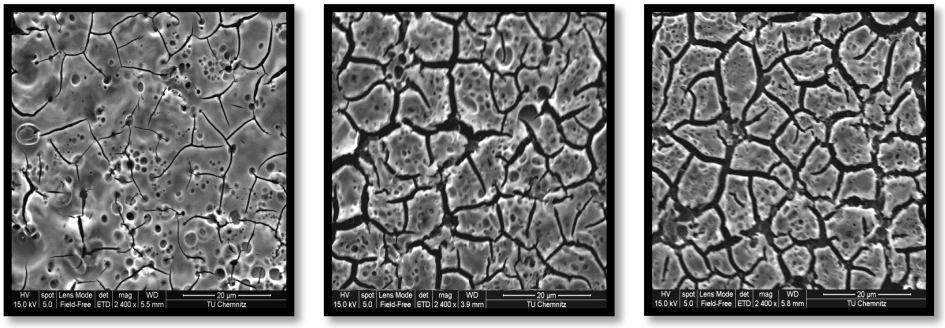

Fig. 3. AZO-Er spray coated on Si(100) and annealed at temperatures: 600ºC, 800ºC, 1000ºC (left to right).

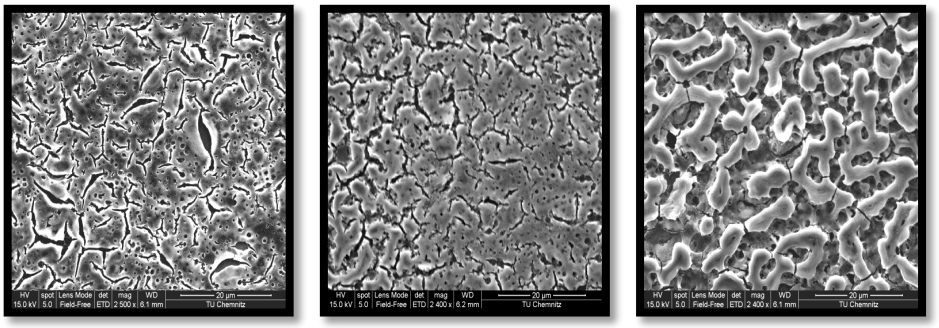

Fig. 4. AZO-Gd spray coated on Si(100) and annealed at temperatures:
600ºC, 800ºC, 1000ºC (left to right).

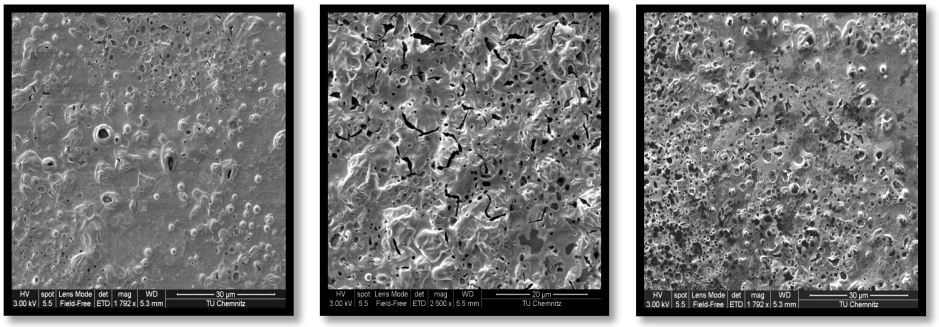

Fig. 5. AZO-Nd spray coated on Si(100) and annealed at temperatures:
600ºC, 800ºC, 1000ºC (left to right).

SEM for the the Si(100) spray coated samples provide some interesting information regarding the surface. Hence, these results accentuate the difference in sample structure with increasing the annealing temperature, resulting in the appearance of larger cracks and more defined crystallites, which could prove the intensity of the peaks from XRD.

AFM images complete the surface analysis which are in accordance with the SEM results.

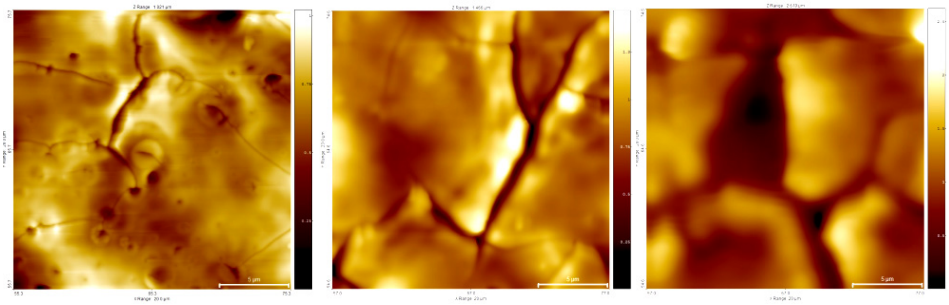

Fig. 6. AZO-Er spray coated on Si(100) and annealed at temperatures: 600ºC, 800ºC, 1000ºC (left to right).

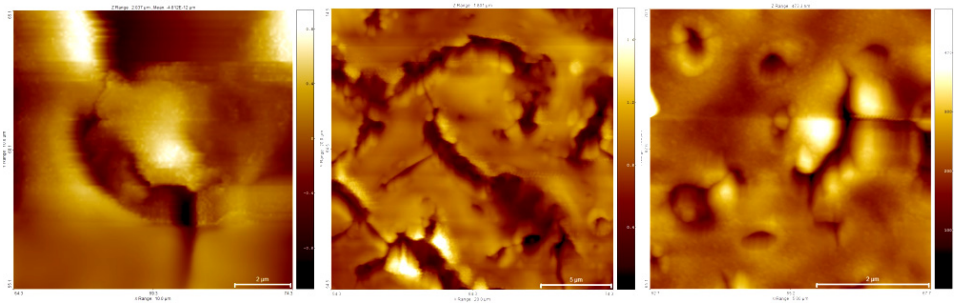

Fig. 7. AZO-Gd spray coated on Si(100) and annealed at temperatures: 600ºC, 800ºC, 1000ºC (left to right).

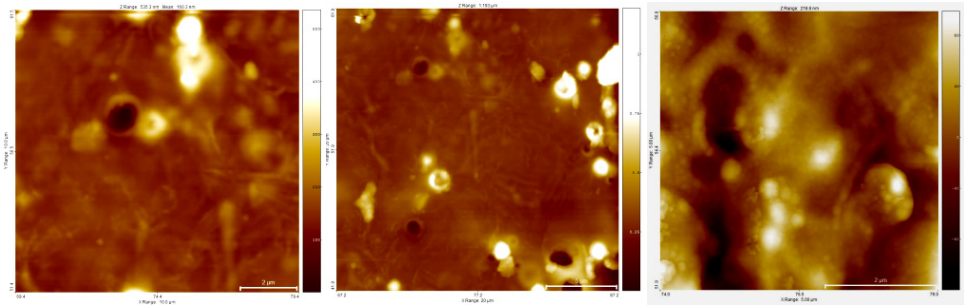

Fig. 8. AZO-Nd spray coated on Si(100) and annealed at temperatures: 600ºC, 800ºC, 1000ºC (left to right).

Furthermore, by using different RE dopants we could observe a slight effect in how compact the surface was formed, revealing better quality for the samples doped with Nd ions, that could be related to the fact that Nd has a smaller ionic radius compared to the other RE used, making it more likely to incorporate into the ZnO lattice.

CONCLUSIONS

ZnO thin films co-doped with Al and RE ions were grown using spray coating technique and deposited on quartz glass and Si(100) single crystal. The films were annealed at three different temperatures (600ºC, 800ºC, 1000ºC), and characterized by XRD, SEM and AFM.

The type of RE-ions, substrate and annealing temperatures, induce changes in the structure and especially in the morphology of thin films.
The growth of film and crystallographic plane orientation is differently influenced by Si(100) substrate and quartz glass substrate respectively.

All films deposited on quartz glass are polycrystalline with random orientation. For films deposited on Si(100) substrate, anisotropic growth with a preferred c-axis orientation was emphasized. The degree of c-axis epitaxy and the stress along this direction is influenced by the type of RE ion and annealing temperature. Along the c-axis, for Er and Gd dopants the tension stress decreases with increasing annealing temperature, while for Nd dopant the change from tension stress to compressive stress was evidenced.

AFM and SEM revealed that the sprayed samples forms cracks on the surface and the number of crystallites increases with increasing the annealing temperature. Also, the type dopant used had a slight effect in how compact the surface was formed after the annealing process, revealing better quality for the samples doped with Nd ions.

EXPERIMENTAL SECTION

Spray coated technique and two different types of substrates were used to obtain ZnO co-doped with Al and RE ions using a constant concentration of 0.15 M. Solid nitrides were measured after the specific concentration (c=0.15 M) and quantities were calculated, then mixed with equal quantities of ethanol and distilled water using the ultrasonic bath for 5 minutes for better homogeneity. Two types of substrates were used, quartz glass and Si(100) kept at a temperature of 210°C and a pressure of 2 bars, for 10 minutes time of deposition. After the spraying process, the samples were annealed at three different temperatures (600°C, 800°C, 1000°C) for 5 minutes each to eliminate any impurities and mechanical stress in the films. The structure of films was determined by XRD analysis, using a Brucker D8 X-ray diffractometer with a CuK_{α} radiation. The 2θ range was recorded at the rate of 0.02º and 2θ / 0.5 s. The crystal phases were identified by comparing the 2θ values and

intensities of reflections on X-ray diffractograms with JCP data base using Diffraction AT-Brucker program. Scanning electron microscopy technique was used to illustrate the morphology of film surface. SEM images were recorded using FEI Quanta 3D FEG 200/600 microscope.

The sample topography was analyzed by atomic force microscopy (AFM) in order to analyze the structure of the surface. AFM images were taken with a Ntegra Spectra commercial microscope (NT-MDT, Russia) at room temperature in semicontact mode with anticorrosive rectangular monocrystalline silicon Sb doped cantilever for static charge dissipation, electrical resistivity 0.01-0.025 Ω×cm, resonant frequency in the range 240-440 kHz (typically 320 kHz), a constant force of 22-100 N/m (typical 40 N/m), peak radius <10 nm (typical 6 nm). After acquisition, image processing was performed using the Nova v1.1.0.1837 (NT-MDT) program.

REFERENCES

[1] M.-W. Ahn, K.-S. Park, J. Heo, D.-W. Kim, K. J. Choi, J.-G. Park, *Sensors and Actuators B* 138 (2009)168-173.
[2] Kuwei Liu, Makoto Sakurai, Masakazu Aono, *Sensors and Actuators B* 157 (2011) 98-102.
[3] Yu-Ming Lin, Chien-Hsun Chu, Hung-Wei Wu, Jow-Lay Huang, IMECS (2015).
[4] V. Ghafouri, M. Shariati, A. Ebrahimzad, *Sci. Iran. Trans.* F, 19 (3), (2012), pp. 934–942.
[5] Patwari G., Bodo B.J., Singha R and Kalita P.K."Photoluminescence Studies of H2O2 Treated Chemically Sythesized ZnO Nanostructures", *Res. J. Chem. Sci.,* Vol.3 (9), (2013), pp.45-50.
[6] Kentaro Sakai, Kohei Noguchi, Atsuhiko Fukuyama, Tetsuo Ikari and Tatsuo Okada, "Low-Temperature Photolumine cence of Nanostructured ZnO Crystal Synthesized by Pulsed-Laser Ablation" *Jpn. J. Appl. Phys*, Vol. 48, (2009), 085001.
[7] Yaxin Cai, Xiaowei Li, Yang Liu, Sisi Du, Pengfei Cheng, Fengmin Liu, Kengo Shimanoe, Noboru Yamazoe and Geyu Lu, *CrystEngComm,* (2014), 16, 6135.
[8] A.C. Tickle, Thin Film Transistors, John Wiley and Sons, New York, USA, 1969.
[9] E. Bacaksiz, M. Parlak, M. Tomakin, A. O¨ zc¸elik, M. Karakız, M. Altunbas¸ *J. Alloys Compd.* 466 (2008) 447–450.
[10] L. Dghoughi, F. Ouachtari, M. Addou, B. Elidrissi, H. Erguig, A. Rmili, A. Bouaoud, *Physica B* 405 (2010) 2277–2282.
[11] C.M. Muiva, T.S. Sathiaraj, K. Maabong, *Ceramics International* 37 (2011) 555–560.
[12] Kuang-Che Hsiao, Shih-Chieh Liao, Yi-Jia Chenb, *Materials Science and Engineering A* 447 (2007) 71–76.
[13] S.M. Rozati, Sh. Akesteh, *Materials Characterization* 58 (2007) 319–322.

[14] M. Alaoui Lamrani, M. Addou, Z. Sofiani, B. Sahraoui, J. Ebothe, A. El Hichou, N. Fellahi, J.C. Bernede, R. Dounia, *Optics Communications* 277 (2007) 196–201.
[15] M Subramanian, P Thakur, S Gautam, K H Chae, M Tanemura, T Hihara, S Vijayalakshmi, T Soga, S S Kim, K Asokan and R Jayavel, *J. Phys. D: Appl. Phys.* 42 (2009) 105410 (6pp).
[16] A. Douayar, P. Prieto, G. Schmerber, K. Nouneh, R. Diaz, I. Chaki, S. Colis, A. El Fakir, N. Hassanain, A. Belayachi, Z. Sekkat, A. Slaoui, A. Dinia, and M. Abd-Lefdil, *Eur. Phys. J. Appl. Phys.* (2013) 61: 10304 (p1-p6) DOI: 10.1051/epjap/2013120388.
[17] M. Subramanian, P. Thakur, M. Tanemura, T. Hihara, V. Ganesan, T. Soga, K. H. Chae, R. Jayavel, and T. Jimbo, *Journal of Applied Physics* 108, (2010), 053904, p1-p7.
[18] R.A. Mereu, A. Mesaros, M. Vasilescu, M. Popa, M.S. Gabor, L. Ciontea, and T. Petrisor, *Ceramics International* 39 (2013) 5535–5543.
[19] Perez-Casero R, Gutierrez-Llorente A, Pons-Y-Moll O, Seiler W, Defourneau R M, Defourneau D, Millon E, Perriere J, Goldner P and Viana B 2005 *J. Appl. Phys.* 97 054905.
[20] Sofiani Z, Derkowska B, Dalasinski P, Wojdyła M, Dabos-Seignon S, Alaoui Lamrani M, Dghoughi L, Bała W, Addou M and Sahraoui B 2006 *Opt. Commun.* 267 433.
[21] Cebulla R, Wendt R, Ellmer K, *J. Appl. Phys*. 83 (1998) *1087*-1095.
[22] C. Bingqiang, C. Weiping, *Journal of Physical Chemistry C* 112 (2008) 680–685.
[23] Z. Jun, S. Lingdong, Y. Jialu, S. Huilan, L. Chunsheng, Y. Chunhua, *Chemistry of Materials* 14 (2002) 4172–4177.

STUDIA UBB PHYSICA, Vol. 67 (LXVII), 1-2, 2022, pp. 55-77
(RECOMMENDED CITATION)
doi:10.24193/subbphys.2022.06

SUSPENSION BASED ON A MIXTURE OF TITANIA-SILICA-FUNCTIONALIZED GRAPHENE OXIDE FOR SURFACE CONSOLIDATION OF HISTORICAL ANDESITE STONE AND MORTAR

L.C. COTET[1,2*], C. SALAGEAN[2,3], A. MIHIS[2], I. SZÉKELY[3,4], ZS. TOTH[4], L. BAIA[2,3,4], M. BAIA[2,3], G. OLTEANU[5], I. OLTEANU[5], V. DANCIU[1]

ABSTRACT. Three-components suspension, based on a mixture of titania (TiO_2)-silica (SiO_2)-functionalized graphene oxide (GO) is prepared and used for surface consolidation of historical andesite stone and mortar. For comparison, mono- and bi-component suspensions are also involved in this study. In order to increase the attachment capacity of GO to substrate with silicon, GO functionalized with (3-aminopropyl) triethoxysilane (GO-APTES) was involved. Unmodified and modified by painting with prepared suspensions andesite and mortar samples were investigated by microscopy (Optic and SEM-EDX), XRD, FT-IR and Raman spectra before and after 6 months of exposure to ambient conditions. After investigation, even the amount of used consolidant suspension was low, the stability of the modified samples was found that remains constant and in a long time it is possibly to reach even a higher stability level. This approach provides the idea that the prepared suspension could be an interesting option to be involved in stone and mortar consolidation-restoration field.

Keywords*: titanium oxide, cultural heritage, functionalized graphene oxide, surface consolidation, historical stones, historical mortars.*

[1] *Department of Chemical Engineering, Faculty of Chemistry and Chemical Engineering, Babes-Bolyai University, Arany Janos 11, RO-400028, Cluj-Napoca, Romania*
[2] *Institute of Research-Development-Innovation in Applied Natural Sciences, Babes-Bolyai University, Fantanele 30, RO-400294, Cluj-Napoca, Romania*
[3] *Faculty of Physics, Babes-Bolyai University, M. Kogalniceanu 1, RO-400084, Cluj-Napoca, Romania*
[4] *Nanostructured Materials and Bio-Nano-Interfaces Center, Interdisciplinary Research Institute on Bio-Nano-Sciences, Babeș-Bolyai University, Treboniu Laurian 42, RO-400271 Cluj-Napoca, Romania*
[5] *S.C. Duct S.R.L., Feroviarilor 55, Sector 1, RO- 012206, Bucuresti, Romania*
[*] *Corresponding author: cosmin.cotet@ubbcluj.ro*

1. INTRODUCTION

Nowadays, there is a growing concern about the degradation of cultural heritage, which is an incalculable legacy for our future. In order to preserve the stone heritage, the intrinsic properties of the stone, the state of conservation, the degradation mechanisms and the environmental factors as well as the appropriate selection of materials and their application procedures must be taken into account. The compatibility, depth of penetration and durability of the selected materials, as well as their effect on water and vapor permeability, and their resistance to biological factors should also be taken into consideration. Until recently, the preservation of cultural heritage was mainly based on traditional conservation and restoration treatments such as the use of synthetic polymers, which often lack vital compatibility with substrate and durability. The development of materials science led to the discovery of nanomaterials with applicability in construction that allowed the improvement of the consolidation and protection of damaged building materials and the maintenance of the architectural heritage [1–3]. Consolidation treatment is an important conservation process that allows to improve the deep cohesion of the damaged stone heritage. However, the irreversibility of the consolidation process and its likelihood of causing unwanted effects makes this treatment one of the riskiest preservation processes. This risk explains the growing development and application of nanotechnology to the preservation of cultural heritage. Nanotechnology allows the design and development of reinforcing nanomaterials compatible with the original stone substrate, with 1-100nm in size and large surfaces, which leads to increased chemical reactivity and easier penetration into the depth of damaged stone monuments [4]. The dramatic increase in the external degradation of historical monuments due to air pollution, respectively the deposition of organic compounds and other pollutants on stone substrates has led to the development of nanomaterials with self-cleaning, antimicrobial and air depollution properties. Over the last 20 years, due to its outstanding ability to decompose pollutants by photocatalytic oxidation and its photoinduced superhydrophilicity [5], titanium dioxide is one of the best-known additives used in building materials, such as cement paste and mortar [6-8]. In addition, it should be noted that titanium dioxide is a cheap, non-toxic, chemically stable photocatalyst [9] and compatible with commonly used building materials [7]. The photocatalytic function of TiO_2 depends on its semiconductor and optical properties. Due to the oxygen vacancies present in its network, TiO_2 is an n-type semiconductor. The photocatalytic action of TiO_2 lies in the ability to simultaneously adsorb two reactants, which are reduced and oxidized

by photonic activation initiated by photon absorption ($h\nu \geq Eg$). The photoinduced electron transfer to an adsorbed molecule is determined by the position of the valence band and respectively the conduction band of the TiO_2 in relation to the redox potentials of the adsorbed molecules [10]. The energy value of the gap band of TiO_2-anatase is 3.2 eV, which means that it can only absorb UV light ($\lambda \leq 387$ nm). Given the fact that the solar spectrum consists of 3-4% ultraviolets, there was the problem of changing the electronic structure of TiO_2 so that it absorbs light from the visible region, and thus working efficiently under natural sunlight. This can be done either by TiO_2-doping with metals and non-metals, TiO_2 coupling with other semiconductors, or by creating network defects [8, 11, 12].

The great discrepancy between the recombination time of the photogenerated electron– hole pairs (10^{-9}s), and the time scale for the chemical interactions of TiO_2 with the adsorbed dirt (10^{-8} to 10^{-3}s) does that the unintended recombination of electron–hole pairs to be much more favourable than for the TiO_2–dirt adsorption which leads to a decrease in the efficiency of the photocatalytic activity of TiO_2 [13].

Due to its special features (specific surface area of 2600 $m^2 g^{-1}$, thermal/chemical stability and mobility of the charge carriers of 200,000 $cm^2 V^{-1} s^{-1}$) the graphene increases the adsorption capacity of TiO_2 based photocatalysts acting at the same time as an acceptor of the photo generated electrons from TiO_2, suppressing the recombination between photo-excited electrons and holes. Also, graphene act as a sensitizer extending light absorption range. The localized electrons in the sp^2 states of the graphene, excited by sunlight, are injected into the conduction band of TiO_2, where they are trapped by the O_2 molecules producing superoxides radicals which oxidize organic compounds [14,15]. The results of the researchers showed that the addition of graphene oxide improves the antibacterial and self-cleaning of the titanium dioxide films in order to use it in practical applications [14, 16, 17].

Another role of TiO_2-based nanoparticles is to improve mechanical properties (compressive strength, toughness, etc.), and to reduce the shrinkage and permeability of building materials - characteristics that prolong the life of the building material [18]. The positive influence on the impermeability of construction materials (mortar, concrete, etc.) can be explained either by the function of nanoparticles as fillers thus creating less permeable structures, or by their function as "nucleus" that induce the formation and growth of hydration of the cement or which promotes the formation of high-density C-S-H structures [19].

For the TiO_2 photocatalyst application in conservation and restauration of the cultural heritage, the issue was to ensure the durability and adhesion of TiO_2 on the stone or mortar substrates. In recent years, numerous studies have demonstrated the ability of silica-based materials to create durable and well-adherent TiO_2 coatings [20–23].

The TiO_2-SiO_2 coatings proved also high photocatalytic activity, the efficiency increasing as TiO_2 concentration was increased. The positive effects of SiO_2 are due to the increased surface area for adsorption and photodegradation of organic pollutants, to the charge imbalance which determines the creation of Lewis acidic sites, which promotes the adsorption of higher amount of hydroxide respectively a higher photocatalytic efficiency. Furthermore, TiO_2/SiO_2 composite having lower isoelectric point determines the increasing of the concentration of hydroxyl ions which are absorbed on the surface of photocatalysts and reduce the electron/hole recombination rate by blocking the generated holes [24–26].

In our previous study, interesting properties related to the increase of mechanical properties of mortar treated with consolidant based on graphene oxide (i.e. GO, oxidated form of graphene) was obtained [27]. More exactly, an increased value for the compressive strength of about twice time compared to the untreated blank samples and a decrease of the value for the capillary absorption water coefficient with about one order of magnitude in comparison with the untreated blank samples were obtained for mortar samples treated with GO consolidation suspension.

2. EXPERIMENTAL

2.1. Preparation of andesite and mortar as parallelepiped samples

In the case of andesite, a block of andesite was brought from the Pietroasa Bejan quarry and cut at a workshop in Bucharest into 1 cm thick slices, from which 2 cm wide strips were later extracted. The 2x1 cm^2 strips, obtained at coarse cutting, were cut into 2x2x1 cm^3 samples (Figure 1a). The samples thus obtained were sorted by removing the parts with errors, washed in distilled water and stored under normal conditions of temperature and humidity; 20-25 ^oC and 55-60% relative humidity. Thus, 100 parallelepipedal specimens of 2x2x1 cm^3 of andesite were obtained.

The lime mortar is prepared by recipe: one part slaked lime (paste), three parts washed and dried river sand sieved less than 2 mm.

For paste preparation, to 100 g of $Ca(OH)_2$ 100 ml of water was added to obtain a more fluid mixture that is proper to prepare a mortar with increased porosity. The obtained homogeneous mixture was introduced into the casting patterns by manual pressing. After drying and drawing out from the pattern, 100 samples of lime mortar measuring 2x2x1 cm^3 were obtained (Figure 1b). Alteration of the exposure surfaces was performed by treatment with acetic acid solution (6%) in all mortar samples (100 pcs.), by total immersion in the acid solution, exposure for 3 minutes, followed by stopping the reaction by immersing the sample in water.

The not modified faces of mortar samples were reinforced by using an acrylic paint in order to make the samples more enforced during manipulation. The binder has a holocrystalline structure being composed of micron calcite crystals, resulted from the carbonation of calcium hydroxide.

2.2. Preparation of graphene oxide components (i.e. GO and GO-APTES)

2.2.1. Preparation of GO

Graphene oxide (GO) was synthetized using an efficient sono-chemical exfoliation of graphite [28]. In the obtaining pathway besides graphite (7.5g, 99%, powder >0.1mm, Fluka), H_2SO_4 (742mL, 95–97%, SC Nordic Invest SRL, Cluj-Napoca), H_3PO_4 (83mL, 85%, SC Nordic Invest SRL, Cluj-Napoca) and KMnO4 (33g, 995, Sigma Aldrich) that are the main precursors of Marcano-Tour's improved exfoliation method [29], H_2O_2 (550mL, 3%, SC "Hipocrate 2000" SRL, Bucharest), H_2O (550mL, bidistilled homemade), HCl (275mL, 37%, SC Nordic Invest SRL, Cluj-Napoca) and ethanol (275mL, absolute, SC Nordic Invest SRL Cluj-Napoca) were involved into a washing-sonication-centrifugation-decantation process. After 7days of drying, about 14,3g GO was obtained.

2.2.2. Synthesis of GO functionalized with (3-aminopropyl) triethoxysilane (APTES)

Ethanolic suspension of GO (17,5 mL, C=40 mg / ml GO), was placed in a 3-necked flask having a capacity of 750 ml. Then, 360 ml (3-aminopropyl) triethoxysilane (APTES) and 360 mg N, N'-dicyclohexylcarbodiimide (DCC) were added under magnetic stirring at 700 rpm. An ascending water-cooled refrigerant was attached to the flask, and the installation was placed in an oil bath heated at 70ºC for 24 hours. After the reaction time elapsed, the precipitate of GO functionalized with APTES was allowed to settle, the top layer (colourless) was decanted and the suspension (bottom layer) was centrifuged at 6000 rpm for 15 minutes. The resulted precipitate has been washed three times with 300 ml absolute ethanol. After the last washing and separation by centrifugation, the precipitate of GO functionalized with APTES was dried in an oven at 60°C for 12 hours, yielding 1.0 g of GO functionalized with APTES (GO-APTES).

2.3. Preparation of colloidal solution used in consolidation process

2.3.1. Synthesis of TiO_2 colloidal solution (S1)

To an Erlenmeyer flask (V=50 ml) containing 5 ml of isopropyl alcohol, 30 ml of titanium tetraisopropoxide (98%, MERCK, GE)-TIP were added, in drops and continuous stirring, The obtained solution was added, in drops and continuous stirring, to 175 ml of bidistilled water in a three-necked glass flask (V = 1000 ml).

After 2.5 ml of 65% HNO_3 ml (CHEMPUR, RO) have been added, the flask provided with an ascending refrigerant connected to a water source was immersed in an oil bath at 80ºC for 6h continuously magnetic stirring.

2.3.2. Synthesis of TiO_2 colloidal solution with 0.026% GO functionalized with APTES (GO-APTES), (S2)

After 15 minutes of magnetic stirring of the obtained TiO_2 colloidal solution (see 2.3.1), the suspension of GO-APTES (0.053g of GO functionalized with APTES in 5 ml of absolute ethylic alcohol, stirred with ultrasound for 30 min) was added and then the mixture was stirred continuously and kept at 80ºC for 8 hours.

2.3.3. Synthesis of TiO_2-SiO_2 (67:33%) colloidal solution (S3)

A mixture of 11.2 ml of tetraethyl orthosilicate (98%, MERCK, DE), 0.05 ml of 65% HNO_3 (CHEMPUR, PL), 1.8 ml of double-distilled water and 26 ml of absolute ethyl alcohol (CHIMREACTIV SRL, RO) was prepared and added, under continuous stirring, to the obtained colloidal solution of TiO_2 (see 2.3.1) that was previously cooled to room temperature. Stirring was continued for 6 hours.

2.3.4. Synthesis of TiO_2-SiO_2 (67:33%) colloidal solution with 0.023% GO functionalized with APTES (GO-APTES), (S4)

To prepare TiO_2-SiO_2 (67:33%) colloidal solution with 0.023% GO-APTES, 0.054 g of GO-APTES were weighed and added to 5 ml of absolute ethyl alcohol. After 20 min of ultrasonic stirring, the obtained GO-APTES suspension was added to the colloidal solution of TiO_2-SiO_2 (see 2.3.3). Ultrasonic stirring was continued for one hour.

2.4. Devices and techniques involved in morpho-structural characterization

2.4.1. Optical microscopy

The optical microscopy analysis was performed with "Motic BA310Pol" device. After a surface cleaning by air blowing, the surface samples were analyzed in adequate lateral illumination.

2.4.2. Scanning electron microscopy (SEM)

The SEM and EDX (electron diffraction X-ray) analysis were performed with a SEM - HITACHI TM4000plus combined with an EDX OXFORD INSTRUMENTS hardware and AZtecOne software.

2.4.3. X-ray diffraction (XRD)

Structural properties of the samples were carried out by using Rigaku MiniFlex II diffractometer with X-ray (Cu-Kα; λ = 0,15406 nm) radiation equipped with a graphite monochromator. Scan speed was: 1°·min^{-1} (2θ°) and the diffractograms were taken between 3º-80º (2θ°). Samples were scraped with a spatula and transferred into an XRD support.

2.4.4. Fourier Transform Infrared (FT-IR)

Absorption spectra of the investigated samples were recorded at room temperature by employing a Jasco 6000 (Jasco, Tokyo, Japan) spectrometer (in reflection configuration) in the 400–4000 cm^{-1} range, with a spectral resolution of 4 cm^{-1}. All samples were prepared previously in the form of KBr pellets.

2.4.5. Raman spectroscopy

Raman spectra measurements were recorded with the help of a multilaser confocal Renishaw inVia Reflex Raman spectrometer equipped with a RenCam CCD detector. The 785 nm (NIR) laser line was applied as an excitation source on the samples' surface. The Raman spectra were collected employing a 0.9NA objective of 100 × magnification. The following parameters were used for all spectra: integration time was 20 s, 1200 lines/mm grating, and 50% of the maximum laser intensity - laser power of 150 mW.

3. RESULTS AND DISCUSSION

The study is performed on andesite and lime mortar. The andesite corresponds to the cultural objective Sarmizegetusa Regia, the source of the andesite being the magmatic body from Pietroasa, Bejani Hill, the south-eastern extremity of Deva municipality of Romania. The mortar was prepared in using a mixture of sand, $Ca(OH)_2$ and H_2O. Parallelepipedal samples of 2x2x1 cm^3 were prepared by stone cutting for andesite (Figure 1a) and casting in proper patterns for mortars (Figure 1b). The both sample types were modified by painting with four suspensions (Figure 1c): TiO_2 colloidal solution (S1), TiO_2 colloidal solution with GO-APTES (S2), TiO_2-SiO_2 (67:33%) colloidal solution (S3) and TiO_2-SiO_2 (67:33%) colloidal solution with GO-APTES (S4).

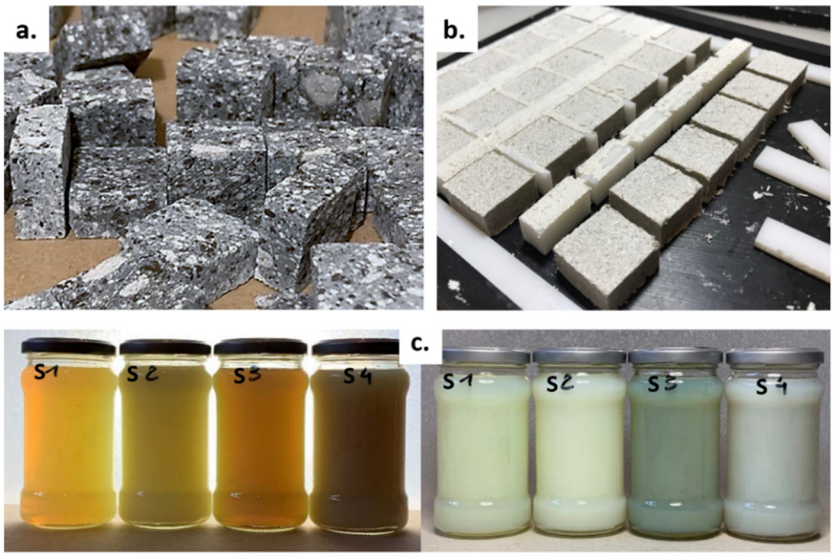

Fig. 1. Real images with andesite (a) and mortar (b) samples, and suspensions used in surface modification of the samples (c), (see Chapter 2.3).

In the present study, unmodified samples were also investigated as blanks (S0). Moreover, suspensions with GO (i.e. GO unfunctionalized with APTES) were not mentioned in this study because without GO's functionalization with silicious group a poor fixation of this nanosheet material on samples surface could be achieved. To increase of GO-APTES fixation, SiO_2 component could play a favorable behavior. In order to study the in time structural change, the investigation was performed on unexposed and 6 months ambient atmosphere exposed samples. The suspensions were applied only on a face of the parallelepipedal andesite and mortar samples that consist of 2x2 cm^2. After preparation and analysis, samples were placed in ambient atmosphere for 6 months (from May to October at the climate of Bucharest, Romania). Then, the samples were analyzed again.

3.1. Optical microscopy (OM) analysis of andesite and mortar surfaces

Investigation of andesite and mortar surfaces was performed with the optical microscope using reflected light illumination mode. In Figure 2 a compact structure with zones with different colours (e.g. light-grey, dark-grey) was evidenced for andesite samples. Instead of this, in Figure 3 a more granular structure (i.e. sand particles) linked with the binder component (i.e. calcium carbonate) was shown for mortar samples.

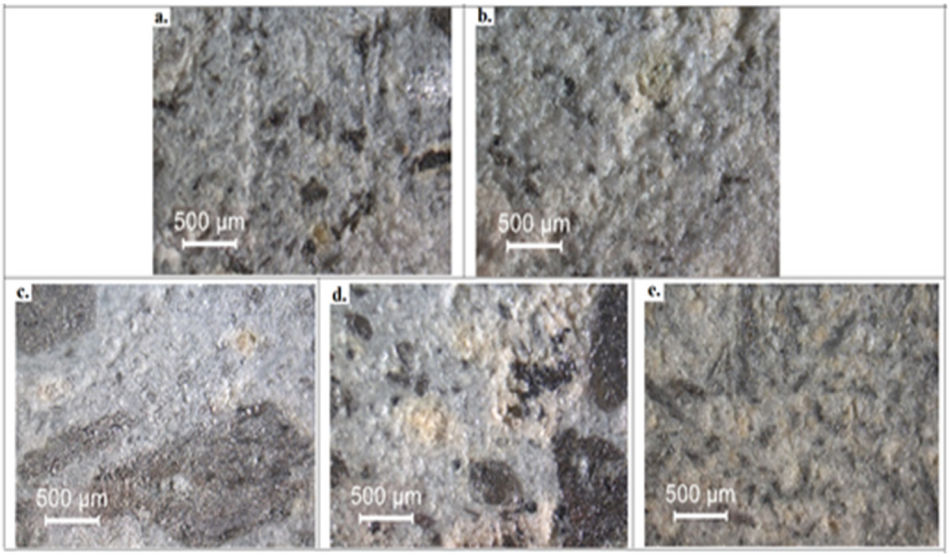

Fig. 2. Optical microscopy images with surfaces of andesite samples unmodified (a) and modified with S1 (b), S2 (c), S3 (d) and S4 (e) before of 6 months for external exposure.

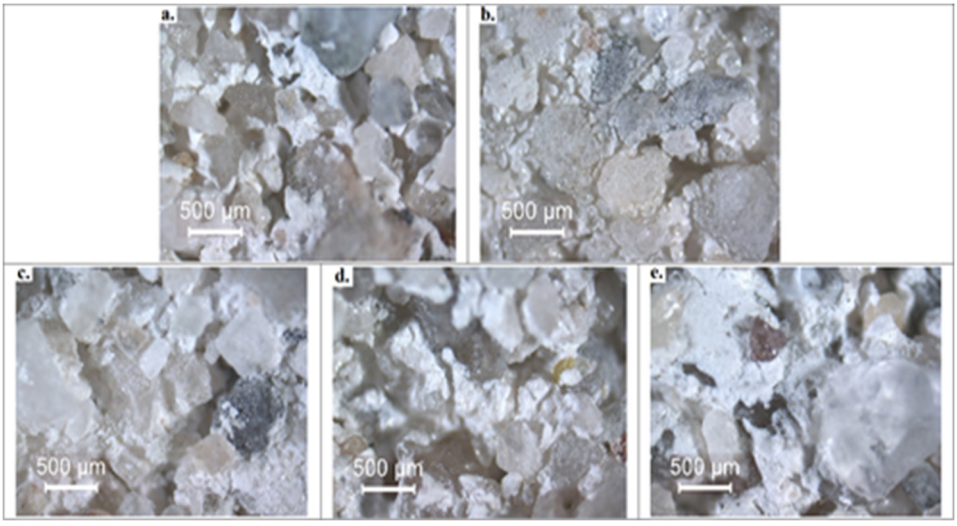

Fig. 3. Optical microscopy images with surface of mortar samples unmodified (a) and modified with S1 (b), S2 (c), S3 (d) and S4 (e) before of 6 months for external exposure.

For both sample types after surface modification with prepared suspensions (see Chapter 2.3), no visual change was evidenced. This could due to the low thickness and the transparent feature of applied layers. The same behavior was evidenced after 6 months of ambient environment exposure (i.e. for simplicity, these images are not presented).

In the case of mortar, microscopic observations show that the mass of the binder is relatively compact and has good adhesion to the aggregate clasps. It is also found that there are several shrinkage cracks in the binder mass, which are poorly connected, with local extension. A slight difference lies in the characteristics of the pore system. The pores have irregular shapes and variable sizes. The microscopically expressed porosity is about 10–15%.

Andesite rock porosity by microscopic examination shows that there are no over capillary pores in its structure. The rock is practically compact, with zero effective porosity and therefore waterproof.

3.2. SEM-EDX analysis of andesite and mortar surfaces

By SEM investigation surfaces with no regular features with zones with cracks were evidenced both for andesite (Figure 4) and mortar (Figure 5) samples and both before and after modification with prepared suspensions (see Chapter 2.3). The same behaviour was shown also after 6 months of ambient exposure (i.e. for simplicity, these images are not presented).

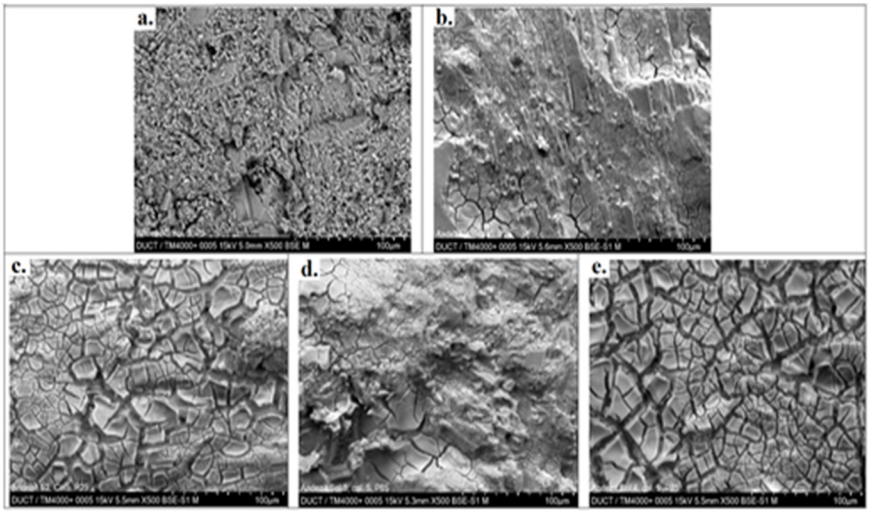

Fig. 4. SEM images with surfaces of andesite samples unmodified (a) and modified with S1 (b), S2 (c), S3 (d) and S4 (e) before of 6 months for external exposure.

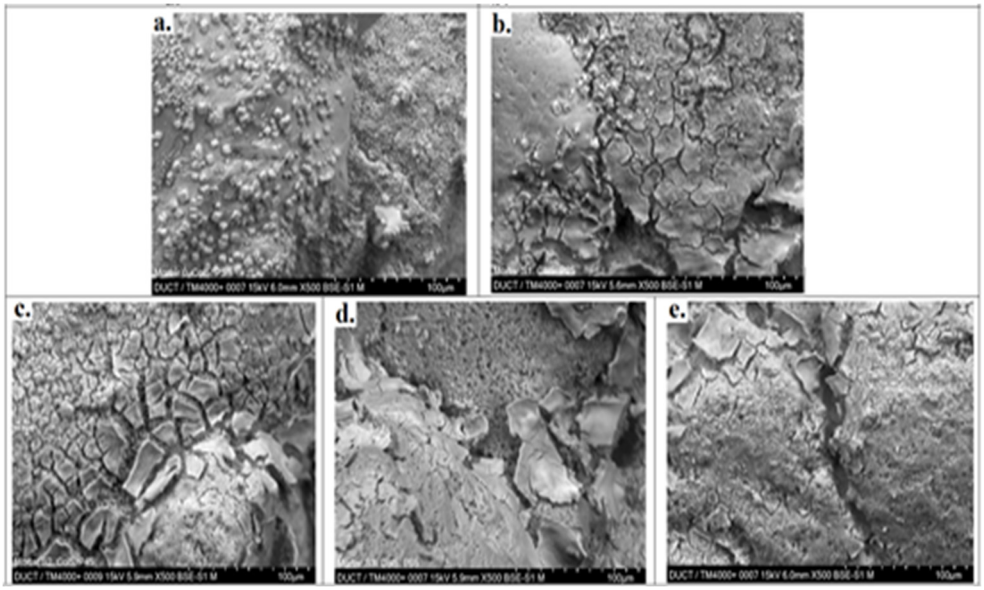

Fig. 5. SEM images with surface of mortar samples unmodified (a) and modified with S1 (b), S2 (c), S3 (d) and S4 (e) before of 6 months for external exposure.

The atomic ratios between the percent of Ti and Si (i.e. Ti/Si) were determined by EDX for S2 and S4 consolidant solutions dried on a common support (i.e. not applied on mortar or andesite samples) obtaining hundred micro meters of thickness (i.e. the analysis dose not touch the support). The values were 1.375 for S2 and 1.222 for S4, respectively. This means more Si in S4 in comparisons to S2 (i.e. because of Si from APTES). Moreover, the atomic percent for C (i.e. having GO-APTES as source) for S2 and S4 was not noticed by EDX. This could be because GO-APTES is in a very low concentration that means a low amount of C that is below the detection limit. The atomic percent ratio between Si of S3 and S4 which is 0.888, confirms again the presence of a higher amount of Si for solution prepared with GO-APTES (i.e. because of Si of SiO_2 component in addition to APTES).

3.3. X-ray diffraction (XRD) measurements on andesite and mortar surface

Commercial andesite consists mostly of SiO_2 and various types of Feldspar. In the andesite-unmodified and unexposed sample, we found amorphous SiO_2 and mineral Plagioclase with the following reflections: 21.7°, 23.4°, 24.3°, 27.4°, 30,2°, 35,3°, and 44,3° [30]. A new reflection is also visible in the andesite-unmodified and

exposed sample: 51.2° [30], which is a reflection of Plagioclase or Pyroxenes. Not all reflections of plagioclase could be observed in the XRD patterns of the unmodified samples because the sample is heterogeneous. The presence of TiO_2, SiO_2 and GO-APTES was not visible in the XRD patterns of the samples. The reason that the mentioned modification could not be seen in XRD patterns, could be that the amount of the TiO_2, SiO_2, and GO-APTES is lower than the detection limit of the XRD. The samples which have been exposed for 6 months are identical to the samples which were not exposed.

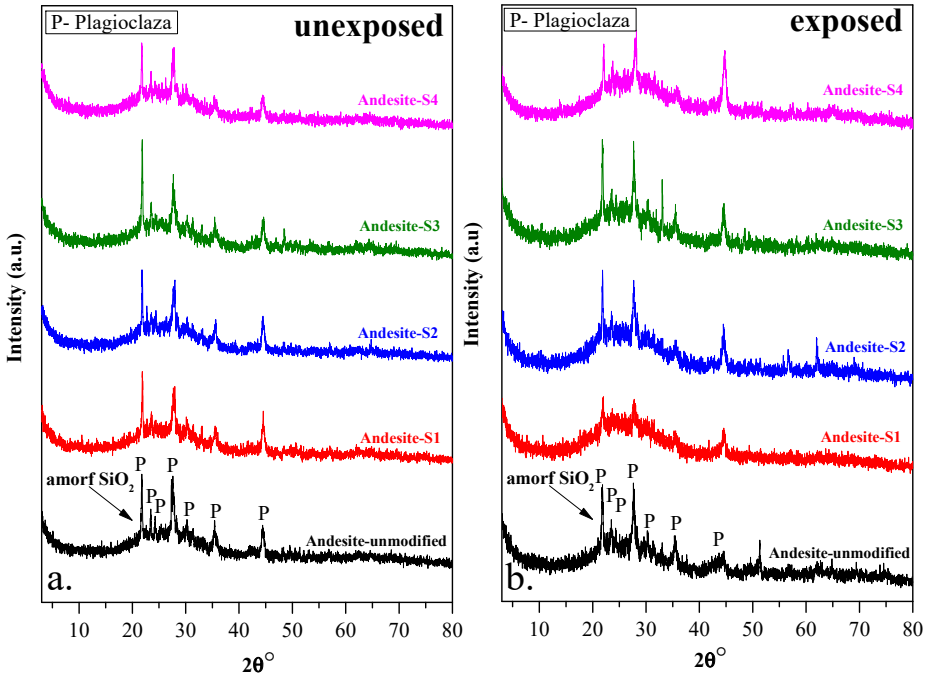

Fig. 6. XRD patterns of the unexposed and exposed (6 months) andesite samples.

3.4. Fourier Transform Infrared (FT-IR) measurements on andesite and mortar surface

Andesite is a volcanic rock with a mixed composition, meaning it is the intermediate rock between basalt and rhyolite. It predominantly comprises sodium-rich silicates such as plagioclase, pyroxene, and hornblende. In the FT-IR spectra of all unexposed and exposed andesite samples, the following bands were observed:

O-H stretching vibrations at 3439 cm^{-1}; H-O-H bending at 1636 cm^{-1} [31]; Si-O asymmetric and symmetric stretching vibrations at 1100, 1026, and 795 cm^{-1} [32, 33]; Si-O-Si bending a 619 cm^{-1}, respectively Si-O-Al bending at 538 and 483 cm^{-1} [34]. At first glance, the presence of TiO_2, SiO_2, and GO-APTES cannot be observed from the FT-IR spectra, but it was observed that the ratio of the I_{1026}/I_{1100} bands does change for both types of samples: unexposed and exposed (Table 1), which could hint at structural modifications of the samples. Moreover, from Table 1 it can be observed that the samples' I_{1026}/I_{1100} ratio changes in each sample when comparing it to the blank samples. In the case of the unexposed samples the ratio was below 1, but in the case of the exposed samples it was above 1, indicating that the samples' 6-month exposure did affect their structure.

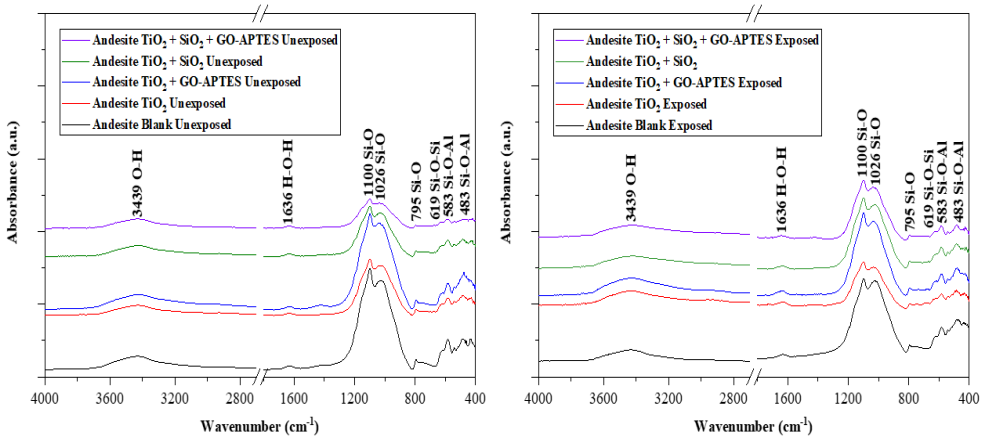

Fig. 7. FT-IR spectra of the unexposed and exposed (6 months) andesite samples.

Table 1. Ratio changes of the Si-O bands at 1026 and 1100 cm^{-1} in the unexposed and exposed samples

Sample	Unexposed	Exposed
	I_{1026} / I_{1100}	I_{1026} / I_{1100}
Andesite Blank	0.910	1.027
Andesite TiO_2	0.928	1.058
Andesite TiO_2 + GO-APTES	0.938	1.062
Andesite TiO_2 + SiO_2	0.920	1.042
Andesite TiO_2 + SiO_2 + GO-APTES	0.924	1.044

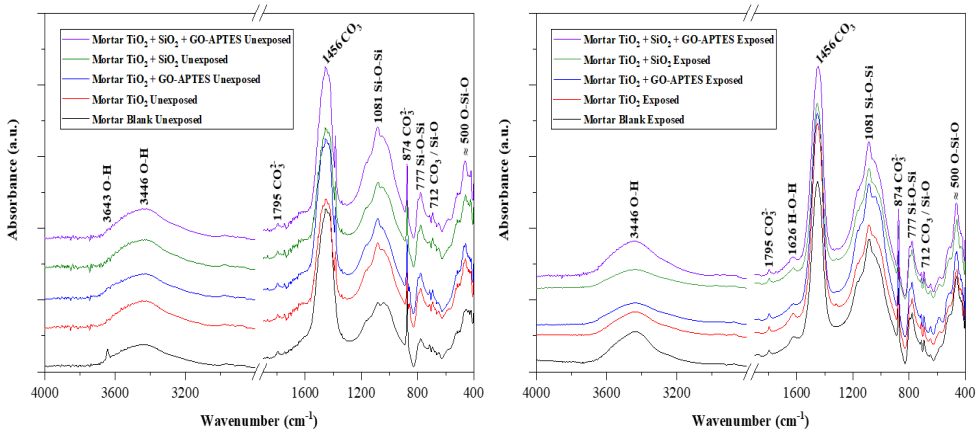

Fig. 8. FT-IR spectra of the unexposed and exposed (6 months) mortar samples.

The building blocks of mortar are lime and an aggregate of sand mixed with water. The mortar samples consist of lime, calcite, and quartz. Concerning the FT-IR spectra of the unexposed and exposed mortar samples, for each sample, the following absorption bands were identified: O-H stretching vibrations at 3643 and 3446 cm^{-1}, which were attributed to the $Ca(OH)_2$ from mortar [35]; CO_3^{2-} and CO_3 stretching at 1795, 1456, 874 and 712 cm^{-1}, which are related to the calcite and carbonate in the sample [36–38]; Si-O-Si asymmetric, Si-O symmetric stretching, and O-Si-O rocking vibrations at 1081, 777, 721 cm^{-1}, respectively in the 500 - 400 cm^{-1} region [39, 40].

Regarding the unexposed mortar samples, for all treated samples, a sharp band appeared at 1384 cm^{-1}, in the proximity of the CO_3 band; this can be linked to the presence of impurities on the sample's surface in the form of other ions, species, or even water. Most probably the band at 1384 cm^{-1} is related to the carbonation of the samples, since it disappears from each sample after 6-months of exposure. Although the presence of other components like metal oxides or graphene oxide from the FT-IR spectra cannot be proven with certainty, it is visible that the intensity of the Si-O-Si bands at 1081 and 777 cm^{-1} changes in the case of the treated samples—the Si-O-Si bands' intensity changes in both types of samples: unexposed and exposed, and is presented in Table 2. These changes could be caused by the presence of metal oxides or other components like graphene oxide on the samples' surface.

Table 2. Ratio changes of the Si-O-Si bands at 777 and 1081 cm^{-1} in the unexposed and exposed samples.

Sample	Unexposed	Exposed
	I_{777} / I_{1081}	I_{777} / I_{1081}
Mortar Blank	0.449	0.309
Mortar TiO_2	0.463	0.391
Mortar TiO_2 + GO-APTES	0.450	0.394
Mortar TiO_2 + SiO_2	0.467	0.545
Mortar TiO_2 + SiO_2 + GO-APTES	0.457	0.516

3.5. Raman spectroscopy measurements on andesite and mortar surface

As already mentioned, andesite is a volcanic rock with a mixed composition consisting in sodium-rich silicates such as plagioclase, pyroxene, and hornblende. The Raman spectra recorded from different zones of the andesite samples (light-grey and dark-grey) are illustrated in Figures 9 and 10. As one can see the spectra are looking different and can be correlated to the specific structural features of the samples. Thus, in the Raman spectra recorded on light-grey zones the most intense bands are located in the 1000-1800 cm^{-1} spectral region, where appear mainly the stretching vibrations in which Si and O atoms are involved, in structural units such as Q_1-Q_4 [41]. In the low wavenumber region of the spectra, between 110 and 700 cm^{-1}, there are a few low intense bands mainly attributed to bending vibrations of bonds in which Si, O and/Al atoms are involved. On the other hand, in the Raman spectra recorded on dark-grey zones the most intense bands are observed in the low wavenumber region. Moreover, as a consequence of the presence of more disordered structure, the elastically scattered light increased the background of the Raman spectra recorded from these zones. This assumption is confirmed by the attenuated intensity of the bands from the high wavenumber region (<1500 cm^{-1}), where the stretching vibrations of more connected Si structural units appear. Besides the bands due to the bending vibrations of Si, O and/or Al containing bonds some bands due to hornblende vibrations [42], can be also noticed (around 670 cm^{-1}).

By comparing the spectra of the unexposed samples treated with different solutions a few differences can be observed. Thus, one can notice the presence of the band around 150 cm^{-1} due to the TiO_6 vibration [43], mostly intense in the spectra of Andesite-S1 and Andesite-S3 samples. Moreover, one can also remark that in all spectra of the Andesite-S1 sample, recorded from light-grey and dark-grey

zones, the bands from the high wavenumber region are less intense as compared to the ones from the 120-700 cm^{-1} spectral range. This behavior could be due to a reduced number of connected SiO_4 structural units as a consequence of the TiO_2 presence. No clear evidence of the bands given by the GO vibrations can be noticed in the spectra of Andesite-S2 and Andesite-S4 spectra.

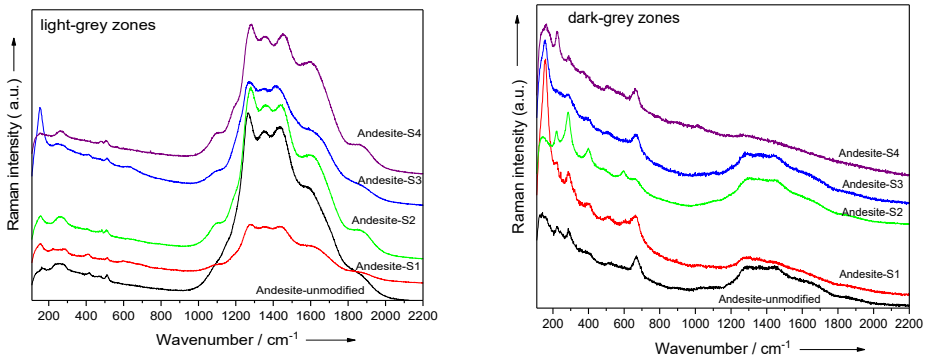

Fig. 9. Raman spectra of the unexposed andesite samples.

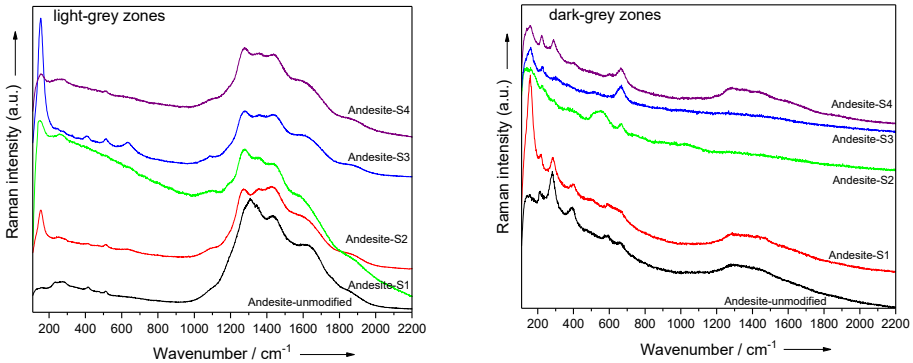

Fig. 10. Raman spectra of the exposed (6 months) andesite samples.

When analyzing the spectra recorded from light-grey zones of exposed samples in comparison to the ones recorded from the unexposed samples one can see that the band around 150 cm^{-1} due to the TiO_6 vibrations is more evident in all spectra of exposed samples and the intensity of the bands from the high wavenumber region slightly decreased. This behavior could indicate that the Ti containing structure

is more stable over the exposure period as compared to the Si containing structure. No important differences can be observed between the spectra recorded from dark-grey zones of the exposed and unexposed samples.

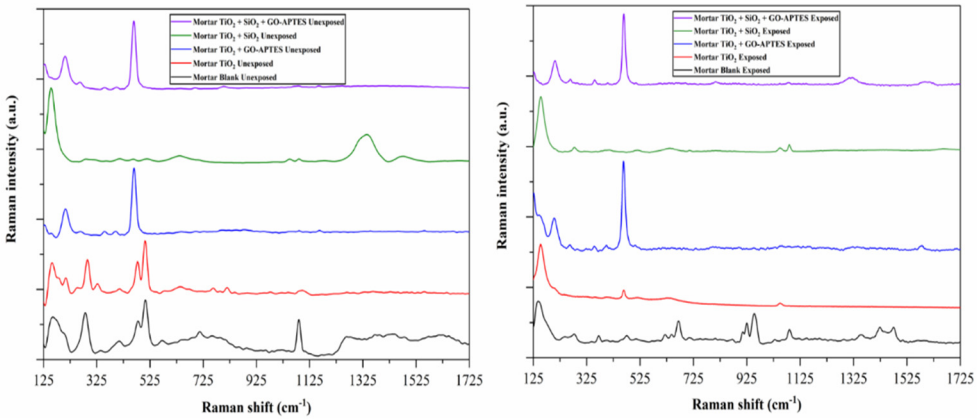

Fig. 11. Raman spectra of the unexposed and exposed (6 months) mortar samples.

As mentioned earlier mortar is a mix of sand, water, and a binding agent like cement, lime or plaster. The Raman spectra of the unexposed blank mortar sample present Raman bands at 160, 281, 410, 480, 507, 571, 712 and 1085 cm^{-1}. The sharp band at 1085 cm^{-1} was attributed to the symmetric stretching mode of carbonate ions, the band at 712 cm^{-1} corresponds to the in-plane bending vibrations of carbonate, respectively the bands at 281 and 160 cm^{-1} were attributed to the rotational and translational lattice modes, which are specific for calcite and vaterite [44].

The presence of gypsum in the sample was confirmed by the bands at 410 cm^{-1}. The doublet at 480 and 507 cm^{-1} was associated with the presence of plagioclase, these bands correspond to the stretching vibrations of the SiO_4 or AlO_4 tetrahedra, whereas the broad band at 571 cm^{-1} was assigned to the Si-O stretching vibrations [45].

Comparing the unexposed blank mortar sample with the exposed one interesting change can be observed between the two samples' spectra. The intensity of the 1085 cm^{-1} band decreased and the bands at 712, 507 and 480 cm^{-1} disappeared, which can be explained by the fact that the sample's surface was covered with pollution. The bands below 300 cm^{-1} also have disappeared, or shifted to lower wavenumbers, hinting that by exposing the mortar samples to the weather conditions structural changes will occur on the mortar surface. The exposed sample presented new bands at 143, 669, 926 and 953 cm^{-1}. The band at 143 cm^{-1} was attributed to

the lattice vibrations of Ca-O polyhedra, at 669 cm^{-1} to the Si-O-Si symmetric bending, respectively the bands at 926 and 953 cm^{-1} were attributed to the asymmetric stretching of the SiO_4 tetrahedra [46].

The Raman spectra of the Mortar TiO_2 unexposed sample at first glance is similar with the Mortar Blank sample, but it is obvious that the bands at 1085 and 712 cm^{-1} disappeared, and this was caused probably by the presence of TiO_2 on the samples' surface. The bands at 208, 410, and 638 cm^{-1} correspond to the TiO_2 anatase phase [47, 48]. After exposing the sample for six months the corresponding TiO_2 anatase phase Raman bands were identified in the spectra at 152, 208, 515 and 638 cm^{-1}. Two other bands were also observed in the exposed sample's spectra at 464 and 1050 cm^{-1}, which were attributed to the silicate and calcite components from mortar.

Two intense Raman bands were observed in the unexposed Mortar TiO_2+GO-APTES sample: at 208 and 464 cm^{-1}, from which the first is linked to the presence of TiO_2, respectively the second to the presence of an increased number of O-Si-O bonds on the surface. The presence of TiO_2 was also proved by the less intense band at 396 cm^{-1}. After exposing the sample for six months almost identical Raman spectra was obtained for the sample, the most notable difference was that the intensity of the band at 464 cm^{-1} has increased, respectively it became narrower. Although the corresponding D and G bands for graphene oxide were not observed in the Raman spectra, the very intense band at 464 cm^{-1} could be caused by the presence of APTES on the sample's surface, since this compound is rich in Si-O-C_2H_5 bonds.

Regarding the Mortar TiO_2+SiO_2 sample, Raman bands corresponding to the TiO_2 anatase phase were observed at 154, 514 and 636 cm^{-1}. Two other bands with relatively small intensity were identified at 1050 and 1085 cm^{-1}, these bands correspond to the silicate and calcite components of mortar. Another band at 1339 cm^{-1} and a shoulder at 1477 cm^{-1} were observed in the Raman spectra, which are most probably linked to the presence of calcium hydroxide phosphate and calcium oxalate dihydrate. After the samples were exposed for 6 months the band at [49] 1339 cm^{-1} and the shoulder at 1477 cm^{-1} disappeared from the spectra, whereas the bands at 1050 and 1085 cm^{-1}, became more intense and narrower. Corresponding band to anatase TiO_2 were observed at 638, 517 and 154 cm^{-1}. SiO_2 presence on the sample surface was not evident from the Raman spectra.

Concerning the Mortar TiO_2+SiO_2+GO-APTES sample Raman bands were identified at 130, 206, 262 and 464 cm^{-1}. The presence of TiO_2 was evidenced only by the band at 130 cm^{-1}, the band at 514 is masked by the intense band at 464 cm^{-1}, respectively the band at 636 cm^{-1} was a very broad and low intensity shoulder. The bands at 206 and 262 were cm^{-1} attributed to the presence of SiO_2 [50].

Although the sharp and intense band at 464 cm^{-1} is generally attributed to SiO_2, in this context it is worth mentioning, that this band corresponds to the Si-O-Si/O-Si-O bridging vibrations [51], which could prove the presence of APTES. After exposing the sample for six months to the weather conditions, the same bands were observed as before (130, 206, 262 and 464 cm^{-1}), but in this case also the bands had higher intensity and were narrower. Another band specific for SiO_2 was observed at 355 cm^{-1}. After the exposure two modifications were observed in the Raman spectra: a doublet at 1309 and 1320 cm^{-1}, respectively a shoulder at 1591 cm^{-1}. The bands at 1309 and 1591 cm^{-1} can be attributed to the D and G bands of the functionalized graphene oxide (GO-APTES) [52].

According to the Raman spectra of the unexposed and exposed samples we can draw the conclusion that blank mortar stability decreases after being exposed to the weather conditions for six months. However, by adding only three layers of TiO_2, TiO_2+GO-APTES, TiO_2+SiO_2 or TiO_2+SiO_2+GO-APTES colloidal solution, the stability of the mortar samples remains constant, or possibly it reaches even higher stability, leading to the conclusion that this method of applying colloidal solution on the samples' surface is a viable option.

CONCLUSIONS

A mixture of three components (TiO2, SiO2 and GO-APTES) was tested for consolidation of the surface of two sample types (i.e. andesite and mortar). Also, suspensions that contains TiO_2, TiO_2+GO-APTES, TiO_2+SiO_2 were investigated as blanks for three-components suspension. The unmodified and modified with different suspensions samples were investigated with microscopic techniques (optic and SEM), X-ray diffraction (XRD and EDX), FT-IR and Raman techniques before and after 6 months of ambient exposure.

After investigation was found that the stability of the three-components treated samples remains constant, or possibly it reaches in time even higher stability. This leading to the conclusion that the obtained suspension is a viable option in stone and mortar consolidation-restoration field.

ACKNOWLEDGMENTS

The authors acknowledge UBBTeMATIC-Art P_40_374 project for the financial support. L. B. would like to acknowledge the financial support provided by STAR-UBB Advanced Fellowship.

REFERENCES

[1] L. Dei and B. Salvadori, "Nanotechnology in cultural heritage conservation: nanometric slaked lime saves architectonic and artistic surfaces from decay," *J. Cult. Herit.*, vol. 7, no. 2, pp. 110–115, 2006, doi: 10.1016/j.culher.2006.02.001.

[2] A. L. Linsebigler, G. Lu, and J. T. Yates, "Photocatalysis on TiO2 Surfaces: Principles, Mechanisms, and Selected Results," *Chem. Rev.*, vol. 95, no. 3, pp. 735–758, 1995, doi: 10.1021/cr00035a013.

[3] P. Munafò, G. B. Goffredo, and E. Quagliarini, "TiO2-based nanocoatings for preserving architectural stone surfaces: An overview," *Constr. Build. Mater.*, vol. 84, pp. 201–218, 2015, doi: 10.1016/j.conbuildmat.2015.02.083.

[4] A. Sierra-Fernandez, L. S. Gomez-Villalba, M. E. Rabanal, and R. Fort, "New nanomaterials for applications in conservation and restoration of stony materials: A review," *Mater. Constr.*, vol. 67, no. 325, 2017, doi: 10.3989/mc.2017.07616.

[5] R. Wang *et al.*, "Light-induced amphiphilic surfaces [4]," *Nature*, vol. 388, no. 6641, pp. 431–432, 1997, doi: 10.1038/41233.

[6] A. Maury and N. de Belie, "State of the art of TiO2 containing cementitious materials: Self-cleaning properties," *Mater. Constr.*, vol. 60, no. 298, pp. 33–50, 2010, doi: 10.3989/mc.2010.48408.

[7] J. Chen and C. sun Poon, "Photocatalytic construction and building materials: From fundamentals to applications," *Build. Environ.*, vol. 44, no. 9, pp. 1899–1906, 2009, doi: 10.1016/j.buildenv.2009.01.002.

[8] M. Pelaez *et al.*, "A review on the visible light active titanium dioxide photocatalysts for environmental applications," *Appl. Catal. B Environ.*, vol. 125, pp. 331–349, 2012, doi: 10.1016/j.apcatb.2012.05.036.

[9] O. Carp, C. L. Huisman, and A. Reller, "Photoinduced reactivity of titanium dioxide," *Prog. Solid State Chem.*, vol. 32, no. 1–2, pp. 33–177, 2004, doi: 10.1016/j.progsolidstchem.2004.08.001.

[10] M. Batzill, "Fundamental aspects of surface engineering of transition metal oxide photocatalysts," *Energy Environ. Sci.*, vol. 4, no. 9, pp. 3275–3286, 2011, doi: 10.1039/c1ee01577j.

[11] J. Schneider *et al.*, "Schneider et al. - 2014 - Understanding TiO 2 Photocatalysis Mechanisms and Materials(2).pdf," *Chem. Rev.*, vol. 114, no. 9, p. 9919−9986, 2014.

[12] J. Chen, F. Qiu, W. Xu, S. Cao, and H. Zhu, "Recent progress in enhancing photocatalytic efficiency of TiO2-based materials," *Appl. Catal. A Gen.*, vol. 495, pp. 131–140, 2015, doi: 10.1016/j.apcata.2015.02.013.

[13] X. Kang, S. Liu, Z. Dai, Y. He, X. Song, and Z. Tan, *Titanium dioxide: From engineering to applications*, vol. 9, no. 2. 2019.

[14] N. Zhang, Y. Zhang, and Y. J. Xu, "Recent progress on graphene-based photocatalysts: Current status and future perspectives," *Nanoscale*, vol. 4, no. 19, pp. 5792–5813, 2012, doi: 10.1039/c2nr31480k.

[15] S. Linley, Y. Liu, C. J. Ptacek, D. W. Blowes, and F. X. Gu, "Recyclable graphene oxide-supported titanium dioxide photocatalysts with tunable properties," *ACS Appl. Mater. Interfaces*, vol. 6, no. 7, pp. 4658–4668, 2014, doi: 10.1021/am4039272.

[16] E. SOLANO BERRAL, "Sobre un caso de cervicitis gonocócia y gestación.," *Medicamenta (Madr).*, vol. 10, no. 215, p. 224, 1952.

[17] J. Shen, B. Yan, M. Shi, H. Ma, N. Li, and M. Ye, "One step hydrothermal synthesis of TiO2-reduced graphene oxide sheets," *J. Mater. Chem.*, vol. 21, no. 10, pp. 3415–3421, 2011, doi: 10.1039/c0jm03542d.

[18] D. Feng *et al.*, "Portland cement paste modified by TiO2 nanoparticles: A microstructure perspective," *Ind. Eng. Chem. Res.*, vol. 52, no. 33, pp. 11575–11582, 2013, doi: 10.1021/ie4011595.

[19] Z. Li, S. Ding, X. Yu, B. Han, and J. Ou, "Multifunctional cementitious composites modified with nano titanium dioxide: A review," *Compos. Part A Appl. Sci. Manuf.*, vol. 111, pp. 115–137, 2018, doi: 10.1016/j.compositesa.2018.05.019.

[20] C. Mendoza, A. Valle, M. Castellote, A. Bahamonde, and M. Faraldos, "TiO2 and TiO2-SiO2 coated cement: Comparison of mechanic and photocatalytic properties," *Appl. Catal. B Environ.*, vol. 178, pp. 155–164, 2015, doi: 10.1016/j.apcatb.2014.09.079.

[21] A. Naumann, I. Stephan, and M. Noll, "Material resistance of weathered wood-plastic composites against fungal decay," *Int. Biodeterior. Biodegrad.*, vol. 75, pp. 28–35, 2012, doi: 10.1016/j.ibiod.2012.08.004.

[22] C. Kapridaki, L. Pinho, M. J. Mosquera, and P. Maravelaki-Kalaitzaki, "Producing photoactive, transparent and hydrophobic SiO2-crystalline TiO2 nanocomposites at ambient conditions with application as self-cleaning coatings," *Appl. Catal. B Environ.*, vol. 156–157, pp. 416–427, 2014, doi: 10.1016/j.apcatb.2014.03.042.

[23] S. Khannyra, M. Luna, M. L. A. Gil, M. Addou, and M. J. Mosquera, "Self-cleaning durability assessment of TiO2/SiO2 photocatalysts coated concrete: Effect of indoor and outdoor conditions on the photocatalytic activity," *Build. Environ.*, vol. 211, p. 108743, 2022, doi: 10.1016/j.buildenv.2021.108743.

[24] M. Zhang, L. Shi, S. Yuan, Y. Zhao, and J. Fang, "Synthesis and photocatalytic properties of highly stable and neutral TiO2/SiO2 hydrosol," *J. Colloid Interface Sci.*, vol. 330, no. 1, pp. 113–118, 2009, doi: 10.1016/j.jcis.2008.10.038.

[25] X. Li and J. He, "Synthesis of Raspberry-Like SiO 2 − TiO 2 Nanoparticles toward Antire fl ective and Self-Cleaning Coatings," 2013.

[26] R. Fateh, R. Dillert, and D. Bahnemann, "Preparation and characterization of transparent hydrophilic photocatalytic TiO2/SiO2 thin films on polycarbonate," *Langmuir*, vol. 29, no. 11, pp. 3730–3739, 2013, doi: 10.1021/la400191x.

[27] M. C. Dudescu, I. Olteanu, L. C. Cotet, and V. Danciu, "APTES Functionalized Graphene Oxide for Silane-Based Mortar Performances," vol. 20, no. xx, pp. 1–9, 2020, doi: 10.1166/jnn.2020.18958.

[28] L. C. Cotet, K. Magyari, M. Todea, M. C. Dudescu, V. Danciu, and L. Baia, "Versatile self-assembled graphene oxide membranes obtained under ambient conditions by using a water-ethanol suspension," *J. Mater. Chem. A*, vol. 5, no. 5, pp. 2132–2142, 2017, doi: 10.1039/C6TA08898H.

[29] D. C. Marcano *et al.*, "Improved synthesis of graphene oxide," *ACS Nano*, vol. 4, no. 8, pp. 4806–4814, 2010, doi: 10.1021/nn1006368.

[30] M. Pavlovic, M. Dojcinovic, R. Prokic-Cvetkovic, L. Andric, Z. Ceganjac, and L. Trumbulovic, "Cavitation wear of basalt-based glass ceramic," *Materials (Basel).*, vol. 12, no. 9, 2019, doi: 10.3390/ma12091552.

[31] A. T. Djowe, S. Laminsi, D. Njopwouo, E. Acayanka, and E. M. Gaigneaux, "Surface modification of smectite clay induced by non-thermal gliding arc plasma at atmospheric pressure," *Plasma Chem. Plasma Process.*, vol. 33, no. 4, pp. 707–723, 2013, doi: 10.1007/s11090-013-9454-8.

[32] Y. Liu, F. Zeng, B. Sun, P. Jia, and I. T. Graham, "Structural characterizations of aluminosilicates in two types of fly ash samples from Shanxi Province, North China," *Minerals*, vol. 9, no. 6, pp. 1–16, 2019, doi: 10.3390/min9060358.

[33] L. Y. Yu, Z. X. Huang, and M. X. Shi, "Synthesis and characterization of silica by sol-gel method," *Adv. Mater. Res.*, vol. 1030–1032, pp. 189–192, 2014, doi: 10.4028/www.scientific.net/AMR.1030-1032.189.

[34] J. T. Kloprogge, *Infrared and Raman Spectroscopies of Pillared Clays*, 1st ed., vol. 8. Elsevier Ltd., 2017.

[35] A. Eisazadeh, K. A. Kassim, and H. Nur, "Solid-state NMR and FTIR studies of lime stabilized montmorillonitic and lateritic clays," *Appl. Clay Sci.*, vol. 67–68, pp. 5–10, 2012, doi: 10.1016/j.clay.2012.05.006.

[36] R. Babilas, A. Bajorek, A. Radoń, and R. Nowosielski, "Corrosion study of resorbable Ca60Mg15Zn25 bulk metallic glasses in physiological fluids," *Prog. Nat. Sci. Mater. Int.*, vol. 27, no. 5, pp. 627–634, 2017, doi: 10.1016/j.pnsc.2017.08.011.

[37] M. A. Legodi, D. De Waal, J. H. Potgieter, and S. S. Potgieter, "Technical note rapid determination of CaCo3 in mixtures utilising FT-IR spectroscopy," *Miner. Eng.*, vol. 14, no. 9, pp. 1107–1111, 2001, doi: 10.1016/S0892-6875(01)00116-9.

[38] F. B. Reig, J. V. G. Adelantado, and M. C. M. Moya Moreno, "FTIR quantitative analysis of calcium carbonate (calcite) and silica (quartz) mixtures using the constant ratio method. Application to geological samples," *Talanta*, vol. 58, no. 4, pp. 811–821, 2002, doi: 10.1016/S0039-9140(02)00372-7.

[39] A. V. Oancea *et al.*, "Multi-analytical characterization of Cucuteni pottery," *J. Eur. Ceram. Soc.*, vol. 37, no. 15, pp. 5079–5098, 2017, doi: 10.1016/j.jeurceramsoc.2017.07.018.

[40] B. J. Saikia, "Spectroscopic Estimation of Geometrical Structure Elucidation in Natural SiO₂ Crystal," *J. Mater. Phys. Chem.*, vol. 2, no. 2, pp. 28–33, 2014, doi: 10.12691/jmpc-2-2-3.

[41] J. J. Freeman, A. Wang, K. E. Kuebler, B. L. Jolliff, and L. A. Haskin, "Characterization of natural feldspars by raman spectroscopy for future planetary exploration," *Can. Mineral.*, vol. 46, no. 6, pp. 1477–1500, 2008, doi: 10.3749/canmin.46.6.1477.

[42] A. I. Apopei, V. Diaconu, C. Muzeal, J. Neamț, and A. Buzatu, "The composition and source of the raw material of two stone axes of Late Bronze Age from Neamț County (Romania)-A Raman study," no. March, 2018, [Online]. Available: http://geology.uaic.ro/auig/.

[43] Y. Zhang, C. K. Chan, J. F. Porter, and W. Guo, "Powders Prepared By Vapor Hydrolysis," vol. 13, no. 9, 1998.

[44] F. C. Donnelly, F. Purcell-Milton, V. Framont, O. Cleary, P. W. Dunne, and Y. K. Gun'ko, "Synthesis of CaCO3 nano- and micro-particles by dry ice carbonation," *Chem. Commun.*, vol. 53, no. 49, pp. 6657–6660, 2017, doi: 10.1039/c7cc01420a.

[45] J. R. Johnson, S. J. Jaret, T. D. Glotch, and M. Sims, "Raman and Infrared Microspectroscopy of Experimentally Shocked Basalts," *J. Geophys. Res. Planets*, vol. 125, no. 2, pp. 0–3, 2020, doi: 10.1029/2019JE006240.

[46] S. Ortaboy *et al.*, "Effects of CO2 and temperature on the structure and chemistry of C-(A-)S-H investigated by Raman spectroscopy," *RSC Adv.*, vol. 7, no. 77, pp. 48925–48933, 2017, doi: 10.1039/c7ra07266j.

[47] R. Taziwa, E. Meyer, and N. Takata, "Structural and Raman Spectroscopic Characterization of C-TiO 2 Nanotubes Synthesized by a Template-Assisted Sol-Gel Technique," *J. Nanosci. Nanotechnol. Res.*, vol. 1, no. 1, pp. 1–11, 2017, doi: 10.4229/EUPVSEC20172017-3DV.2.103.

[48] R. Kaveh, M. Mokhtarifar, M. Bagherzadeh, A. Lucotti, M. V. Diamanti, and M. P. Pedeferri, "Magnetically recoverable TiO2/SiO2/γ-Fe2O3/rGO composite with significantly enhanced UV-visible light photocatalytic activity," *Molecules*, vol. 25, no. 13, 2020, doi: 10.3390/molecules25132996.

[49] G. Marucci, A. Beeby, A. W. Parker, and C. E. Nicholson, "Raman spectroscopic library of medieval pigments collected with five different wavelengths for investigation of illuminated manuscripts," *Anal. Methods*, vol. 10, no. 10, pp. 1219–1236, 2018, doi: 10.1039/c8ay00016f.

[50] O. F. S. Polymorphs, "DEPENDENCE SPECTRA a resolution," pp. 347–359, 1987.

[51] P. Schmidt, L. Bellot-Gurlet, A. Slodczyk, and F. Fröhlich, "A hitherto unrecognised band in the Raman spectra of silica rocks: Influence of hydroxylated Si-O bonds (silanole) on the Raman moganite band in chalcedony and flint (SiO 2)," *Phys. Chem. Miner.*, vol. 39, no. 6, pp. 455–464, 2012, doi: 10.1007/s00269-012-0499-7.

[52] M. Musielak, A. Gagor, B. Zawisza, E. Talik, and R. Sitko, "Graphene Oxide/Carbon Nanotube Membranes for Highly Efficient Removal of Metal Ions from Water," *ACS Appl. Mater. Interfaces*, vol. 11, no. 31, pp. 28582–28590, 2019, doi: 10.1021/acsami.9b11214.

STUDIA UBB PHYSICA, Vol. 67 (LXVII), 1-2, 2022, pp. 79-90
(RECOMMENDED CITATION)
doi:10.24193/subbphys.2022.07

ENHANCING THE PHOTOLUMINESCENCE OF POLYFLUORENE-BASED THIN FILMS VIA ILLUMINATION

I. PETROVAI[1,2], O. TODOR-BOER[3], L. DAVID[1], I. BOTIZ[1,2*]

ABSTRACT. We show in this work that exposing thin films of conjugated poly[9,9-bis(2-ethylhexyl)-9*H*-fluorene-2,7-diyl] to light under nitrogen atmosphere led to an increase of their emission up to 2.2 folds. This enhancement was due to the appearance of structural changes in the glassy and β-phase conformations induced upon thin film illumination, as revealed by the Franck-Condon analysis of the photoluminescence spectra. Interestingly, the photoluminescence of thin films remained at the enhanced value for 75 days after stopping the illumination, most probably due to the permanent structural changes induced upon illumination.

Keywords: *conjugated polymers, illumination, photoluminescence, β-phase conformations.*

INTRODUCTION

Due to the evident structure-property relationship existent in conjugated polymeric materials [1–7], the scientific community is continuously looking for novel processing methods to manipulate, control and tune the microstructure of conjugated materials, with the aim to improve their optoelectronic properties and consequently, the functionality of potential organic devices. Detailed information on various processing methods prominently adopted by scientists are well described in the literature [8–10]. One of such processing tools appears to be the exposure to light [11–16]. Scientific reports have shown that illumination of conjugated polymers with white light in controlled nitrogen atmosphere influenced the behavior of an

[1] *Faculty of Physics, Babeș-Bolyai University, 400084 Cluj-Napoca, Romania*
[2] *Interdisciplinary Research Institute on Bio-Nano-Sciences, Babeș-Bolyai University, 400271 Cluj-Napoca, Romania*
[3] *INCDO-INOE 2000, Research Institute for Analytical Instrumentation, 400293 Cluj-Napoca, Romania*
[*] *Corresponding author: ioan.botiz@ubbcluj.ro*

ensemble of conjugated molecules, *i.e.*, their mechanical properties such as viscosity [11]. Several other experiments have shown that conjugated materials such as poly(3-hexylthiophene-2,5-diyl) (P3HT) and the poly[2-methoxy-5-((2'-ethylhexyl)oxy)-1,4-phenylenvinylene] (MEH-PPV) chains suffered conformational changes in solutions and adopted more coiled-like conformation when illuminated [14,15]. Similar behavior was observed in thin films [16]. Moreover, structural changes of MEH-PPV in thin films were reported along with an increase in photoluminescence (PL) upon illumination in nitrogen [12,13]. The enhancement of the PL properties in thin films was tentatively attributed to structural changes induced by photoexcitations.

In this work, we study the alteration of PL properties of conjugated poly[9,9-bis(2-ethylhexyl)-9*H*-fluorene-2,7-diyl] (PFO) films upon illumination. Our aim is to find out how different type of light used in the illumination process impacts the PL enhancement in such polymer films and to reveal the best experimental conditions under which the PL enhancement is maximized and, eventually, remains stable for long periods of time. Such information might then be useful in the design of future energy devices, including light-emitting diodes.

EXPERIMENTAL

PFO of a weight-average molecular weight M_w = 13.2 kg/mol, number-average molecular weight M_n= 6.8 kg/mol and polydispersity $Đ$ = 1.94, was purchased from Sigma-Aldrich. Thin films of PFO (127±5 nm in thickness) were prepared by spin casting at 2000 rpm from a toluene solution. For all films, regular microscopy cover glass, previously cleaned in UV-ozone for 20 minutes, was used as substrate.

Absorption spectra of thin films were acquired using a V-530 UV-VIS spectrophotometer from Jasco (spectral range of 190-1100 nm). PL spectra were collected using an FP-6500 Spectrofluorometer from Jasco (excitation wavelength range of 220-750 nm). All PL spectra were recorded using an excitation wavelength of 375 nm. Illumination of all films was always performed both at controlled temperature and in nitrogen atmosphere inside a Linkam hot stage (model THMS 600 that was equipped with a precise temperature controller in the range of -196°C to 600 °C and which could be continuously flashed with nitrogen flow).

Different LED sources from Thorlabs were used to illuminate the PFO films: SOLIS-1A/M (white cold), SOLIS-365A/M, SOLIS-385A/M, SOLIS-445B/M, SOLIS-525A/M and SOLIS-623A/M. The sources were operated using a ThorlabsDC2200 (1 Channel) LED driver, the latter being also used to precisely control the power of LEDs. Illumination of PFO films at 30°C for 45 minutes was done using a white xenon lamp (powered by 50 W and equipped with a UV filter).

RESULTS AND DISCUSSION

Figure 1a depicts the large increase of the PL intensity of PFO films upon their illumination with white light at a constant temperature of 30 °C in nitrogen atmosphere. The longer the films were illuminated, the higher their PL intensity became. Nonetheless, illuminating PFO films beyond 2 hours did not lead to any further increase in PL intensity. To exclude possible alterations of PL due to contaminations with oxygen [17], control experiments, using films prepared from solutions nitrogen-bubbled in anhydrous toluene, were performed inside a nitrogen-flooded glove box (with oxygen content < 10 ppm [18]). Results shown in Figure 1b proved that, even under such circumstances, the PFO film still exhibited a clear PL enhancement when exposed to light.

To quantify the enhancement of PL upon illumination, we have extracted the I_{PL}/I_{ref} ratio for various illumination times. Here, I_{PL} is the PL intensity of the total area under the peak measured for each illuminated film. Instead, I_{ref} is the PL area peak intensity corresponding to a nonilluminated reference film. Figure 1c shows the evolution of this ratio with the illumination time. The PL intensity increased by 1.5 folds in less than 15 minutes of illumination and kept increasing up to 2 folds after 2 hours of illumination. Indeed, beyond this time no further increase in PL was observed. In order to exclude a possibly PL alteration due to the incomplete solvent evaporation upon spin casting, we have monitored the PL of other reference PFO films that were prepared under same conditions, but kept for specific times in dark (no light was allowed to shine on these films). The evolution of the I_{PL}/I_{ref} ratio of these films, as depicted in Figure 1c by the square symbols, showed that there was only a weak (several %) variation of the PL intensity that could be attributed to solvent traces remaining in PFO films. Therefore, our results clearly showed that illuminating PFO films with white light induced large enhancement in their PL intensity.

We have repeated all the experiments described above once more, but this time we kept the PFO films at 70 °C (Figure 1d). In this case, the PL intensity doubled in less than 5 minutes of film illumination and further increased to a maximum of 2.2 folds after 12 minutes of illumination. Instead, the illumination of PFO films for times longer than 40 minutes led to a decrease of the PL intensity. Again, almost no PL alteration attributed to solvent traces was detected for the control samples kept in dark. Furthermore, by fixing the illumination time to 30 minutes, we have varied the film temperature at which illumination was performed. The obtained results, shown in Figure 1e, revealed a clear dependence of the PL increase with respect to the film temperature and the best PL enhancement happened at 70 °C. Above 70 °C, the PL decreased, probably due to an increased mobility of PFO molecules (PL also

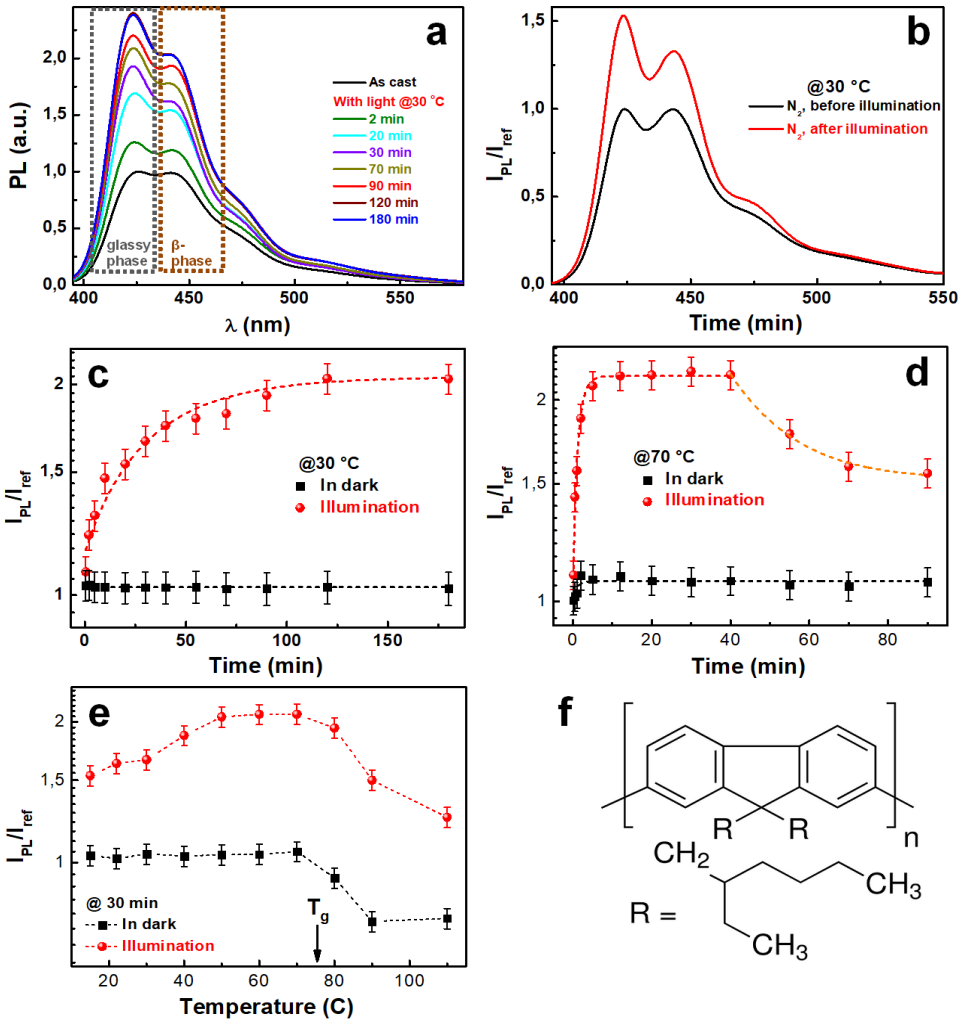

Figure 1. (a) PL spectra of PFO films before and after illumination at 30 °C for various times. Spectral components of the glassy and β-phases are indicated by the dotted rectangular shapes. (b) Normalized PL spectra of a PFO film before and after its illumination at 30 °C for 45 minutes inside a glove box filled with nitrogen. This PFO film was obtained from a solution that was prepared using anhydrous toluene and that was then bubbled with nitrogen before further use. (c-d) PL enhancement of PFO films illuminated at 30 °C (c) and at 70 °C (d) as a function of illumination time. Dashed black and red lines in (c) and (d) are fits of single exponential growth functions, while the dashed orange line in (d) was fitted using a single exponential decay function. (e) PL enhancement of PFO films illuminated for 30 minutes at various temperatures. Square symbols show the PL changes taking place in the reference films kept in dark. Illumination of films was performed in nitrogen atmosphere and using a white cold LED source with an output power of ~252 mW. The black arrow indicates the expected T_g for PFO films (f) Chemical structure of PFO system.

decreased for the reference films kept in dark) caused by the transition to a less glassy state, as the glass transition temperature T_g was estimated to be around 70-75 °C for PFO films. Our flash differential scanning calorimetry measurements in bulk revealed a T_g of about 84 °C for this PFO system (see its chemical structure in Figure 1f). Nonetheless, it is well-known that, for a specific polymer, the T_g in thin films is lower than the T_g in the bulk [19–23]. Thus, above 70 °C the effect of illumination might have been diminished by other conformational changes induced thermally [24,25]. For the lower film temperatures, the PL amplification was smaller too but, according to Figure 1c, this PL amplification, that corresponded to only 30 minutes of illumination, did not reach yet the maximum of PL enhancement observed for longer illumination times (*i.e.*, 2 hours).

The photophysical properties of PFO are known to strongly depend on the film microstructure [26,27]. Therefore, one possibility is to link the PL enhancement upon illumination to conformational changes, especially when knowing that thin PFO films generally display the coexistence of two phases. In the glassy phase, PFO molecules adopt a range of disordered wormlike conformations characterized by a broad distribution of intermonomer torsion angles [28,29]. Instead, in the β-phase, PFO molecules adopt an extended coplanar geometry with a torsion angle of 165°-180° between the adjacent fluorene units [28–33]. In order to follow the possible changes of the glassy and β-phases in PFO films during illumination, we have performed a Franck-Condon analysis (FCA; details on FCA are described elsewhere [34]) on the PL spectra shown in Figure 1a. For that, two molecular species corresponding to the glassy phase and the β-phase conformations, that exist in an intermediary state (*i.e.*, within the PL spectrum recorded after 90 minutes of illumination), were separated and scaled appropriately to all the other PL spectra recorded at different illumination times. For instance, Figure 2a and Figure 2b display the separation and scaling of glassy and β-phase contributions to PL spectra of Figure 1a recorded at 0 and 180 minutes of illumination. Furthermore, the data points of Figure 1c (red spherical symbols) were normalized to 100% at the time corresponding to 0 minutes of illumination and were then fitted using a single exponential growth function. The glassy and β-phase spectra for all illumination times were further integrated and their fraction on the total integrated PL intensity was calculated (Figure 2c). Fits through the spectra (as a guide to the eye) were done using single exponential growth functions. Note that the parameters that we have used in the FCA, including Huang-Rhys parameters, are comparable to the parameters reported in the literature [35]. The obtained results have shown that, while the fraction of glassy phase was increasing from about 88% to 94%, the fraction of β-phase was decreasing from around 11% to about 5% when increasing the illumination time from 0 to 180 minutes (Figure 2c). Thus, these results clearly proved that illumination was reducing the amount of β-phase

in thin films of conjugated PFO. This observation was further sustained by the fact that the PL ratio between the 422 nm and 442 nm peaks increased upon illumination (this information can be seen when performing the normalization to 422 nm peak of all PL spectra presented in Figure 1a; *not shown*), indicating the appearance of a more disordered, possibly less planarized phase [36].

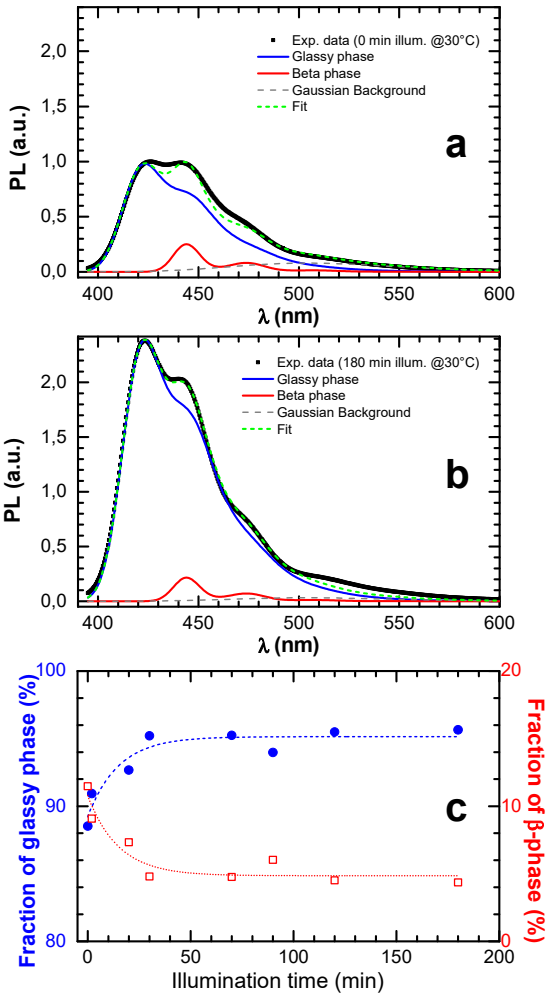

Figure 2. (a-b) Separation and scaling of glassy and β-phase contributions to all the other PL spectra of Figure 1a recorded at 0 and 180 minutes of illumination. (c) Evolution of the glassy and β-phase fractions in PFO films during illumination as deduced from the FCA using data of Figure 1a and Figure 1c. Dotted fits through the spectra were done with a single exponential growth fit $y=y_0+A_1 \cdot \exp(x/t_1)$ for the glassy phase (with y_0*=95%*, A_1*=-5.9%* and t_1*=-14.8 min*) and with another single exponential decay fit $y=y_0+A_1 \cdot \exp(-x/t_1)$ for the β-phase (with y_0*=4.9%*, A_1*=-5.9%* and t_1*=-14.8 min*).

According to the literature, the amount of polymer chains planarized in β-phase conformation determines the PL efficiency [37]. Therefore, we expected a PL alteration to take place upon illumination. While the mechanism by which illumination reduces the β-phase is not clearly understood, the enhancement of PL associated with the reduction of β-phase could be tentatively explained assuming the behavior of the geminate pairs (*i.e.*, charge transfer states) formed from excitons in the β-phase. For instance, the absorption spectra display only weak changes in absorption when PFO films are illuminated, with no visible evidence of the existence of the absorption peak expected to be located around 435-440 nm (*not shown*) and corresponding to the β-phase [34,35,38,39]. This means that there is only a very small amount of β-phase in the PFO films, but with rather efficient energy transfer to it [35,40]. These β-phase sites quench the emission most probably due to the fact that the excitons in the β-phase tend to form geminate pairs rather than to emit light [41]. Therefore, the emission from neat β-phase should be less than emission from the neat glassy phase. Nonetheless, when PFO films are being illuminated and consequently the amount of β-phase is reduced, there is less quenching of the emission and the overall PL efficiency increases. This observation is in line with other results reported in the literature and indicating both that PFO films with lower β-phase fraction exhibit higher PL quantum efficiency [42] and that simple white light exposure sharply retards the growth of conjugated polymer microstructures [15]. Finally, note that although there are many examples in the literature where illumination may alter or keep stable the optoelectronic properties of conjugated polymers [17,43–46], yet the enhancement of PL via illumination might be, to the best of our knowledge, the only example where light has exhibited a beneficial impact on such a material.

In order to study the impact of the type of light, used for the illumination of PFO films, on the PL enhancement, we have replaced the white light with other light sources (*e.g.*, 365 nm, 385 nm, 445 nm, 525 nm and 623 nm). For example, a 2-fold enhancement of PL in PFO films was also observed upon their illumination with light of a wavelength of 385 nm (Figure 3a). In this case, much shorter illumination times of up to only 40 s were sufficient to enhance the PL. Moreover, the general behavior of the I_{PL}/I_{ref} ratio with respect to the illumination time at 30 °C and 70 °C (Figure 3b-c), as well as with respect to the temperature when keeping the illumination time at 40 s (Figure 3d), was like that reported in Figure 1 for the white light.

The enhancement of PL was also significant when utilizing 365 nm and 445 nm light sources (*not shown*). In contrary, when employing light of 525 nm and 623 nm for the illumination of PFO films, the PL enhancement was rather negligible and the maximum PL enhancement depended on the light intensity of each illumination source (*not shown*). Therefore, for a clearer comparison, we have further fixed the output power

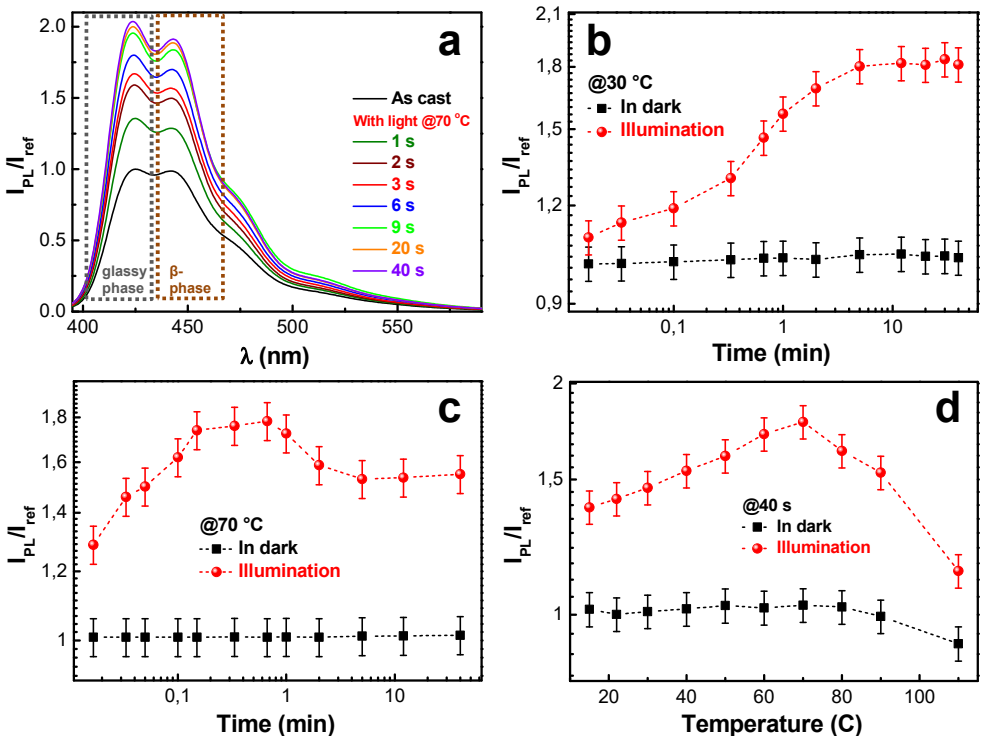

Figure 3. (a) PL spectra of PFO films before and after their illumination at 70 °C for various times. (b-c) PL enhancement of PFO films illuminated at 30 °C (b) and at 70 °C (c) as a function of illumination time. (d) PL enhancement of PFO films illuminated for 40 s while annealed at various temperatures. Square symbols show the PL changes taking place in control PFO films kept in dark. Illumination of films was performed using a 385 nm LED source with an output power of ~ 258 mW. Spectral components of glassy and β-phases are indicated by the dotted rectangular shapes in (a).

of all light sources and measured the corresponding PL enhancements induced in PFO films upon illumination (Figure 4). The most significant enhancement of PL was observed when exciting the glassy phase at 385 nm, as at this wavelength the PFO system absorbs almost 100% of the incoming light (Figure 5a). Furthermore, when illuminating PFO films with light of 445 nm, a significant increase in PL was also noticed, even though the PFO system absorbs at this wavelength only a small fraction of the incoming light (see Figure 5a). This result could be explained by the fact that PFO molecules adopting a β-phase conformation absorb light around 435-440 nm [34,35,38,39].

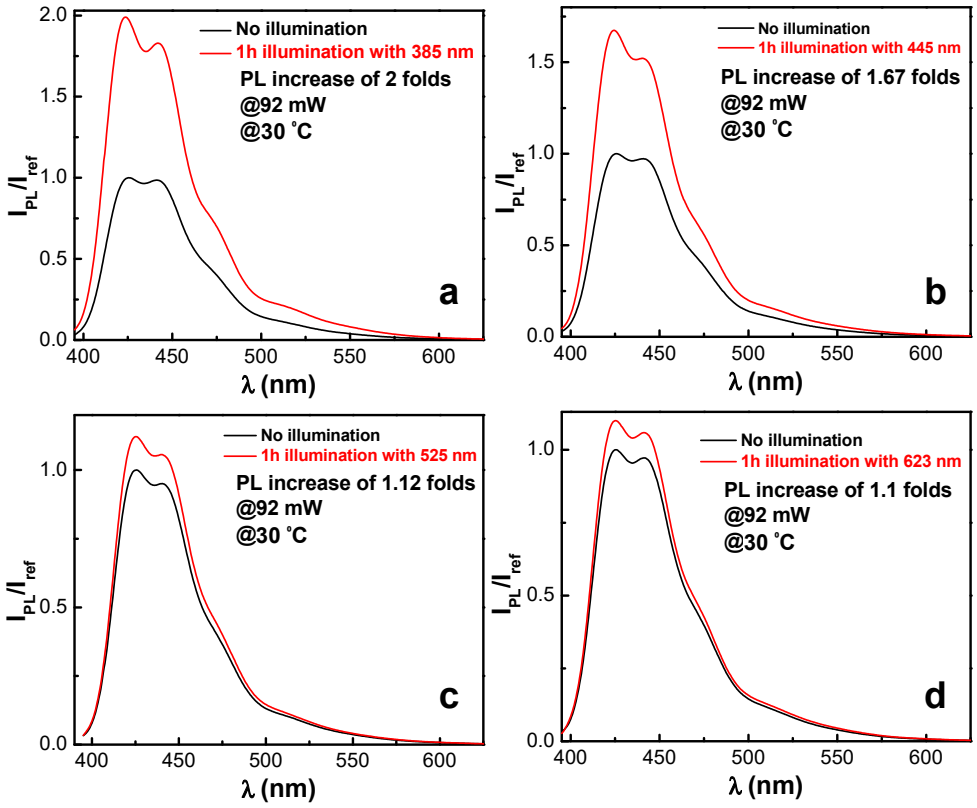

Figure 4. PL spectra of PFO films before and after their illumination at 30 ˚C for 1 hour, by employing 385 nm (a), 445 nm (b), 525 nm (c) and 623 nm (d) LED sources. All these sources worked at an output power of 92 mW.

In order to see how useful the PL enhancement would be for practical applications, we have broken an as spin cast PFO film in two pieces. One piece was simply monitored in dark in nitrogen atmosphere, as a control sample. The other piece was monitored during illumination for 90 minutes in nitrogen. Then, the illumination of the PFO film was stopped and the film was placed in dark in nitrogen atmosphere. We have then periodically measured the PL spectra of both films. The obtained results, summarized in Figure 5b, showed that the PL enhancement remained stable for 75 days, period after which the experiment was stopped. This was most probably due to the permanent and irreversible reduction of the β-phase induced by the illumination. Such irreversibility of the PL enhancement shows good potential for the future design of organic light emitting diodes.

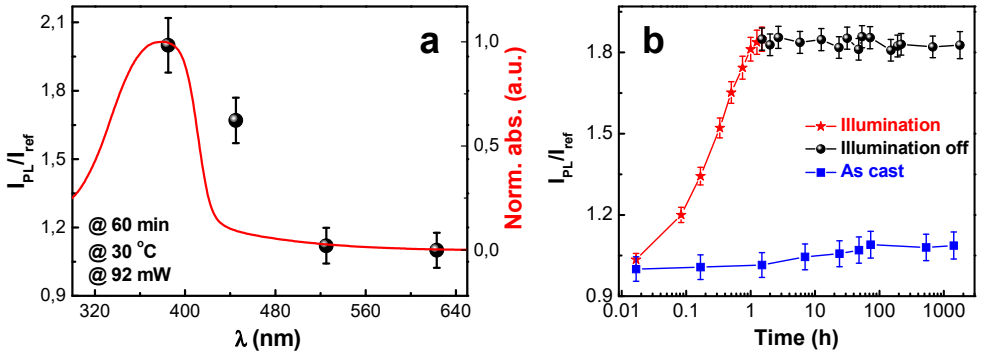

Figure 5. (a) Normalized absorption spectrum (line) of an as spin-cast PFO thin film acquired at 30 °C with the corresponding PL enhancement (symbols) obtained upon the illumination of its analogues using light of a specific wavelength. (b) PL enhancement measured using the total area under the peak for: a spin cast reference PFO film kept in dark (square symbols), a PFO film illuminated with white light (~ 200 mW) for various times (star symbols) and same film monitored in dark after the illumination was stopped (spherical symbols). All films were kept at 30 °C in nitrogen atmosphere.

CONCLUSIONS

We have demonstrated an increase in PL intensity of about 2.2 folds for thin PFO films upon their illumination, in controlled atmosphere, with light of various wavelength and power. The PL enhancement was attributed to the changes in the glassy and β-phase fractions upon illumination and was proven to be stable for many tens of days. Our results showed that PL was increasing to a maximum with the decreasing of the β-phase fraction from around 11% to about 5%, as revealed by the FCA. Moreover, the PL enhancement was shown to depend on the temperature of PFO films. For temperatures below the T_g, a continuous increase in PL intensity with the time of illumination was measured. For temperatures around the T_g, we found an optimal illumination time at which the PL intensity was generally reaching its maximum value. At temperatures higher than T_g, the enhancement of PL was decreasing, most probably due to an increased mobility of PFO molecules caused by the transition to a less glassy state.

ACKNOWLEDGMENTS

O. T-B. and I. B. acknowledge the Core Program within the National Research Development and Innovation Plan 2022-2027, carried out with the support of MCID, project no. PN 23 05, and the financial support of the Romanian National Authority for Scientific Research and Innovation, CNCS – UEFISCDI, project numbers PN-II-RU-TE-2014-4-0013 and PN-III-P1-1.1-TE-2021-0038, respectively. The authors are grateful to A. Köhler for the help with the FCA.

REFERENCES

1. E. Collini and G.D. Scholes, *Science*, **323**, 369–373 (2009).
2. S. Wang, M. Kappl, I. Liebewirth, M. Müller, K. Kirchhoff, W. Pisula, and K. Müllen, *Adv. Mater.*, **24**, 417–420 (2012).
3. B. Ma, B.J. Kim, L. Deng, D.A. Poulsen, M.E. Thompson, and J.M.J. Fréchet, *Macromolecules*, **40**, 8156–8161 (2007).
4. E.D. Como, N.J. Borys, P. Strohriegl, M.J. Walter, and J.M. Lupton, *J. Am. Chem. Soc.*, **133**, 3690–3692 (2011).
5. J.C. Bolinger, M.C. Traub, T. Adachi, and P.F. Barbara, *Science*, **331**, 565–567 (2011).
6. L. Brambilla, M. Tommasini, I. Botiz, K. Rahimi, J.O. Agumba, N. Stingelin, and G. Zerbi, *Macromolecules*, **47**, 6730–6739 (2014).
7. F. Dubin, R. Melet, T. Barisien, R. Grousson, L. Legrand, M. Schott, and V. Voliotis, *Nat. Phys.*, **2**, 32–35 (2006).
8. R.A. Segalman, B. McCulloch, S. Kirmayer, and J.J. Urban, *Macromolecules*, **42**, 9205–9216 (2009).
9. I. Botiz, *J. Mater. Chem. C*, **11**, 364–405 (2023).
10. I. Botiz, S. Astilean, and N. Stingelin, *Polym. Int.*, **65**, 157–163 (2016).
11. I. Botiz, P. Freyberg, N. Stingelin, A.C.M. Yang, and G. Reiter, *Macromolecules*, **46**, 2352–2356 (2013).
12. I. Botiz, P. Freyberg, C. Leordean, A.-M. Gabudean, S. Astilean, A.C.-M. Yang, and N. Stingelin, *ACS Appl. Mater. Interfaces*, **6**, 4974–4979 (2014).
13. I. Botiz, P. Freyberg, C. Leordean, A.-M. Gabudean, S. Astilean, A.C.-M. Yang, and N. Stingelin, *Synth. Met.*, **199**, 33–36 (2015).
14. B. Morgan and M.D. Dadmun, *Eur. Polym. J.*, **89**, 272–280 (2017).
15. B. Morgan and M.D. Dadmun, *Polymer*, **108**, 313–321 (2017).
16. X.L. Ho and J.D. White, *Chem. Phys. Lett.*, **735**, 136753 (2019).
17. V. Bliznyuk, S. Carter, J. Scott, G. Klärner, R. Miller, and D. Miller, *Macromolecules*, **32**, 361–369 (1999).
18. M. Stoessel, G. Wittmann, J. Staudigel, F. Steuber, J. Blässing, W. Roth, H. Klausmann, W. Rogler, J. Simmerer, and A. Winnacker, *J. Appl. Phys.*, **87**, 4467–4475 (2000).
19. S. Napolitano, E. Glynos, and N.B. Tito, *Rep. Prog. Phys.*, **80**, 036602 (2017).
20. J.L. Keddie, R.A. Jones, and R.A. Cory, *Europhys. Lett.*, **27**, 59–64 (1994).
21. M. Chowdhury and R. Priestley, *Proc. Natl. Acad. Sci. USA*, doi/10.1073/pnas.1704886114 (2017).
22. D. Long and F. Lequeux, *Eur. Phys. J. E*, **4**, 371–387 (2001).
23. J.A. Forrest and K. Dalnoki-Veress, *Adv. Colloid Interface Sci.*, **94**, 167–195 (2001).
24. K.-P. Tung, C.-C. Chen, P. Lee, Y.-W. Liu, T.-M. Hong, K.C. Hwang, J.H. Hsu, J.D. White, and A.C.-M. Yang, *ACS Nano*, **5**, 7296–7302 (2011).

25. P.W. Lee, W.-C. Li, B.-J. Chen, C.-W. Yang, C.-C. Chang, I. Botiz, G. Reiter, Y.T. Chen, T.L. Lin, J. Tang, J.-H. Jou, and A.C.-M. Yang, *ACS Nano*, **7**, 6658–6666 (2013).
26. U. Scherf and E.J. List, *Adv. Mater.*, **14**, 477–487 (2002).
27. D. Neher, *Macromol. Rapid Commun.*, **22**, 1365–1385 (2001).
28. A. Perevedentsev, N. Chander, J. Kim, and D.D. Bradley, *J. Polym. Sci. Part B: Polym. Phys.*, **54**, 1995–2006 (2016).
29. W. Chunwaschirasiri, B. Tanto, D. Huber, and M. Winokur, *Phys. Rev. Lett.*, **94**, 107402 (2005).
30. M. Grell, D. Bradley, X. Long, T. Chamberlain, M. Inbasekaran, E. Woo, and M. Soliman, *Acta Polym.*, **49**, 439–444 (1998).
31. C. Liu, Q. Wang, H. Tian, J. Liu, Y. Geng, and D. Yan, *Macromolecules*, **46**, 3025–3030 (2013).
32. A. Perevedentsev, P.N. Stavrinou, D.D.C. Bradley, and P. Smith, *J. Polym. Sci. Part B: Polym. Phys.*, **53**, 1481–1491 (2015).
33. X. Li, Z. Bai, B. Liu, T. Li, and D. Lu, *J. Phys. Chem. C*, **121**, 14443–14450 (2017).
34. A.L.T. Khan, M.J. Banach, and A. Köhler, *Synth. Met.*, **139**, 905–907 (2003).
35. A.L.T. Khan, P. Sreearunothai, L.M. Herz, M.J. Banach, and A. Köhler, *Phys. Rev. B*, **69**, 085201 (2004).
36. I. Botiz, M.-A. Codescu, C. Farcau, C. Leordean, S. Astilean, C. Silva, and N. Stingelin, *J. Mater. Chem. C*, **5**, 2513–2518 (2017).
37. M. Ariu, D. Lidzey, M. Sims, A. Cadby, P. Lane, and D. Bradley, *J. Phys.: Condens. Matter*, **14**, 9975 (2002).
38. A. Cadby, P. Lane, H. Mellor, S. Martin, M. Grell, C. Giebeler, D. Bradley, M. Wohlgenannt, C. An, and Z. Vardeny, *Phys. Rev. B*, **62**, 15604 (2000).
39. C. Rothe, S. King, F. Dias, and A. Monkman, *Phys. Rev. B*, **70**, 195213 (2004).
40. M. Ariu, M. Sims, M. Rahn, J. Hill, A. Fox, D. Lidzey, M. Oda, J. Cabanillas-Gonzalez, and D. Bradley, *Phys. Rev. B*, **67**, 195333 (2003).
41. C. Yang, Z. Vardeny, A. Köhler, M. Wohlgenannt, M.K. Al-Suti, and M.S. Khan, *Phys. Rev. B*, **70**, 241202 (2004).
42. Q. Zhang, L. Chi, G. Hai, Y. Fang, X. Li, R. Xia, W. Huang, and E. Gu, *Molecules*, **22**, 315 (2017).
43. T. Tromholt, M.V. Madsen, J.E. Carle, M. Helgesen, and F.C. Krebs, *J. Mater. Chem.*, **22**, 7592–7601 (2012).
44. S. Alem, S. Wakim, J. Lu, G. Robertson, J. Ding, and Y. Tao, *ACS Appl. Mater. Interfaces*, **4**, 2993–2998 (2012).
45. A. Rivaton, S. Chambon, M. Manceau, J.-L. Gardette, N. Lemaître, and S. Guillerez, *Polymer Degradation and Stability*, **95**, 278–284 (2010).
46. M. Jørgensen, K. Norrman, and F.C. Krebs, *Sol. Energy Mater. Sol. Cells*, **92**, 686–714 (2008).

STUDIA UBB PHYSICA, Vol. 67 (LXVII), 1-2, 2022, pp. 91-106
(RECOMMENDED CITATION)
doi:10.24193/subbphys.2022.08

RASHBA FIELD CONTRIBUTION AND ELECTRIC FIELD CONTROL OF THE MAGNETIC ANISOTROPY

R.-A. ONE[1], C. V. TIUSAN[1,2,*]

ABSTRACT. The anatomy of the Perpendicular Magnetic Anisotropy (PMA) in magnetic multilayered thin film heterostructures and the possibility to efficiently manipulate it by external electric fields represent major issues for technological applications in magnetic data storage devices. Solving a standard quantum model based on a Stoner-Rashba Hamiltonian, we illustrate that the magnetic properties in ultrathin magnetic films arise from the competing components identified in the magnetic energy: the Rashba correction to the Stoner splitting, a pseudo-dipolar contribution to the anisotropy energy proportional to the electric field at the interface that would favor in-plane magnetization configuration and a uniaxial-like perpendicular anisotropy term. This last term is responsible on the perpendicular magnetization configuration in ultrathin films and depends on the square of the electric field at the surface of the film. Investigating the time evolution of the magnetic system, we described the macrospin magnetization dynamics in terms of a Rashba field induced magnetization precession. Despite its simplicity, the quantum approach underlines the basic issues related to the physical origin and the mechanisms of the perpendicular magnetization in ultrathin magnetic films and illustrates the capability of manipulation by external gating electric field, in experiments similarly to Nuclear Magnetic Resonance.

Keywords: *perpendicular magnetic anisotropy, electric field control of anisotropy, magnetic tunnel junctions, magnetic multilayer heterostructures.*

[1] *Babeș-Bolyai University, Faculty of Physics, 1 M. Kogălniceanu, 400084 Cluj-Napoca, Romania*
[2] *National Center of Scientific Research (CNRS), France*
* *Corresponding author: coriolan.tiusan@ubbcluj.ro*

INTRODUCTION

The Perpendicular Magnetic Anisotropy (PMA) in ultrathin magnetic films represents nowadays one of the most developed experimental and theoretical topics in the magnetic data storage technologies. This is correlated to the enhanced thermal stability and the switching efficiency by spin-transfer-torque in magnetic random-access memories devices. A deep understanding of the fundamental physics related the PMA, its intrinsic anatomy and the possibility to control it by external stimuli (e.g. electric fields) in magnetic multilayer structures represents major issues for efficiently operating the magnetic random access memories (MRAM) devices [1]. Particularly, in case of ultrathin magnetic films, the magnetic anisotropy can be driven by interface effects. This opens the possibility of its control by external electric fields (E-field), that can be applied at the ferromagnetic film interface in cleverly designed spintronic device geometries. The non-zero interface electric fields affect the electronic properties of metallic interfaces and have a few monolayers penetration depth before vanishing by screening, when going in depth towards the bulk. Moreover, the ***E***-field control of the anisotropy provides enhanced energetic efficiency [2] for operating the spintronic devices. Extremely low energy consumption levels, of few fJ/bit [3,4] and sub-nanosecond switching times [5] have been already experimentally demonstrated.

Within these complex technological problematics, concerning the perpendicular magnetic anisotropy and its possibility to be manipulated, the basic understanding of the underlying physics represents a very important step. For describing the perpendicular magnetic anisotropy, often, more sophisticated *ab-initio* [6,7] and micromagnetic models are involved [8]. They underly electronic structure features responsible on the PMA: i.e., charge transfer and orbital population at the ferromagnetic metal/ insulator interface or interfacial Rashba field mechanisms illustrated by the bans structure analysis. On the other hand, the micromagnetic analysis incorporates other complex magnetic issues such as the magnetic anisotropy energy, its variation ratio with the electric field and magnetization damping phenomena. However, in this paper we illustrate that even a simple quantum model, based on a Stoner-Rashba Hamiltonian [9, 10] can be successfully used to depict major static and dynamic features related to the anatomy of the PMA in ultrathin films and its possibility to be toggled by external gating electric fields. The main results and predictions of this quantum analytical approach are in good qualitative agreement with the ones issued from more sophisticated DFT and micromagnetic calculations.

THEORETICAL MODEL, RESULTS AND DISCUSSION

In our paper, we develop a simple analytic quantum model based on the bi-dimensional Rashba contribution to the spin-orbit interaction and we show that this interaction is responsible on the perpendicular magnetic anisotropy. The magnetism (e.g., the exchange interaction) is introduced via a Stoner contribution to the Hamiltonian that competes with the Rashba spin-orbit fields. To build the Stoner-Rashba Hamiltonian, we add a Dirac spin orbit contribution that includes the spin-orbit effects to the band Stoner Hamiltonian. Therefore, in the total Hamiltonian (eq. 1) we easily recognize the kinetic free-electron contribution, the Stoner exchange, described in terms of an external molecular field J_0, and the Dirac spin orbit contribution containing the spin-orbit effects.

$$H_{SO} = \frac{\hat{p}^2}{2m} - J_0 \hat{m} \cdot \hat{\sigma} + \frac{\hbar}{2m_0 c^2} \vec{\nabla} V \cdot (\hat{\sigma} \times \hat{p}) \quad (1)$$

The third term describing the coupling between the electron spin and its orbital is deduced from the Dirac equation for a relativistic electron, expanded to the lowest order in $(v/c)^2$ (v and c are the electron and light velocities, respectively). A simple calculation (see Appendix 1) shows that for a central potential, the spin orbit contribution to the Hamiltonian describing the interaction between the carrier spin and the carrier momentum is proportional to the scalar product between the spin $\vec{S}$ and the orbital $\vec{L}$ angular moments (with λ being the spin-orbit interaction constant): $H_{SO} = \lambda \vec{L} \cdot \vec{S}$. This self-comprehensive expression for the SO-component in the Hamiltonian gives the name for the spin-orbit interaction.

In the Hamiltonian (1), *m* is the carrier (electron) mass, $\hbar$ the reduced Planck constant, $\hat{p} = \hbar \hat{k}$ is the momentum operator; the vector $\hat{m}$ is the magnetization $\vec{M}$ unit vector: $\hat{m} = \frac{\vec{M}}{M}$ with the components: $\hat{m}$ = (sinθ cosφ, sinθ sin φ, cos θ)- see figure 1 and $\hat{\sigma} = (\hat{\sigma}_x, \hat{\sigma}_y, \hat{\sigma}_z)$ is the operator of the Pauli spin matrices:

$$\hat{\sigma}_x = \begin{pmatrix} 0 & 1 \\ 1 & 0 \end{pmatrix}; \quad \hat{\sigma}_y = \begin{pmatrix} 0 & -i \\ i & 0 \end{pmatrix}; \qquad \hat{\sigma}_z = \begin{pmatrix} 1 & 0 \\ 0 & -1 \end{pmatrix};$$

related to the spin operator $\hat{S} = \frac{\hbar}{2}\hat{\sigma}$ and corresponding to the situation when the oz axis is the quantization axis for the magnetic field.

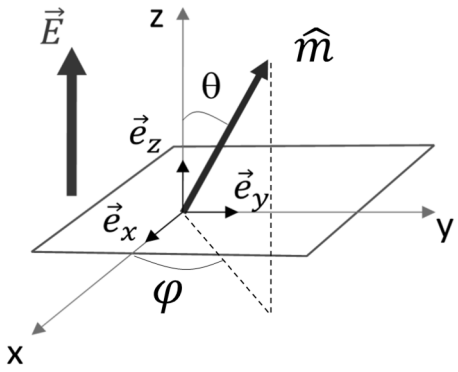

Figure 1

Geometry used in the analytical model, $\vec{e}_x$, $\vec{e}_y$, $\vec{e}_z$ are the unit vectors of ox, oy, oz axes. The electric field will be applied along the oz axis, perpendicular to the plane of the magnetic film.

The magnetic ultrathin film, having a thickness smaller than the mean free-electron path, can be reasonably assimilated to a two-dimensional electron gas (2DEG) in which the electrons are only moving within the xoy plane. Therefore, the electron wave vector will have only in-plane components $k_{II}=(k_x,k_y)$. Moreover, our model assumes that an electric field is applied perpendicular to this plane: $\vec{E} = (0,0,E_z)$. Later, we will reiterate that this field can be either an applied external field or an intrinsic electric field arising at the depletion zone when the ferromagnetic film is interfaced either with an insulator or with another metal (e.g., nonmagnetic) with different work-function or, the intrinsic field at the surface of the metallic film due to the symmetry breaking induced potential gradient. Within this model, considering the 2DEG with the confinement direction perpendicular to the propagation direction, we can calculate the vector product:

$$\hat{\sigma}\times\hat{p} = \begin{vmatrix} \hat{x} & \hat{y} & \hat{z} \\ \hat{\sigma}_x & \hat{\sigma}_y & \hat{\sigma}_z \\ p_x & p_y & p_z \end{vmatrix} \tag{2}$$

$$\hat{\sigma}\times\hat{p} = \hat{x}\left(p_z\hat{\sigma}_y - p_y\hat{\sigma}_z\right) - \hat{y}\left(p_z\hat{\sigma}_x - p_x\hat{\sigma}_z\right) + \hat{z}\left(p_y\hat{\sigma}_x - p_x\hat{\sigma}_y\right)$$

to find the expression of the Dirac third term in equation (1) within the hypothesis of our 2DEG model.

If the electric field $\vec{E} = -\nabla V$ is applied along the oz axis, perpendicular to the 2DEG plane, we have:

$$\vec{\nabla}V\cdot\left(\hat{\sigma}\times\hat{p}\right) = -\frac{\partial V}{\partial z}\left(\hat{p}_x\hat{\sigma}_y - \hat{p}_y\hat{\sigma}_x\right) \tag{3}$$

This would lead to the Stoner-Rashba Hamiltonian, which is the particular case of the Stoner-Dirac Hamiltonian in case of a 2DEG with an electric field applied perpendicular to the electron mobility plane:

$$\widehat{H} = \frac{\hat{p}^2}{2m} - J_0\hat{m}\cdot\hat{\sigma} + \frac{\alpha_R}{\hbar}\left(\hat{\sigma}_x\hat{p}_y - \hat{\sigma}_y\hat{p}_x\right) = \frac{\hbar^2\hat{k}^2}{2m} - J_0\hat{m}\cdot\hat{\sigma} + \alpha_R\left(\hat{\sigma}_x\hat{k}_y - \hat{\sigma}_y\hat{k}_x\right) \quad (4)$$

with $\alpha_R = \frac{\hbar^2}{2m_0c^2}\frac{\partial V}{\partial z}$ defining the Rashba coefficient. Because the electric field in our model has only a z component, we have: $\vec{E} = (0,0,E_z) \Longrightarrow \overrightarrow{\nabla V} = \frac{\partial V}{\partial z}\vec{e}_z$, which states that the Rashba coefficient is proportional with the z (perpendicular) component of the electric field.

This approach leads to the following immediate conclusions: (i) the larger is the electric-field felt by the electron, the larger is the SO-coupling; (ii) in case of an atom, the ***E***-field is proportional to the atomic number Z (***E***~Ze); this explains why the SO-coupling is larger for heavy atoms: Au (Z=79), Pt (Z=78), Pd (Z=46) than for 3d atoms: Cr (Z=24), Fe (Z=26),Co (Z=27), Ni (Z=28); (iii) the SO-coupling is exacerbated at the metal surfaces: i.e, the breaking of the translational symmetry in surface is equivalent to a potential gradient felt by the electron => electric field; (iv) in case when a metal-insulator (or metal semiconductor) interface is created in a multilayer heterostructure, a depletion zone appears with corresponding significant interfacial intrinsic electric field.

1. Stationary solution: eigenstates and eigenvalues

Within the Heisenberg-Dirac formalism, we solve the stationary Schrodinger equation by diagonalizing the spin-orbit Hamiltonian and find the eigenvalues and the stationary eigenfunctions.

The $\hat{k}_x$ and $\hat{k}_y$ wave vector operators commute with $\widehat{H}$, then the eigenfunctions of the system are:

$$\left|\Psi\right\rangle = e^{i(k_x x + k_y y)}\left(C_1\left|+\right\rangle + C_2\left|-\right\rangle\right) = e^{i\vec{k}_{\parallel}\vec{r}}\left(C_1\left|+\right\rangle + C_2\left|-\right\rangle\right) \quad (5)$$

The $\{|+\rangle, |-\rangle\}$ wave functions represent the up (UP) and down (DN) electron states of the *z* component of the spin (S_z), they are orthonormal and form

a basis. We remember that, in our model, the *z* direction in the electron referential is chosen to be the quantization direction of the effective magnetic field $\mathbf{B}_{\text{eff.}}$ leading to a diagonal $\hat{\sigma}_z$.

The eigenvalues are issued from diagonalizing the Hamiltonian matrix (See Appendix 2) whose components are calculated within the $\{|+\rangle, |-\rangle\}$ basis. After solving the eigenvalues problem within the Heisenberg matrix formalism, we get:

$$\varepsilon_{\pm} = \frac{\hbar^2 k^2}{2m} \mp \sqrt{J_0^2 + 2J_0 \alpha_R k_x \sin\theta + \alpha_R^2 k^2} \tag{6}$$

$$\text{or,} \quad \varepsilon_{\sigma} = \frac{\hbar^2 k^2}{2m} - \sigma J_0 \sqrt{1 + \frac{2\alpha_R k_x}{J_0} \sin\theta + \frac{\alpha_R^2 k^2}{J_0^2}}; \quad \sigma = \pm 1 \,(\text{UP, DN}) \tag{7}$$

A development in $\alpha k/J_0 \ll 1$ (that would correspond to the common experimental situation when the Rashba interaction is much smaller than Stoner interaction) leads to:

$$\varepsilon_{\sigma}(k) = \frac{\hbar^2 k^2}{2m} - \sigma J_0 \left(1 + \frac{1}{2}\frac{\alpha_R^2 k^2}{J_0^2}\right) - \sigma J_0 \frac{\alpha_R k_x}{J_0} \sin\theta + \frac{1}{2}\sigma J_0 \frac{\alpha_R^2 k_x^2}{J_0^2} \sin^2\theta \tag{8}$$

In this equation we identify the following contributions:

(1) the first kinetic term, corresponding to the free electron 2DEG with parabolic dispersion bands.
(2) the second term represents the Rashba correction to the Stoner splitting. The proportionality with α_R indicates a quadratic dependence of this contribution to the total energy with respect to the electric field.
(3) the third term represents pseudo-dipolar contribution to the anisotropy energy. It favors the in-plane magnetization (minimum when $\theta = \pi/2$). Because α_R depends linearly on the electric field, the in-plane pseudo-dipolar contribution to the anisotropy will depend linearly on the electric field.
(4) the fourth term corresponds to a uniaxial-like anisotropy. One can see that it favors the perpendicular to the film plane magnetization (energy minimum when $\theta = 0$). Following the square dependence in α_R, one can deduce that the pure Rashba mechanism induces a quadratic dependence of the uniaxial PMA with the electric field.

The eigenvalues dispersion described by the equation (8) can be depicted by the band diagrams $\varepsilon = \varepsilon_{\sigma}(k)$, schematically illustrated for both nonmagnetic (Fig. 2(a)) or magnetic case (Fig. 2(b)).

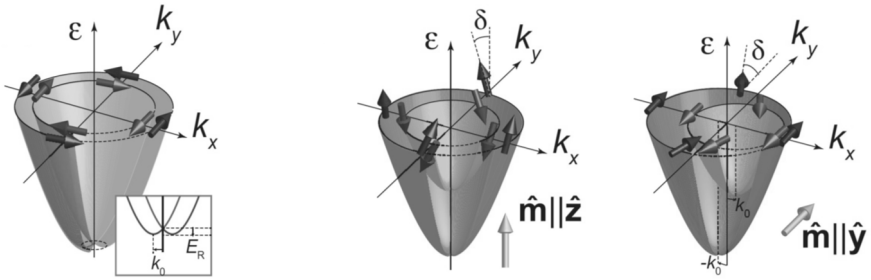

Figure 2. Band diagrams $\varepsilon = \varepsilon_\sigma(k)$ corresponding to a (a) nonmagnetic case (b) magnetic case, as issued from diagonalizing the Stoner-Rashba Hamiltonian -image adapted from [10]. From eq. (6) the dispersion relations in the nonmagnetic case are: $\varepsilon_\pm = \frac{\hbar^2 k^2}{2m} \mp \alpha_R k$, the magnetic case being described by eq. (8).

We can further proceed with a geometric analysis of our result, as illustrated in the Figure 3. We introduce the following contributions to the total (effective) magnetic field: (1) the Stoner field $\vec{B}_0 = \frac{2J_0}{g\mu_B}\vec{m}$ and (2) the Rashba field $\vec{B}_R \propto -\vec{k} \times \vec{E} = -\frac{2\alpha_R}{g\mu_B}\left(\vec{k} \times \vec{e}_z\right)$ that is perpendicular to the vectors ***k*** and ***E***; i.e. the Rashba field lies in (xoy) plane, and is perpendicular to the (**k**o**E**) plane.

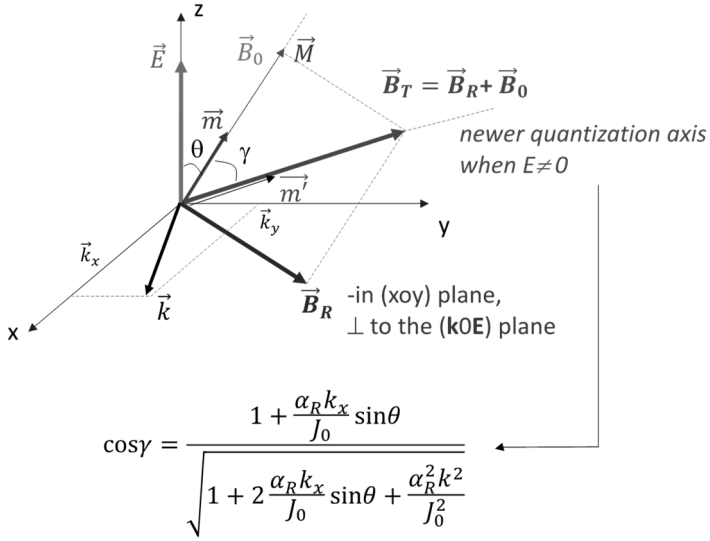

Figure 3. Geometric representation of the Stoner, Rashba and the effective field $\mathbf{B_T}$ whose new quantization direction is defined by the angle γ.

Then, the total (effective) magnetic field $\vec{B}_T = \vec{B}_R + \vec{B}_0$ will write:

$$\vec{B}_T = \vec{B}_0 \left[-\frac{\alpha_R k_y}{J_0} \vec{e}_x + \left(sin\theta + \frac{\alpha_R k_x}{J_0} \right) \vec{e}_y + \cos\theta \vec{e}_z \right] = \vec{B}_0 \overrightarrow{m'} \qquad (9)$$

In this equation, the $\overrightarrow{m'}$ will define the new direction of quantization direction corresponding to the case when an electric field is applied. It is issued from the competition between the Rashba field $\vec{B}_R$, perpendicular to ***E*** and **k,** and the exchange field $\vec{B}_0$. The magnetization dynamics related to the new direction of quantization direction generates the second order in ***E*** contribution to the anisotropy (last term in eq. 8) and is identified as a Dzyalozinskii-Moryia (DMI) interaction mechanism [11].

A partial conclusion can be driven in this point about the main result of the static eigenvalue analysis: the Rashba spin-orbit interaction is responsible on a uniaxial-anisotropy energy. That, within the Dzyaloshinskii-Moriya approach [11], includes a second order in electric field ***E*** in plane pseudo-dipolar interaction and another contribution proportional to $\boldsymbol{E^2/J_0 S}$, issued from the competition between the first order in ***E*** Rashba-Dzyaloshinskii-Moriya and the exchange fields. An effective $\boldsymbol{E^2}$ dependent perpendicular magnetic anisotropy may result in the situation when the Rashba-Dzyaloshinskii-Moriya term overcome the pseudo-dipolar ***E*** dependent one. Therefore, our simple Stoner-Rashba model, developed in the simplified case of quadratic free-electron dispersion framework, clearly indicates the interplay between the two terms in stabilizing the perpendicular magnetic anisotropy. We mention that the validity of results issued from this simplified free-electron approach has been further validated by band structure calculations [6] describing more accurately the localization of the wave-functions of 3d magnetic materials.

2. Rashba induced magnetization precession

From the static analysis, geometrically depicted in Figure 3, we saw that if initially (when ***E***=0) the magnetization quantization axis is $\vec{m}$, when the electric field ***E*** is switched on, due to the additional Rashba field $\mathbf{B_R}$, the newer quantization axis becomes $\overrightarrow{m'}$. Consequently, when the electric field is applied, the spin magnetization, initially aligned along the Stoner field $\mathbf{B_0}$ will not be any more in a stationary state, and a time evolution is expected. Using quantum mechanics time evolution analysis, we demonstrate and quantify that the magnetization will preces around the new quantization axis $\overrightarrow{m'}$.

We focus our analysis on a simplified situation, analytical easier to be calculated, when we fix the initial condition with the magnetization parallel to oz (plane of the 2DEG); m||oz (θ=0) that is the case of a sample with PMA.

Then, we calculate **the eigenvectors** corresponding to the $\varepsilon_{\pm}$ eigenvalues, the stationary solutions being (See Appendix 2):

$$|\Psi_{\varepsilon+}\rangle = e^{i\vec{k}\cdot\vec{r}}\left(\cos\frac{\gamma}{2}e^{\frac{i\varphi}{2}}|+\rangle - \sin\frac{\gamma}{2}e^{\frac{-i\varphi}{2}}|-\rangle\right)$$
$$|\Psi_{\varepsilon-}\rangle = e^{i\vec{k}\cdot\vec{r}}\left(\sin\frac{\gamma}{2}e^{\frac{i\varphi}{2}}|+\rangle + \cos\frac{\gamma}{2}e^{\frac{-i\varphi}{2}}|-\rangle\right) \quad (10)$$

The Hamiltonian being not explicitly dependent on time, the time dependence of the wave functions is simply introduced via some phase terms:

$$|\Psi(t)\rangle = C_+(0)e^{-\frac{i}{\hbar}\varepsilon_+ t}|\Psi_{\varepsilon+}\rangle + C_-(0)e^{-\frac{i}{\hbar}\varepsilon_- t}|\Psi_{\varepsilon-}\rangle \qquad \varepsilon_{\pm} = \frac{\hbar^2k^2}{2m} \mp \sqrt{J_0^2 + \alpha_R^2k^2}$$
$$C_+(t) = C_+(0)e^{-\frac{i}{\hbar}\varepsilon_+ t} \quad ; \quad (11)$$
$$C_-(t) = C_-(0)e^{-\frac{i}{\hbar}\varepsilon_- t}$$

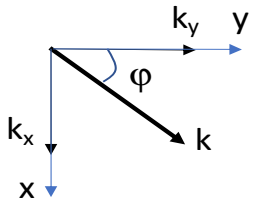

Figure 4

In-plane wave-vector of an electron in a 2DEG.

These time-dependent wave vectors are further used to calculate the average (expectation) value of the spin operators: $\langle\hat{S}_x\rangle$, $\langle\hat{S}_y\rangle$, $\langle\hat{S}_z\rangle$.

Within the Dirac formalism, the average (expectation) value of an operator is:

$$\langle A\rangle = \langle\Psi(t)|\boldsymbol{A}|\Psi(t)\rangle \quad (12)$$

With the *bra* and *ket* wave-vectors written as:

$$|\Psi(t)\rangle = \begin{pmatrix} C_+(t) \\ C_-(t) \end{pmatrix}; \quad \langle\Psi(t)| = (C_+^*(t) \quad C_-^*(t)) \quad (13)$$

Therefore, the average values will be:

$$\widehat{\langle S_x\rangle} = \hbar\Re e[C_+^*(t)C_-(t)]$$
$$\widehat{\langle S_y\rangle} = \hbar\Im m[C_+^*(t)C_-(t)] \quad (14)$$
$$\widehat{\langle S_z\rangle} = \frac{\hbar}{2}[C_+^*(t)C_+(t) - C_-^*(t)C_-(t)]$$

If initially, in a most general case the magnetization would make an angle δ with respect to ***m'*** (see Figure 5), we can write: $C_+(0) = \cos\frac{\delta}{2}; C_-(0) = \sin\frac{\delta}{2}$. When $\delta = -\gamma$ we find back the situation when, initially, **m**||oz.

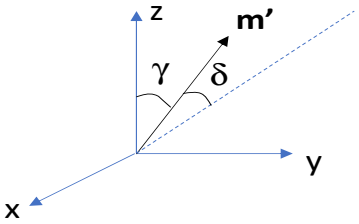

Figure 5

Initial geometry for the time-dependent analysis.

The calculations of the average values, after some simple math, leads to:

$$\begin{cases} \langle \hat{S}_x \rangle = \frac{\hbar}{2}\left[\cos^2\frac{\gamma}{2}\cos\left(\frac{2Jt}{\hbar}+\varphi\right) - \sin^2\frac{\gamma}{2}\cos\left(\frac{2Jt}{\hbar}-\varphi\right)\right] \\ \langle \hat{S}_y \rangle = -\frac{\hbar}{2}\left[cos^2\frac{\gamma}{2}sin\left(\frac{2Jt}{\hbar}+\varphi\right) + sin^2\frac{\gamma}{2}sin\left(\frac{2Jt}{\hbar}-\varphi\right)\right] \\ \langle \hat{S}_z \rangle = \frac{\hbar}{2}\left[\sin\gamma\cos\left(\frac{2Jt}{\hbar}\right)\right] \end{cases} \quad (15)$$

These set of three equations (15) describes the spin precession (and therefore the magnetization precession) around the ***m'*** direction, that is the quantization direction of the effective (total field, Rashba + Stoner): $\vec{\boldsymbol{B}}_{\boldsymbol{T}} = \vec{\boldsymbol{B}}_{\boldsymbol{R}} + \vec{\boldsymbol{B}}_{\boldsymbol{0}}$ described by a total **(**effective) molecular field:

$$J = J_{eff} = \sqrt{J_0^2 + \alpha^2 k^2} \quad (16)$$

The corresponding angular frequency (Larmor) for the precession will be:

$$\Omega = \frac{2J}{\hbar} = \frac{2\sqrt{J_0^2+\alpha^2k^2}}{\hbar} \quad (17)$$

Geometrically, this magnetization precession around the molecular total (effective) field is illustrated in Figure 6. One can see that the magnetization will preces with an angle equal to π (that would correspond to a toggle-like switch or reversal) if we apply a pulse of electric field with a time length equal to half of the Larmor period $t_{1/2} = \frac{T}{2} = \frac{\pi\hbar}{2\sqrt{J_0^2+\alpha^2k^2}}$. Therefore, under a pulse of perpendicular electric field applied to a magnetic 2D electron gas (that mimics an ultrathin magnetic film), we have a magnetization dynamic, similarly to a Nuclear Magnetic Resonance (NMR) experiment. Here, the ***E***-field, via the related Rashba magnetic field $\mathbf{B_R}$, plays the role of the radiofrequency (RF) in-plane magnetic field in NMR experiments.

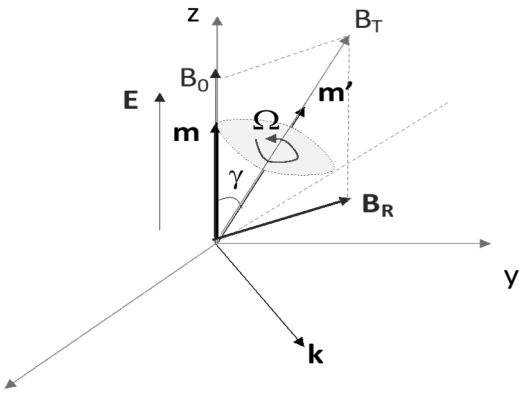

Figure 6

Magnetization precession around the molecular total field whose quantization direction is defined by ***m***'.

Our result indicates that NMR-like experiments can be successfully performed. Using pulses of laser, polarized with a component perpendicular to the film surface, the magnetization can be precesionally switched. However, more dedicated, and realistic experiments for the electric field toggling of the magnetization are commonly performed in lithographically patterned spintronic devices where a gating insulator is used for applying the field [12] or via the tunnel barrier in a magnetic tunnel junction) [13].

We can further add the following concluding remarks. The spin precession in external electric field is related to the spin-orbit interaction in the 2DEG (Rashba effect). The origin of this interaction is relativistic and has been addressed here using a "non-relativistic" Dirac Hamiltonian, deduced from the Dirac equation for a relativistic electron expanded to the lowest order in $(v/c)^2$. Note that even a classical relativistic *gedanken* analysis can phenomenologically explain the precession of a spin induced by an applied electric field. Therefore. an electron, moving with the velocity $\vec{v}$ in an external field $\vec{E}$, would "feel" in its own referential an effective magnetic field perpendicular on the direction of motion: $\vec{B} = -\frac{\vec{v}\times\vec{E}}{c^2}$. This magnetic field (i.e., Rashba field in our case) will lead to the spin Larmor precession.

Finally, we reiterate the important fact that the electric field used in our model can be either an external applied field, or, in realistic thin film heterostructures, an intrinsic electric field at the interface between a ferromagnetic ultrathin film and an insulator or a nonmagnetic metal with different workfunctions, or at the surface of the film due to the potential gradient related to the symmetry breaking. Independent of his origin, the existence of this electric field is responsible in ultrathin magnetic films on the perpendicular magnetic anisotropy [7]. We underline the fact that, in case of a surface or interface intrinsic electric field in multi-layered heterostructures, this field can be further modified by applying an external electric field. Moreover, as a function of the orientation of the external electric field, the intrinsic ***E***-field can be increased or decreased. Having in view the PMA dependence on the net electric

field felt by the 2DEG electrons, this would explain the possibility of controlling the anisotropy magnitude by the electric field (increase/decrease). In the literature, because the electric field is often generated by a biasing voltage, this phenomenon is called Voltage-Controlled-Magnetic-Anisotropy (VCMA) [14].

Beyond this simple quantum description, a more accurate study of the magnetization dynamics can be further performed within the Landau-Lifshitz-Gilbert (LLG) equation approach. That would consider the anisotropy energies, their dependence with respect to the electric field (that would affect the magnetic free-energy landscape), the phenomenological Gilbert damping contribution to the magnetization dynamics [8] and, beyond the macrospin approach, the micromagnetic features of ***E***-field toggling experiments in realistic patterned nanopillars based on ultrathin magnetic films.

CONCLUSIONS

Based on a Stoner-Rashba Hamiltonian approach, we underlined important static and dynamic issues related to the origin of the perpendicular magnetic anisotropy in ultrathin magnetic films, modelled as 2DEG magnetic systems. First, the static eigenvalue and eigenvector analysis show that the Rashba spin-orbit interaction leads to a uniaxial-anisotropy energy with a Stoner splitting, an in-plane pseudo-dipolar (proportional to the electric field **E**) and an out-of-plane ($\mathbf{E}^2$ dependent) competing contributions. Therefore, an effective perpendicular magnetic anisotropy may result when the Rashba-Dzyaloshinskii-Moriya term overcome the pseudo-dipolar one. Second, the time dependent analysis performed in case of the time-independent Stoner-Rashba Hamiltonian, illustrate that when an electric field is applied perpendicularly to the surface of the magnetic ultrathin film, the magnetization will preces around a new quantization axis corresponding to a net magnetic field resulting from vector sum of the initial Stoner field and the ***E***-field induced Rashba field. If the time length of a pulse of an applied electric field is equal to half of the Larmor precession period, magnetization toggling experiments NMR-like can be performed. Our results have been qualitatively confirmed and validated by more complex ab-initio and micromagnetic simulations that include more complex aspects.

ACKNOWLEDGEMENTS

C.T. acknowledges funding from the project «MODESKY» ID PN-III-P4-ID-PCE-2020-0230, No. UEFISCDI: PCE 245/02.11.2021. Moreover, the implementation of the current research further confirms and sustains the durability of previous funding projects: «SPINTRONIC» POS CCE Project: ID. 574, cod SMIS-CSNR 12467, «SPINTAIL» ID PN-II-PCE-2012-4-0315, No. UEFISCDI:23/29.08.2013 and «EMERSPIN» ID PN-III-P4-ID-PCE-2016-0143, No. UEFISCDI:22/12.07.2017.

APPENDIX 1:
THE SPIN-ORBIT HAMILTONIAN FOR A CENTRAL (SPHERICAL) POTENTIAL

The spin-orbit Dirac term that considers the spin-orbit interaction is obtained from the Dirac equation for a relativistic electron, expanded to the lowest order in $(v/c)^2$. Therefore, the non-relativistic Dirac Hamiltonian is:

$$H_{SO} = \frac{\hbar}{2m_0c^2}\vec{\nabla}V \cdot (\hat{\sigma} \times \hat{p})$$

Using some circular rules for the mixed vector product:

$$\vec{a} \cdot \left(\vec{b} \times \vec{c}\right) = \vec{b} \cdot (\vec{c} \times \vec{a}) = -\vec{b} \cdot (\vec{a} \times \vec{c})$$

we can rewrite:

$$H_{SO} = -\frac{\hbar}{2m_0c^2}\hat{\sigma} \cdot \left(\vec{\nabla}V \times \hat{p}\right) = -\frac{\hbar}{2m_0c^2}\left(\vec{\nabla}V \times \hat{p}\right) \cdot \hat{\sigma}$$

Moreover, for a spherical symmetry, the gradient *nabla* $\vec{\nabla}$ operator can be written in spherical coordinates as.

$$\vec{\nabla} = \frac{\partial}{\partial r}\hat{r} + \frac{1}{r}\frac{\partial}{\partial \theta}\hat{\theta} + \frac{1}{r\sin\theta}\frac{\partial}{\partial \varphi}\hat{\varphi}$$

In case of a central potential *V* having a spherical symmetry, *V* will only depend on *r* being independent on θ and φ. Thus, in this case:

$$\vec{\nabla}V = \frac{\partial V}{\partial r}\hat{r} = \frac{\partial V}{\partial r}\frac{\vec{r}}{r} = \frac{1}{r}\frac{\partial V}{\partial r}\vec{r}$$

This will lead to: $H_{SO} = -\frac{\hbar}{2m_0c^2}\frac{1}{r}\frac{\partial V}{\partial r}(\vec{r} \times \hat{p}) \cdot \hat{\sigma}$

In this equation, we recognize the orbital moment of the electron: $\vec{L} = \vec{r} \times \hat{p}$ whereas the Pauli spin operator $\hat{\sigma}$ is related to the spin momentum operator via $\hat{S} = \frac{\hbar}{2}\hat{\sigma}$. Within these circumstances:

$$H_{SO} = \lambda\vec{L} \cdot \vec{S}$$

with $\lambda = -\frac{1}{m_0c^2}\frac{1}{r}\frac{\partial V}{\partial r}$ the spin-orbit constant, proportional to the gradient of the potential (electric field). One can easily correlate the spin-orbit to λ coefficient and the Rashba constant $\alpha_R = \frac{\hbar^2}{2m_0c^2}\frac{\partial V}{\partial z}$, deduced in case of a non-spherical potential varying along the z direction perpendicular to the surface of a 2DEG. Beyond some constants, the most important common feature is their similar dependence on the potential gradient, so on the electric field.

APPENDIX 2:
THE STONER-RASHBA HAMILTONIAN MATRIX: EIGENVALUES AND STATIONARY EIGENVECTORS

The Stoner-Rashba Hamiltonian is:

$$\hat{H} = \frac{\hat{p}^2}{2m} - J_0 \hat{m} \cdot \hat{\sigma} + \frac{\alpha_R}{\hbar}\left(\hat{\sigma}_x \hat{p}_y - \hat{\sigma}_y \hat{p}_x\right) = \frac{\hbar^2 \hat{k}^2}{2m} - J_0 \hat{m} \cdot \hat{\sigma} + \alpha_R\left(\hat{\sigma}_x \hat{k}_y - \hat{\sigma}_y \hat{k}_x\right)$$

and the Pauli matrices:

$$\hat{\sigma}_x = \begin{pmatrix} 0 & 1 \\ 1 & 0 \end{pmatrix}; \qquad \hat{\sigma}_y = \begin{pmatrix} 0 & -i \\ i & 0 \end{pmatrix}; \qquad \hat{\sigma}_z = \begin{pmatrix} 1 & 0 \\ 0 & -1 \end{pmatrix};$$

With $\{|i\rangle, |j\rangle\}$ belonging to the $\{|+\rangle, |-\rangle\}$ orthonormal basis $\langle i|j\rangle = \delta_{ij}$ (Kronecker *delta* symbol), one can calculate the matrix elements of the Hamiltonian $\hat{H}$:

$$\hat{H}_{ij} = \langle i|\hat{H}|j\rangle$$

For the free particle kinetic (first term) we get the diagonal Hamiltonian:

$$\hat{H}_{FP} = \begin{pmatrix} \dfrac{\hbar^2 \hat{k}^2}{2m} & 0 \\ 0 & \dfrac{\hbar^2 \hat{k}^2}{2m} \end{pmatrix}$$

For the Stoner term, we explicit the scalar product:

$$\vec{m} \cdot \hat{\sigma} = m_x \sigma_x + m_y \sigma_y + m_z \sigma_z = \sin\theta\, \sigma_y + \cos\theta\, \sigma_z,$$

in case when we consider a simplified configuration when $\varphi = \pi/2$ (Figure 1), so that $\hat{m}$ = (0, sinθ, cos θ)

Then, we get the explicit form for the Stoner term:

$$\hat{H}_S = -J_0\left(\sin\theta\, \sigma_y + \cos\theta\, \sigma_z\right)$$

Introducing the Pauli matrices, we get a Stoner Hamiltonian.

$$\hat{H}_S = -J_0 \begin{pmatrix} \cos\theta & -i\sin\theta \\ i\sin\theta & -\cos\theta \end{pmatrix}$$

Note that the Stoner Hamiltonian matrix is non-diagonal because the chosen magnetization direction θ does not correspond to the z quantization axis, initially considered for the definition of the Pauli matrices.

For the Rashba term $\hat{H}_R = \alpha_R\left(\hat{\sigma}_x \hat{k}_y - \hat{\sigma}_y \hat{k}_x\right)$ the matrix elements can be calculated by explicitly introducing the Pauli matrices definition:

$$\hat{H}_R = \alpha_R \begin{pmatrix} 0 & \hat{k}_y + i\hat{k}_x \\ \hat{k}_y - i\hat{k}_x & 0 \end{pmatrix}$$

Adding all the contributions, one finds that the matrix of the total Hamiltonian is:

$$\hat{H}_T = \begin{pmatrix} \frac{\hbar^2\hat{k}^2}{2m} - J_0\cos\theta & iJ_0\sin\theta + \alpha_R(\hat{k}_y + i\hat{k}_x) \\ -iJ_0\sin\theta + \alpha_R(\hat{k}_y - i\hat{k}_x) & \frac{\hbar^2\hat{k}^2}{2m} + J_0\cos\theta \end{pmatrix}$$

One can observe that the Hamiltonian matrix is non-diagonal, therefore the $|+\rangle$ and $|-\rangle$ states are not eigenstates of the Hamiltonian (system).

The eigenvalues can be calculated by solving the linear algebra eigenvalues equation:

$$\det(\hat{H}_T - \lambda\hat{I}) = 0$$

where $\hat{I} = \begin{pmatrix} 1 & 0 \\ 0 & 1 \end{pmatrix}$ is the unit 2×2 matrix.

Some elementary algebra leads to:

$$\lambda_{1,2} = \varepsilon_{\pm} = \frac{\hbar^2 k^2}{2m} \mp \sqrt{J_0^2 + 2J_0\alpha_R k_x \sin\theta + \alpha_R^2 k^2}\,;$$

with $\sigma = \pm 1$ (up, dn) and $k = (k_x, k_y, 0)$.

The eigenvectors corresponding to these eigenvalues are calculated from the linear algebra equation:

$$(\hat{H}_T - \lambda\hat{I})\begin{pmatrix} u \\ v \end{pmatrix} = 0$$

with $\lambda_{1,2} = \varepsilon_{\pm}$.

Some elementary algebra leads to the stationary eigenvectors:

$$|\Psi_{\varepsilon+}\rangle = e^{i\vec{k}\cdot\vec{r}}\left(\cos\frac{\gamma}{2}e^{\frac{i\varphi}{2}}|+\rangle - \sin\frac{\gamma}{2}e^{\frac{-i\varphi}{2}}|-\rangle\right)$$

$$|\Psi_{\varepsilon-}\rangle = e^{i\vec{k}\cdot\vec{r}}\left(\sin\frac{\gamma}{2}e^{\frac{i\varphi}{2}}|+\rangle + \cos\frac{\gamma}{2}e^{\frac{-i\varphi}{2}}|-\rangle\right)$$

The phase factor φ is related to the in-plane orientation of the wave vector k.

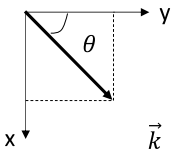

$$k_y = k\cos\varphi \qquad k_x + ik_y = e^{i\varphi}k$$
$$k_y = k\sin\varphi \qquad k_x - ik_y = e^{i\varphi}k$$

Figure A2.1 Geometrical interpretation of the phase factor φ

REFERENCES

1. B. Dieny, M. Chshiev, *Rev. of Mod. Phys.,* vol. 89, (2017).
2. D. C. M. Yamanouchi, F. Matsukura, H. Ohno, *Science*, 301, 943-945 (2003).
3. S. Kanai, F. Matsukura, H. Ohno, *Appl. Phys. Lett.*, 108, 192406 (2016).
4. C. Grezes, F. Ebrahimi , J. G. Alzate, X. Cai, J. A. Katine , J. Langer, B. Ocker , P. Khalili Amiri, K. L. Wang, *Appl. Phys. Lett.,* 108, 012403 (2016).
5. E. G. V. Krizakova, G. Sala, F. Yasin , S. Couet, G. S. Kar, K. Garello, P. Gambardella, *Nature Nanotechnology*, 15, 111 (2020).
6. R-A. One, S. Mican, C. Tiusan, *Stud. Univ. Babeș- Bolyai Phys*. 66, 91–110 (2021).
7. F. Ibrahim, H. Yang, A. Halla, M. Chshiev, *Phys. Rev. B*, 93, 014429 (2016).
8. R-A. One, H. Béa, S. Mican, M. Joldos, P. Brandão Veiga, B. Dieny, L. D. Buda-Prejbeanu & C. Tiusan, *Sci Rep* 11, 8801 (2021).
9. A. Manchon, S. Zhang, *Phys. Rev. B* 79, 094422 (2009).
10. S. E. Barnes, J. Ieda, S. Maekawa, *Sci. Rep.*, 4, 4105 (2015).
11. I. E. A. Dzyaloshinskii, *J. Chem. Solids* 4, 241–255 (1958); T. Moriya, *Phys. Rev.* 120, 91–98 (1960); T. Moriya, *Phys. Rev. Lett.* 4, 228–230 (1960).
12. R-A One, S Mican, A Mesaros, M Gabor, T Petrisor, M Joldos, LD Buda-Prejbeanu, C Tiusan, *IEEE Trans. on Magn.* 57(6), (2021).
13. S. Kanai, F. Matsukura, & H. Ohno, , *Appl. Phys. Lett.* 108, 192406 (2016).
14. J. Zhang, P. V. Lukasev, S. S. Jaswal, & E. Y. Tsymbal, *Phys. Rev. B* 96, 014435 (2017).

STUDIA UBB PHYSICA, Vol. 67 (LXVII), 1-2, 2022, pp. 107-118
(RECOMMENDED CITATION)
doi:10.24193/subbphys.2022.09

VIBRATIONAL FEATURES OF DIPHENYLHYDANTOIN

R. LUCHIAN[1], Z. BORSAY[1], D. MANIU[1], N. LEOPOLD[1], V. CHIŞ[1*]

ABSTRACT. The molecular vibrations of diphenylhydantoin (DPH) were investigated in crystalline sample at room temperature, by using Fourier transform infrared (FT-IR), FT- and conventional Raman spectroscopies. Furthermore, density functional theory (DFT) calculations were utilized to confirm and clarify the experimental data. Two methods were evaluated for accurate prediction of the vibrational spectra: i) vibrational anharmonic calculations on DPH monomer based on the second-order perturbation theory; ii) harmonic calculations on a cluster of five DPH molecules.

Keywords*: Diphenylhydantoin, FT-IR, Raman, DFT, anharmonic, cluster model.*

1. INTRODUCTION

Diphenylhydantoin (DPH - IUPAC name 5,5-diphenylimidazolidine-2,4-dione) (see Fig. 1), is a sodium channel protein inhibitor and one of the most used drug indicated for the treatment of epilepsy [1,2]. It acts on sodium channels on the neuronal cell membrane, dampening the unwanted brain activity seen in seizure, by reducing electrical conductance among brain cells. This molecule is also an effective drug used for the treatment of arrhythmias.

For monitoring the excretion of the drug and its metabolites [3] by vibrational techniques, a precise description of its normal modes is mandatory. For this reason, here we report a detailed investigation on the vibrational features of

[1] *Babeş-Bolyai University, Faculty of Physics, 1 Kogălniceanu str., Cluj-Napoca, Romania*
* *Corresponding author: vasile.chis@ubbcluj.ro*

this molecule. A second objective was to compare two different techniques used for the assignment of vibrational IR and Raman spectra (anharmonic and cluster model calculations) [4]. The present study complete the spectroscopical data reported earlier by some of us [5].

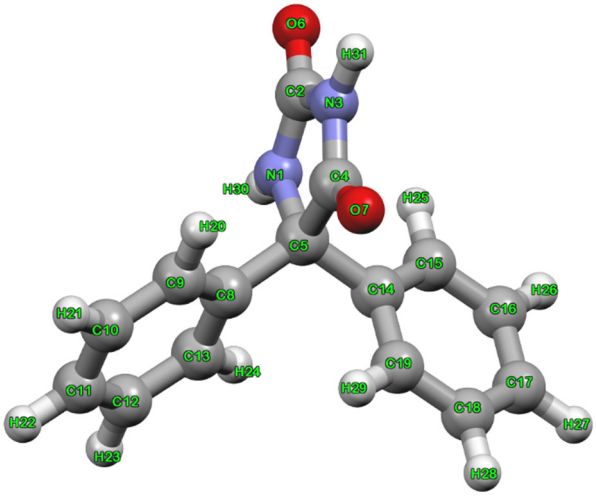

Fig. 1. Geometric structure of the most stable conformer DHP optimized in gas-phase at B3LYP/6-31G+(2d,2p) level of theory, with the atom numbering and labels.

2. EXPERIMENTAL DETAILS

DPH of 99 % purity was purchased from a standard commercial source (Alfa Aesar) and used without further purification.

FT-IR spectra for of DPH powder sample were recorded at room temperature on a conventional Equinox 55 FT-IR spectrometer equipped with an InGaAs detector and by using KBr (Merck UVASOL) tablet samples. IR spectra were recorded with a resolution of 2 cm^{-1} by co-adding 40 scans.

The FT-Raman spectra were recorded in a backscattering geometry with a Bruker FRA 106/S Raman accessory with nitrogen cooled Ge detector. The 1064-nm Nd:YAG laser was used as excitation source and the laser power was set to 350 mW and the spectra were recorded with a resolution of 2 cm^{-1} by co-adding 200 scans.

The conventional Raman spectra of DPH powder were recorded at room temperature using a Renishaw inVia Reflex Raman spectrometer equipped with a RenCam CCD detector. The 325 nm, 532 nm, 633 nm and 785 nm laser excitation lines were used in this study.

3. COMPUTATIONAL DETAILS

The optimization of DPH geometry and calculations of normal modes were performed with the Gaussian16 software package [6] by using DFT approaches. The hybrid B3LYP [7-10] and APFD [11] exchange-correlation functionals were used in conjunction with the Pople's type split-valence 6-311+G(2d,p) basis set [12]. To compute the vibrational spectra of DPH we used a cluster model comprising five molecules, able to capture the hydrogen bonding interactions taking place in solid state. For this model we employed the ONIOM QM:QM approach, treating the relaxed molecule and the four neighboring molecules at B3LYP/6-311+G(2d,p) and B3LYP/3-21G level of theory, respectively (see Fig. 2). Moreover, for the monomer model we tested the performance of the anharmonic approximation for reproducing the Raman spectrum of DPH, the calculations being performed at APDF/6-311+G(2d,p) level of theory, in gas-phase [4].

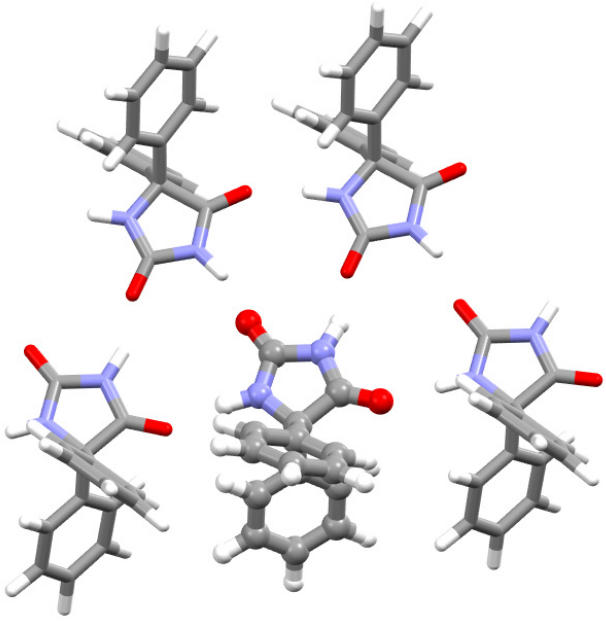

Fig. 2. Cluster model of DPH optimized at the ONIOM(B3LYP/6-311+G(2d,p): B3LYP/3-21G)) level of theory (central molecule – ball and stick model, neighboring molecules – stick model).

The mode assignments were aided by direct comparison between experimental and calculated spectra and by comparisons with vibrational spectra of similar compounds like hydantoin [13-17] and phenyl radical [18].

4. RESULTS AND DISCUSSIONS

The normal modes of DPH have been previously investigated by using IR [19] and Raman [20] techniques. For a reliable assignment of the Raman spectrum of DPH, in this study we based on the comparison with the Raman spectrum of 2,4-imidazolidinedione [15], as well as on the DFT calculated Raman spectrum of a cluster composed of 5 DPH molecules and on the calculated anharmonic spectrum of the DPH monomer in gas-phase.

In Fig. 3 and Fig. 4 are given the experimental FT-IR and Raman spectra, and in Table 1 are listed the experimental and calculated normal modes along with their IR and Raman intensities. The experimental Raman spectrum was obtained with five excitation laser lines of 325, 532, 633, 785 and 1064 nm.

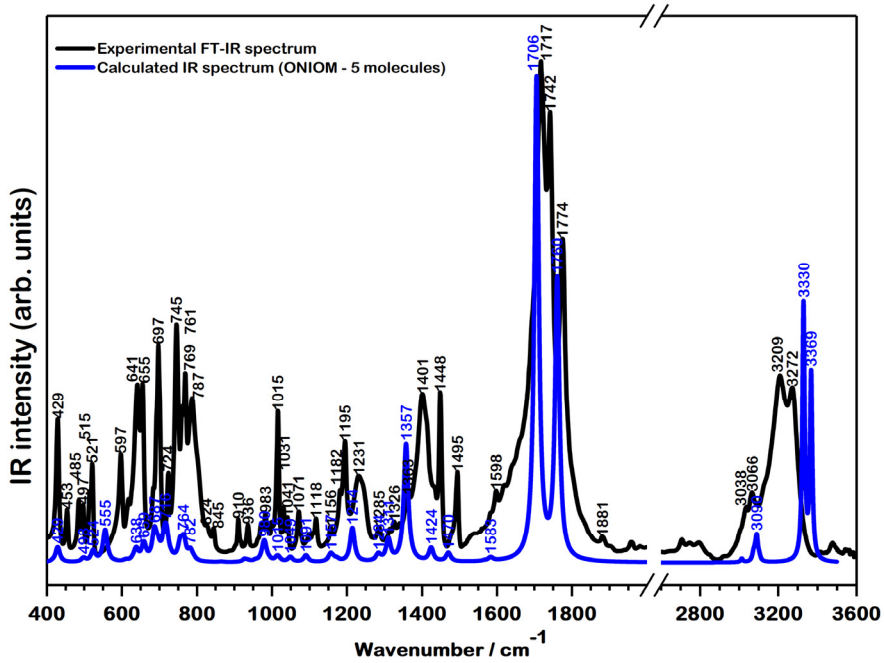

Fig. 3. Experimental FT-IR and calculated spectra (ONIOM(B3LYP/6-311+G(2d,p): B3LYP/3-21G)) of powdered DPH at room temperature

Fig. 5 illustrates the calculated Raman spectrum of DPH using the two models with different computational methodologies, along with the experimental Raman spectrum recorded by using the 633 nm laser line. The upper curve represents the calculated spectrum based on the QM:QM methodology where for the low layer comprising the 4 neighboring molecules (see Fig. 2) we used the B3LYP/3-21G

level of theory, while for the high level comprising only one molecule which was fully optimized we used the B3LYP/6-311+G(2d,p) level of theory. For the harmonic calculations the computed wavenumbers were scaled non-uniformly using scaling factors, derived for three spectral regions by fitting the wavenumbers corresponding to the most intense calculated Raman bands to their experimental counterparts. Thus, 0.955, 0.968 and 0.975 factors determined for $\tilde{\nu}$ > 2800 cm^{-1}, 1700 < $\tilde{\nu}$ < 2000 cm^{-1}, $\tilde{\nu}$ < 1700 cm^{-1}, respectively. It is worth mentioning that no scaling procedure was found in the literature for such QM:QM approaches.

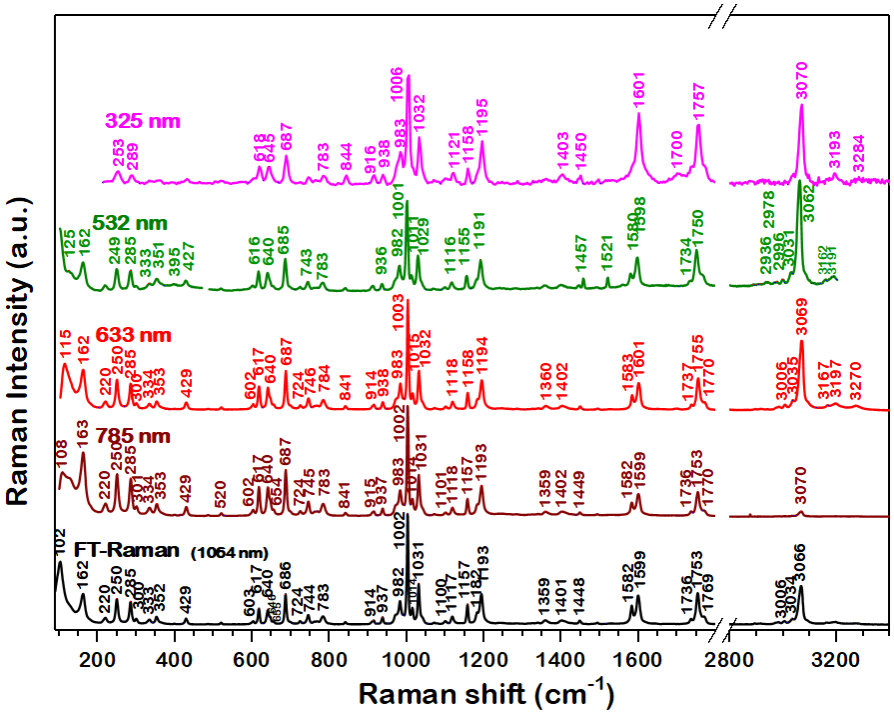

Fig. 4. Experimental Raman spectra of powdered DPH at room temperature recorded with five laser excitation lines

The second computational methodology uses the monomer model solvated in water and the calculations were performed based on the anharmonic approximation [21, 22], rooted into the second-order vibrational perturbation theory [23], at APFD/6-311+G(2d,p) level of theory. No frequency scaling was applied in this case.

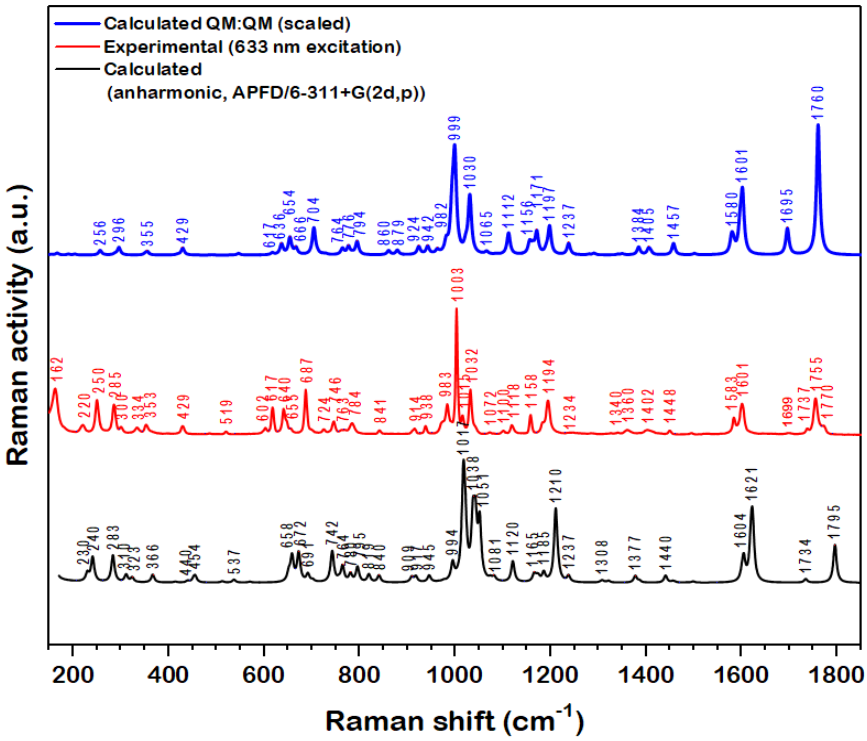

Fig. 5. Top: QM:QM calculated Raman spectrum of DPH; middle: Experimental Raman spectrum of powdered DPH at room temperature (633 nm laser line); bottom: Calculated anharmonic Raman spectrum of DPH in gas-phase at APDF/6-311+G(2d,p) level of theory.

As seen in Fig. 5, the experimental spectrum is much better reproduced by the cluster model treated within the ONIOM approach in the whole spectral range. We particularly note the excellent agreement for the Raman bands associated with the carbonyl stretches around 1755 cm^{-1}, the group of Raman bands between 983-1032 cm^{-1}, but also the spectral features observed in the 1072-1234 cm^{-1} and 602-784 cm^{-1} spectral ranges.

It is worth mentioning that, besides providing much better agreement with the experimental data, the quantum chemical calculations on cluster model take the advantage over the anharmonic calculations, being two orders of magnitude much faster. Thus, the total job CPU time in the case of ONIOM methodology was 24 hours and 23 minutes, compared to 3182 hours and 43 minutes for the anharmonic calculations.

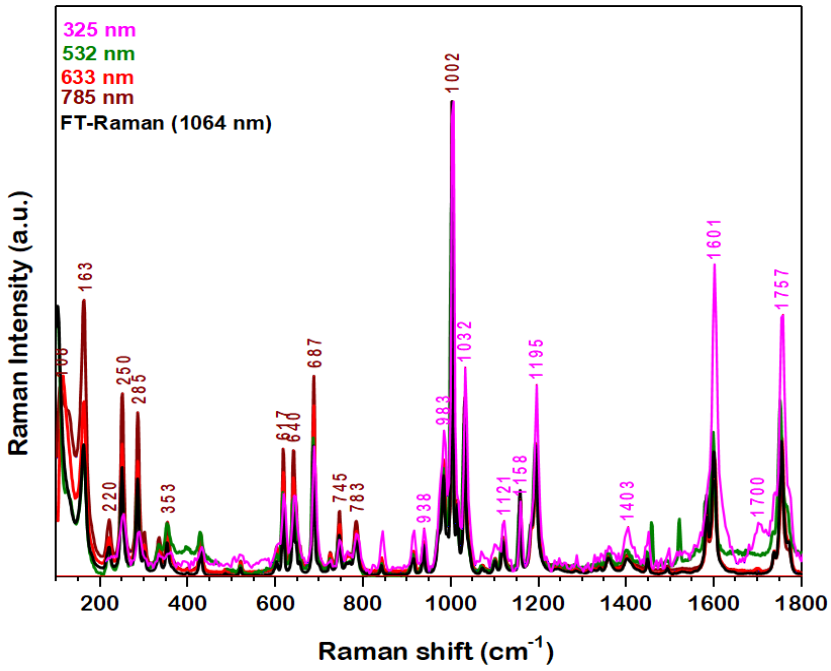

Fig. 6. Raman spectra of DPH recorded with 5 excitation laser lines, normalized to the most intense band at 1002 cm^{-1}.

The last column in Table 1 contains the motions that contribute the most to the different normal modes according to the ONIOM(QM:QM) theoretical data.

We shall first note that the IR bands observed for DPH at 1774 and 1717 cm^{-1} correspond to the most intense experimental IR bands at 1779 and 1717 cm^{-1} for hydantoin. Other IR bands of hydantoin (3265, 1296, 641, and 440 cm^{-1} [15]) observed in the spectrum of DPH are those located at 3272, 1285, 641 and 453 cm^{-1}.

The Raman bands characteristic for hydantoin (2977, 1735, 1698, 1071, 1000, 908, 642 and 414 cm^{-1} [15]) that can be seen in the spectrum of DPH are very close to their position in DPH but with significant lower intensity (2976, 1737, 1698, 1072, 1003, 914, 640 and 429 cm^{-1}). On the other hand, two strong Raman bands in the hydantoin's spectrum at 1422 and 580 cm^{-1} are not observed in the DPH's spectrum.

As seen in Fig. 3 and 4, at least three peaks can be identified in the IR and Raman spectrum of DPH in the spectral range characteristic for carbonyl group stretchings.

Due to its NH and C=O groups, DPH is available for hydrogen bonding, in solid state, as well as in liquid state. Consequently, the vibrations of the carbonyl groups are expected to be strongly affected by such interactions, both in their positions and intensities [24]. As shown in Table 1, we assigned the bands around 1750 cm^{-1} to free and hydrogen bonded carbonyl groups symmetric and asymmetric stretchings. The most intense IR bands for DPH are also the most intense in the IR spectrum of hydantoin.

DPH in solid sample shows the most intense peak in the IR spectrum at 1717, 1742, 1774 cm^{-1} and the set of fundamental bands at 3066, 3209, 3272 and 3479 cm^{-1}. Based on the DFT calculations the first set of peaks is assigned to the carbonyl vibrations coupled to the bending of the amide groups in the five-membered ring. The differences between the peaks are due to hydrogen intermolecular interaction and to symmetric or anti-symmetric nature of the stretchings.

From the second set, the peak at 3066 cm^{-1} is characteristic for aromatic C-H stretching and the others bands are assigned to the symmetric and anti-symmetric stretchings of the amide groups vibrations (ν_s(NH) and ν_{as}(NH)).

In the Raman spectrum of the solid DPH sample recorded with the 532 nm laser line one can observe the very intense bands at 1750 cm^{-1} and 3066 cm^{-1}. The computed data suggest that they are due to the symmetric stretching of the H-bonded C=O group, while the high wavenumber corresponds to the symmetric CH stretchings in the phenyl rings.

Other characteristic Raman bands of DPH are observed at 1601, and 1583 cm^{-1} (633 nm excited spectrum), both of them corresponding to the CC stretchings in the phenyl groups. The band at 1194 cm^{-1} is due to the stretching between the hydantoin and phenyl groups. No Raman band is observed for hydantoin in this region.

The band at 1003 cm^{-1} is the most intense in the Raman spectrum of DPH and it is due to a complex mode involving CCC bendings in phenyl groups as well as CNC bendings in the hydantoin group. The Raman spectrum of pure hydantoin shows a weak band at 1000 cm^{-1}.

It is worth mentioning the presence of a strong band at 1422 cm^{-1} in the Raman spectrum of hydantoin. According to our calculated data, it corresponds to $\beta(CH_2)$ vibrations and, as expectedly, it does not appear in the DPH's Raman spectrum because the CH_2 group does not exist in this molecule. Another hydantoin band that vanishes in the Raman spectrum of DPH is seen at 580 cm^{-1} and it is assigned to the out-of-plane deformation of hydantoin coupled to CH_2 rocking vibration. This deformation is hampered in DPH due to the connection to phenyl groups, thereby explaining the extinction of the corresponding band.

Table 1. Experimental and calculated wavenumbers (cm^{-1}) for DPH using the cluster model - QM:QM methodology and monomer model - anharmonic approximation) (see text for details).

Experimental wavenumber (cm^{-1})						Calculated wavenumbers (cm^{-1})		Assignments based on cluster model (QM:QM methodology)
FT-IR	FT-Raman 1064 nm	Raman 785 nm	Raman 633 nm	Raman 532 nm	Raman 325 nm	Monomer anharmonic	Cluster QM:QM	
	162	163	162	162		133	166	τ(Im)
	220	220	220	218		230	221	τ(Im)+τ(Ph)
	250	250	250	249	253	240	256	τ(Ph)
	285	285	285	285	289	283	296	ν(Ph-Im)
	333	334	334	333		323	350	$\delta(CCN)_{Ph\text{-}Im}$
	352	353	353	351		366	355	ρ(Ph)
429	429	429	429	427	435	454	429	$\beta(C{=}O)_{Im}$
521	519	520	519	518		537	545	γ(Ph)
618	617	617	617	616	618	651	617	$\delta(CCC)_{Ph}$
641	640	640	640	640	645	658	654	$[\delta(CCN)+\delta(CNC)+\delta(NCN)]_{Im}$
697	686	687	687	685	687	672	704	$\delta(CCC)_{Ph}$
745	744	745	746	743	749	742	764	γ(Ph)
787	783	783	784	783	783	795	794	$\delta(Im)+\gamma(CH)_{Ph}$
845	840	841	841	841	844	840	860	$[\gamma(CC)+\gamma(CH)]_{Ph}$
910	914	915	914	912	916	917	924	$\gamma(Im)+\nu(CC)_{Im\text{-}Ph}$
936	937	937	938	936	938	945	942	$\gamma(CH)_{Ph}$
983	982	983	983	982	983	994	982	$\gamma(CH)_{Ph}$
999	1002	1002	1003	1001	1006	1017	999	$\delta(CCC)_{Ph}+\delta(NCC)_{Im}+\delta(CNC)_{Im}$
1015	1014	1014	1015	1011		1020	1022	$\delta(NCC)_{Im}$
1031	1031	1031	1032	1029	1032	1038	1030	$\delta(CCC)_{Ph}$
1071	1072	1072	1071	1070	1070	1081	1065	$\nu(CN)_{Im}$
1118	1117	1118	1118	1116	1121	1120	1112	$\delta(CCC)_{Ph}+\nu(CN)_{Im}$
1156	1157	1157	1158	1155	1158	1165	1156	$\beta(CH)_{Ph}$
1195	1193	1193	1194	1191	1195	1210	1197	$\nu(CC)_{Ph\text{-}Im}+\beta(CH)_{Ph}$
1231	-	-	-	-	-	1237	1237	$\nu(CN)+\nu(CC)_{Im}$
1362	1359	1359	1360	1359	1361	1377	1384	$[\nu(CN)+\beta(NH)]_{Im}$
1401	1401	1402	1402	1400	1403	1385	1405	$[\nu(CN)+\beta(NH)]_{Im}$
1448	1448	1449	1450	1457	1450	1440	1457	$\nu(CN)_{Im}+\beta(NH)_{Im}+\beta(CH)_{Ph}$
1495	1493	1493	1495	1493	-	1498	1502	$\nu(CC)_{Ph\text{-}Im}+\beta(CH)_{Ph}$
-	1582	1582	1583	1580	1583	1604	1580	$\nu(CC)_{Ph}$
1598	1599	1599	1601	1598	1601	1621	1601	$\nu(CC)_{Ph}$
1717	-	-	1699	-	1700	1734	1695	$\nu_{as}(C{=}O)_{Im}$ *H bonded*
-	1736	1736	1737	1734	1733	-	-	$\nu_{as}(C{=}O)_{Im}$ *free*
1742	1753	1753	1755	1750	1757	1795	1760	$\nu_{s}(C{=}O)_{Im}$ *H bonded*
1774	1769	1770	1770	1769	1776	-	-	$\nu_{s}(C{=}O)_{Im}$ *free*
3038	3034	-	-	-	-	3062	3041	$\nu_{as}(CH)_{Ph}$
3066	3066	3070	3069	3062	3070	3082	3067	$\nu_{s}(CH)_{Ph}$
3209	3192	-	3197	3191	3199	3492	3051	$\nu_{as}(NH)_{Im}$
3272	3276	-	3270	-	3284	3510	3282	$\nu_{s}(NH)_{Im}$

Comparing the accuracy of the two used computational methodologies, it is evident that the anharmonic approximation provides better calculated frequencies for only 10 peaks, out of the total of 37 (see Table 1). Seven of the 10 cases correspond to low wavenumbers, between 240 – 917 cm^{-1}, and all of them are assigned to out-of-plane vibrations. The rest of three bands are found between 1020 – 1498 cm^{-1} and they correspond to δ(NCC), ν(CN)+β(NH) and ν(CC)+β(CH) normal modes. In addition, excepting the high wavenumbers, the largest discrepancies between the anharmonic and cluster computational methodologies was noted for the symmetric stretches of the C=O H-bonded groups.

The assignments given in Table 1 contains also the group involved in each vibration and for this reason we will not discuss in more details the two vibrational spectra of DPH. We emphasize here that reliable assignments of the vibrational bands of complex molecular structures like active pharmaceutical ingredients can only be obtained by analyzing also the spectra of the constituting groups, if available.

We would like to mention also that even though the Raman spectra recorded by using different excitation lasers are very similar in terms of peaks' positions and the relative intensities of nearby peaks, a significant change is observed in the bands' intensities when going from the 325 nm to 785 nm excitation laser lines. As illustrated in Fig. 6, where all the spectra have been normalized to the most intense band (1002 cm^{-1}), the 785 nm laser gives rise to more intense Raman bands within the 100 – 800 cm^{-1} spectral region, while in the 800 – 1800 cm^{-1} the most intense Raman bands are obtained with the 325 nm excitation laser. A significant increase is observed particularly for the Raman bands at 1601, 1757 and 1195 cm^{-1}.

None of the used laser is in resonance with the electronic transitions of DPH, thus, this behavior cannot be explained based on the resonance conditions. Similar changes were observed previously by Thorley et al. [25] who analyzed the dependence of the Raman spectra of a set of 4 pharmaceutical ingredients on the excitation wavelength. As in our case, the mentioned work shows that the UV laser gives rise to more intense Raman bands at higher wavenumbers. Nergui et al. [26] have proposed for adenine that such wavelength dependence of the Raman peak intensities could be explained by considering the pre-resonant conditions, even though the wavelength of the excitation lasers are far from resonance. Most probably, the same assumption is valid for the characteristic increase of Raman activities for the higher wavenumber Raman bands of DPH. Another explanation could be the polarizability dependence of DPH on the excitation laser wavelength. Further investigations are needed in order to clarify this behavior.

5. CONCLUSIONS

The experimental vibrational spectra of diphenylhydantoin were obtained by Using FT-IR and Raman technique with five excitation laser lines of 325, 532, 633, 785 and 1064 nm. The normal modes assignment was performed on the basis of the spectrum calculated spectrum for a cluster of five DPH molecules whose initial structure was taken from available X-ray data. For this purpose we used the QM:QM methodology (two layers, B3LYP/3-21G level of theory for the low layer composed of 4 molecules and B3LYP/6-311+G(2d,p) for the high layer composed of one molecule. This methodology was found to be much more convenient compared to the anharmonic calculations, due to the greater accuracy of the calculated bans, as well as to the much shorter time required for running the necessary jobs.

The Raman bands in the spectrum recorded with the 325 nm laser are more enhanced with respect to the other lasers for Raman shifts greater than 800 cm^{-1}. On the other hand, for smaller wavenumbers, the 785 laser gives the most intense Raman bands. Pre-resonant conditions and the polarizability dependence of the molecule on the used laser could explain such behavior.

For reliable assignments of the vibrational bands of complex molecules like drugs, we recommend the vibrational analysis of the constituting groups. Moreover, the choice of a correct model and a proper methodology is mandatory for accurate computational results.

REFERENCES

[1] A. Camerman, N. Camerman, *Acta Cryst.* B27 (1971) 2205.
[2] S. Chakrabarti, R. van Severen and P. Braeckman, *Pharmazie* 33 (1978) 338-339.
[3] M. F. Wu, W. H. Lim, Phenytoin: A Guide to Therapeutic Drug Monitoring, Proceedings of Singapore Healthcare, 22 (2013) 198 – 202.
[4] R. Luchian, PhD thesis, Babeș-Bolyai University, 2018
[5] R. Luchian, E. Vinţeler, C. Chiş, M. Vasilescu, N. Leopold, V. Chiş, *Croatica Chemica Acta,* 88 (2015) 511-522
[6] Gaussian 16, Revision C.01, M. J. Frisch, G. W. Trucks, H. B. Schlegel, G. E. Scuseria, M. A. Robb, J. R. Cheeseman, G. Scalmani, V. Barone, G. A. Petersson, H. Nakatsuji, X. Li, M. Caricato, A. V. Marenich, J. Bloino, B. G. Janesko, R. Gomperts, B. Mennucci, H. P. Hratchian, J. V. Ortiz, A. F. Izmaylov, J. L. Sonnenberg, D. Williams-Young, F. Ding, F. Lipparini, F. Egidi, J. Goings, B. Peng, A. Petrone, T. Henderson, D. Ranasinghe, V. G. Zakrzewski, J. Gao, N. Rega, G. Zheng, W. Liang, M. Hada, M. Ehara, K. Toyota, R. Fukuda, J. Hasegawa, M. Ishida, T. Nakajima, Y. Honda, O. Kitao, H. Nakai, T. Vreven, K. Throssell, J. A. Montgomery, Jr., J. E. Peralta, F. Ogliaro, M. J. Bearpark, J. J. Heyd,

E. N. Brothers, K. N. Kudin, V. N. Staroverov, T. A. Keith, R. Kobayashi, J. Normand, K. Raghavachari, A. P. Rendell, J. C. Burant, S. S. Iyengar, J. Tomasi, M. Cossi, J. M. Millam, M. Klene, C. Adamo, R. Cammi, J. W. Ochterski, R. L. Martin, K. Morokuma, O. Farkas, J. B. Foresman, and D. J. Fox, Gaussian, Inc., Wallingford CT, 2016.

[7] A.D. Becke, *J. Chem. Phys.,* 98 (1993) 5648-5652.

[8] C. Lee, W. Yang, R.G. Parr, *Phys. Rev. B*, 37 (1988) 785.

[9] S.H. Vosko, L. Wilk, M. Nusair, *Can. J. Phys.*, 58 (1980) 1200-1211.

[10] P.J. Stephens, F.J. Devlin, C.F. Chabalowski, M.J. Frisch, *J. Phys. Chem.,* 98 (1994) 11623-11627.

[11] A. Austin, G. Petersson, M. J. Frisch, F. J. Dobek, G. Scalmani, and K. Throssell, *J. Chem. Theory and Comput.,* 8 (2012) 4989-5007.

[12] W.J. Hehre, R. Ditchfield, J.A. Pople, *J. Chem. Phys.*, 56 (1972) 2257-2261.

[13] T. Kimura and Y. Nagao, *Bull. Fac. Sci. Tech. Hirosaki Univ*. 5, 11 (2003).

[14] G.O. Ildiz, I.Boz, O. Unsalan, *J. Optics and Spectroscopy,* 112 (2012) 665-670.

[15] Bio-Rad Laboratories, Inc. SpectraBase; SpectraBase Compound ID=UhBVhrEdKp http://spectrabase.com/compound/UhBVhrEdKp (accessed Jul 21, 2017).

[16] V. Barone, I. Carnimeo, G. Scalmani, *J. Chem. Theory Comput.*, 9 (2013) 2052-2071.

[17] G.M. Hannaa, Drug. Dev. Ind. Pharm. 10 (1984) 341-354.

[18] A Łapiński, J. Spanget-Larsen, M. Langgård, J. Waluk, J. G. Radziszewski, *J. Phys. Chem. A,* 105 (2001) 10520–10524.

[19] T. López, P. Quintana, E. Ortiz-Islas, E. Vinogradova, J. Manjarrez, D.H. Aguilar, P. Castillo-Ocampo, C. Magaña, J.A. Azamar, *Mater. Charact.* 58 (2007) 823–828.

[20] S. Gunasekaran, R. T. Thilak, S. Ponnusamy, *Spectrochim. Acta A*, 65 (2006) 1041-1052.

[21] V. Barone, M. Biczysko, J. Bloino, *Phys. Chem. Chem. Phys.* 16 (2014) 1759-1787.

[22] Y. Cornaton, M. Ringholm, O. Louant, K. Ruud, *Phys. Chem. Chem. Phys.,* 18 (2016) 4201-4215.

[23] M. Piccardo, J. Bloino, V. Barone, *Int. J. Quantum Chem.*, 115 (2015) 948−982.

[24] T. Fornaro, D. Burini, M. Biczysko, V. Barone, *J. Phys. Chem. A*, 119 (2015) 4224–4236.

[25] F.C. Thorley, K.J. Baldwin, D.C. Lee, D.N. Batchelder, J. Raman., *Spectrosc.*, 37 (2006) 335-341.

[26] N. Nergui, M.–J. Chen, J.-K. Wang, Y.-L. Wang, C.-R. Hsing, C.-M. Wei, Kaito Takahashi, *J. Phys. Chem. A*, 120 (2016) 8114−8122.